EFFICIENT DETECTION OF CLOUD SCENES BY A SPACE-ORBITING ARGUS 1000 MICRO-SPECTROMETER

REHAN SIDDIQUI

A DISSERTATION SUBMITTED TO
THE FACULTY OF GRADUATE STUDIES
IN PARTIAL FULFILLMENT OF THE REQUIREMENTS
FOR THE DEGREE OF

DOCTOR OF PHILOSOPHY

GRADUATE PROGRAM IN PHYSICS & ASTRONOMY
YORK UNIVERSITY
TORONTO, ONTARIO

August 2017

Abstract

The description, interpretation and imagery of clouds using remote sensing datasets collected by Earth-orbiting satellites have become a great debate spanning several decades. Presently, many models for cloud detection and classification have been reported in the modern literature. However, none of the existing models can efficiently detect clouds within the shortwave upwelling radiative wavelength flux (SWupRF) band. Therefore, in order to detect clouds more efficiently, a method known as radiance enhancement (RE) can be implemented. A satellite remote sensing database is one of the most essential parts of research for monitoring different atmospheric changes. This study proposes an innovative approach using RE and SWupRF to distinguish cloud and non-cloud scenes by using a space-orbiting Argus 1000 spectrometer utilizing the GENSPECT line-by-line radiative transfer simulation tool for space data retrieval and analysis. We apply this approach within the selected wavelength band of the Argus 1000 spectrometer in the range from 1100 nm to 1700 nm to calculate the integrated SWupRF synthetic spectral datasets. We used the collected Argus observations starting from 2009 to investigate radiative flux and its correlation with cloud and non-cloud scenes. Our results show that the RE and SWupRF model can identify most of the cloudy scenes except for some thin clouds that cannot be identified reasonably with high confidence due to complexity of the atmospheric system. Based on our analysis, we suggest that the relative correlation between SWupRF and RE within a small wavelength band can be a promising technique for the efficient detection of cloudy and non-cloudy scenes.

Acknowledgements

Foremost, I would like to express my sincere gratitude to my supervisor Prof. Brendan M. Quine, for all his continuous guidance, encouragement and assistance over the past several years throughout my doctoral studies, with his patience, motivation, enthusiasm and immense knowledge. His guidance helped me in all the areas of research and development and writing of this dissertation. His exceptional leadership and project management skills have benefited me immensely.

I would also like to extend my thanks to members of my supervising committee, Prof. George Z. H. Zhu and Prof. James A. Whiteway, for their instructions, guidance, advice, and encouragement throughout my journey. I am grateful for the opportunity to have had such a proficient supervising team.

I am grateful to my many PhD fellow mates and Teaching Assistant colleagues, specially Dr. Alain Amarsman, for providing a stimulating and friendly environment in which to learn and grow at York. I am grateful to Marlene Caplan, an Administrative Assistant to the Director of Physics and Astronomy at York University, for assisting me in many ways.

My sincere thanks also go to Dr. Raj Jagpal and Dr. Sanjar Abrarov for guiding me towards successful completion of my project. I am also thankful to my Argus science team members, Naif M. AlSalem, Catherine Tsouvaltsidis and Guy Benari, for their sincere support and continual helpful suggestions during my research work. I thank Dr. Alan Yoshioka for editorial assistance.

I would like to extend my special thanks to my parents and my wife for their wishes and moral support, my kids for their love, all my brothers and sisters for their

encouragement and very deepest thanks to my wife, Uzma Rehan, for providing a me an unwaveringly loving environment throughout my study and research time at York University, Toronto and aiding the timely completion of my project. I dedicate this thesis to my parents and my wife. I am also thankful to Canadian Advanced Nano Space Experiment 2 Operations Team and Thoth Technologies, Inc. for their technical support.

Finally, I would like to acknowledge the Natural Science and Engineering Research Council (NSERC) of Canada, York University Graduate Fellowship Doctoral, Queen Elizabeth II Scholarship (QEII), Ontario, Ralph Nicolls Award, Vernon Oliver Stong Graduate Scholarship in Science and Fiera Sceptre Inc. Scholarship in Science and the granting agencies for their financial support.

Table of Contents

List of Tables

List of Figures

List of Abbreviations

ACE	Atmospheric Chemistry Experiments
ACS	American Chemical Society
ATMOS	Atmospheric Trace Molecular Spectroscopy
AGL	Above Ground level
ATS	Applications Technology Satellite
AVHRR	Advanced Very High-Resolution Radiometer
BB	Blackbody
CALIPSO	Cloud-Aerosol Lidar and Infrared Pathfinder Satellite Observation
CanX-2	Canadian Advanced Nano space eXperiment 2
CERES	Clouds and the Earth Radiation Energy System
CERES	Clouds and the Earth's Radiant Energy System
CRE	Combined Radiance Enhancement
CRF	Cloud Radiative Forcing
ECEF	Earth Centered Earth Fixed Frame
ECI	Earth Centered Inertial
EMR	Electromagnetic Radiation
EMRS	Electromagnetic Radiation Spectrum
ENVISAT	European Environmental Satellite
EOS	Earth Observation from Space
EOs	Earth Observations
ERBE	Earth Radiation Budget Experiment
EM	Electromagnetic
ERBS	Earth Radiation Budget Satellite
ESA	European Space Agency
EWR	Energy Waves Region
FAR4	Fourth Assessment Report 4
FOV	Field of View
FTS	Fourier Transform Spectrometer
GOES	Geostationary Operational Environmental Satellite
GOSAT	Greenhouse gases Observing SATellite
GOMOS	Global Ozone Monitoring by Occultation of Stars
HITRAN	High Resolution Transmission
HRG	High Resolution Geometrical
INPs	Ice-Nucleating Particles
IPCC	Intergovernmental Panel on Climate Change
IR	Infrared
IRR	Infrared Region

ISCCP	International Satellite Cloud Climatology Project
JPC	Joules-per-count
LEO	Low Earth Orbit
LW	Longwave
LBL	Line By Line
MetOpS	Meteorological Operational Spacecraft
MODIS	Moderate Resolution Imaging Spectroradiometer
MOPITT	Measurement of Pollution in the Troposphere
NIR	Near Infrared
NIRR	Near Infrared Region
NOAA	National Oceanic and Atmospheric Administration
NOAA	National Oceanic and Atmospheric Administration
NORAD	North American Aerospace Command
OBS	Observed
OCO	Orbiting Carbon Observatory
OMI	Ozone Monitoring Instrument
POLDER	Polarization and Directionality of the Earth's Repentances
PSLV	Indian Polar Satellite Launch Vehicle
RE	Radiance Enhancement
SCB	Space Craft Body
SCIAMACHY	Scanning Imaging Absorption Spectrometer for Atmospheric Chartography
SDSC	Satish Dhawan Space Centre
SNR	Signal to Noise Ratios
SB	SathyamabaSat
SPG4	Simplified General Perturbation 4
SRCA	Spectral Radiometric Calibration Assembly
SDSC	Satish Dhawan Space Centre
SDSM	Solar Diffuser Stability Monitor
STK	Systems Tool Kits
SW	Shortwave
SWIR	Short Wave Infrared
SWIRR	Shortwave Infrared Region
SWupRF	Short Wave upwelling Radiative Flux
SYN	Synthetic
SZA	Solar Zenith Angle
TIROS	Television Infrared Observation Satellite
TOA	Top of Atmosphere
TIRR	Thermal Infrared Region
TLE	Two-Line Element

UTIAS/SFL	University of Toronto Institute for Aerospace Studies/ Space Flight Laboratory
UV	Ultraviolet
VIS	Visible
VISR	Visible Region
VNIR	Very Near Infrared
WCRP	World Climate Research Program

1.0 INTRODUCTION

The World Climate Research Program (WCRP) was established in 1982 as part of the International Satellite Cloud Climatology Project (ISCCP), to compile a comprehensive global satellite dataset in order to advance the field of cloud climatology [Schiffer R. A., et al., 1983]. Clouds participate in the key energy exchange processes that drive the Earth's climate, namely solar, atmospheric, and terrestrial (ground and water) radiance transfer [Rossow W.B., et al., 1993], and thus cloud detection from remote sensing datasets has long been an important area of interest. A long-term research program has been carried out to develop algorithms for distinguishing surface and cloud types in the polar regions [Ebert, E.E., 1987, 1989, 1992, 2007]. Another cloud detection algorithm, focusing on the CO_2 absorption band within thermal infrared data, was developed using high-resolution radiance spectra from the Greenhouse gases Observing SATellite (GOSAT) [Someya, Y., et al., 2016].

For satellite-based cloud detection, it is necessary to have a good estimate of Earth's surface albedo [Hendrick, F., et al., 2005], in order to compare the measured reflectance with the expected reflectance from cloud scenes [Li, W. et al., 2008]. Satellite instruments operating in the near infrared SW band are efficient tools for the detection of cloud scenes [Siddiqui, R., et al., 2015], and there is an increasing use of satellite data to calculate surface SW radiative fluxes [Jiang, J. H., et al., 2012; Henderson, D. S., et al., 2013; McCoy, D. T., et al., 2014; Siddiqui, R., et al., 2017].

This thesis presents a new method for the efficient detection of clouds, based on atmospheric near-infrared (NIR) radiance measurements made by the Argus 1000 spectrometer at various locations on the globe. The Argus instrument performs space-based

measurements of outgoing thermal radiation to monitor absorption by atmospheric constituent gases [Jagpal, R.K., et al., 2010, 2011]. Argus has a spectral resolution of approximately 6 nm, and within its narrow spectral range of 900 nm to 1700 nm, gases such as carbon dioxide (CO_2), methane (CH_4), oxygen (O_2) and water vapor (H_2O) exhibit significant infrared emission features. The orbiting Argus spectrometer measures near infrared (NIR-SW) shortwave radiation [Jagpal, R.K., et al., 2010, 2011; Chesser, H. et al., 2012; Siddiqui, R., et al., 2015], and these spectra form the basis of this work's radiance-enhancement (RE) and shortwave upwelling radiative flux (SWupRF) methodology for the efficient detection and classification of cloud scenes [Siddiqui, R., et al., 2015].

Analysis of the Argus spectral data, in conjunction with the output of the GENSPECT line-by-line (LBL) radiative transfer model [Quine, B. M., et al., 2002; Jagpal, R.K., et al., 2010; Chesser, H. et al., 2012; Quine & Abrarov 2013; Siddiqui, R., et al., 2015] can accurately predict the RE and SWupRF over a wide area of the Earth, leading to an improved detection probability of cloud scenes. The GENSPECT model accounts for different input parameters such as surface albedo, Solar Zenith Angle (SZA), water vapor concentration, and atmospheric mixing ratios of O_2, CO_2, CH_4, etc. concentrations, to calculate simulated IR spectra, which can be compared to measured data, and thus characterize the SW radiative flux

1.1 Clouds and Shortwave Radiation

Clouds are generally characterized by a higher reflectance and lower temperature than either the surrounding atmospheric layers or Earth's surface [Ackerman, S.A. et al., 1998]. Accurate monitoring of the Earth's radiation budget is essential for understanding

Earth's climate system and its dynamics [Hatzianastassiou, N., et al., 2005], and clouds play a significant role through absorption and scattering of incident radiance within different atmospheric layers. These processes are distinct from the interactions of radiation with gaseous species such as water vapor, carbon dioxide, and oxygen, or the scattering of light by dust and aerosol particles [Hausmann, P., et al., 2012; Siddiqui R., et al., 2016].

The net surface SW radiation is the difference between the amount of incoming and outgoing shortwave radiation, and represents the amount of solar radiation absorbed by Earth's surface [Inamdar, A.K. et al., 2015]. It is known that clouds are the main contributors in modulating the Earth's energy budget and climate [Mitchell, D. L. et al., 2009], and they are involved directly in temperature convection processes close to Earth's surface [Siddiqui, R., et al., 2015]. Clouds typically take on the ambient environment atmospheric temperature, that under normal lapse rate conditions decreases with increasing altitude. Therefore, by measuring a cloud's radiative emission and converting it to the equivalent black body temperature, opaque clouds can be distinguished from the warmer Earth surface by using a threshold technique that is described, for example, in the work of [Fournier, N., et al., 2006]. Consequently, the incoming solar radiation is attenuated as it penetrates downward to the atmosphere, reflects from the surface, and travels back to space. Solar radiation passing through the atmosphere may be scattered by its constituents; this may take any of the two forms: Rayleigh and Mie scattering. When the size of the atmospheric particles is close to, or greater than, the wavelength of the incident radiation Mie scattering becomes significant. This is the case with aerosols, cloud droplets and ice crystals. Rayleigh scattering describes the interaction of incident light with particles whose sizes are small compared to the wavelength of the radiation.

Absorption and emission processes also occur, whereby incident radiant energy is converted into thermal kinetic energy and completely removed from the incoming flux, or in the case of emission, thermal motion of molecules drives collisions that excite molecular species, which subsequently release their energy as radiation.

In the atmosphere, the attenuation includes molecular Rayleigh scattering, Mie scattering, and absorption by CO_2, CH_4, CO and water vapor in the form of clouds [Mishchenko, M.I., et al., 2002; Siddiqui R. et al., 2014; Siddiqui R. et al., 2016].

Although both types of scattering are small over the Argus spectral range, these effects, are included in the analysis. The most abundant greenhouse gas, H_2O, represents the main interest in analysis of clouds [Siddiqui R., et al., 2015]. We know that carbon dioxide gas absorbs energy in some small segments of the thermal infrared spectrum where water vapor does not strongly absorb [Fu, Q., et al., 2002]. This extra absorption within the atmosphere causes the air to warm more and a warmer atmosphere has a greater capacity to hold water vapor within clouds [Fu, Q., et al., 2002]. The attenuation also includes extinction (scattering plus absorption) by aerosols and clouds [Mao, J. et al., 2004].

Surface radiative flux is a major component affecting temperature, due to the energy exchange between the atmosphere and the land or ocean surface [Field, C. B., et al., 2014]. The net surface radiation modifies the energy and water exchange between the biosphere and the atmosphere, and has a major impact on Earth's weather and climate [Stephens, G. L., et al., 2012]. Earth climate is determined by the flows of energy in and out of the Earth [Stephens, G. L., et al., 2012; Andrews, T., et al., 2009], and changes to the surface energy balance also ultimately control how this hydraulic cycle corresponds to the small energy imbalances that force climate change [Andrews, T. et al., 2009].

Solar shortwave radiation is the dominant energy source of the Earth. It plays a key role in hydrology, metrology, agriculture and climate change [Wang, T., et al., 2014]. The Earth surface net SW radiation is the difference between the incoming and outgoing SW radiation, represents the amount of solar radiation absorbed by surface [Inamdar, A. K., et al., 2015]. Net surface radiation is the driving force for the surface energy balance and the transport between the surface and the atmosphere. In addition, the net SW radiation significantly affects the climate dynamics [Tang, B., et al., 2006]. Accurate characterization of SW radiation levels on the surface is also a significant factor that has to be accounted for in the detection of clouds [Mitchell, D. L., et al., 2009; Mateos, D., et al., 2014; Furlan, C., et al., 2012; Islam, M. D., et al., 2009]. Therefore, the understanding impact of the SW to the clouds detection is a main part of the present research.

1.2 Radiance Measurements

Cloud detection is a preliminary key step in most known techniques for processing radiance data from satellites [Cutillo, L., et al., 2004]. In general, different cloud models are introduced in radiance transfer. Their influence on the radiance emitted from Earth's surface is estimated with respect to clear sky conditions at spectral regions as described by Cutillo and coauthors [Cutillo, L. et al., 2004]. An efficient way to accurately model atmospheric variation with height is to divide the atmosphere into a large number of relatively thin homogeneous layers or cells, where the required parametric values of each layer correspond to those of in the real atmosphere [Quine, B.M. et al., 2002]. The satellite instrument measures the radiance emitted by clouds, atmospheric gases, and Earth's surface into the instruments line of sight view captured by small sensors similar to the Argus spectrometer. Incoming solar radiance reflected by the top cloud layer is a function

of cloud thickness, particle density, size, and shape [Mishchenko, M.I., et al., 1996; Fu, Q., et al., 1998; Yang, P., et al., 2005].

1.3 Research Objectives

The main objectives of the present work are:

- To develop a new technique for the efficient detection of clouds and the types of clouds within the NIR wavelength band of Argus 1000 micro-spectrometer by using satellite remote sensing datasets of trace gases.
- To develop an efficient algorithm for computing the radiance-enhancement (RE) characteristics of the NIR spectra obtained from the Argus instrument, incorporating the GENSPECT line-by-line radiative transfer model for RE-cloud model.
- To develop an efficient algorithm for calculating the measured shortwave upwelling radiative flux (SWupRF) within the Argus spectral wavelength range for the detection and classification of cloud scenes.
- To validate the RE and SWupRF results within an optimal wavelength range, and with adequate spectral and spatial resolution for the detection of cloud scenes, by comparing these results with those from other models.
- To provide algorithms and methods producing cloud spectral datasets for the Global Cloud Models. These datasets can be used to simulate various types of cloud scenes and climate change scenarios by using RE and SWupRF. Our algorithms and methods can be implemented to assist in detecting and monitoring cloud scenes for application in climate change policy.

1.4. Research Motivation

The Fourth Assessment Report (FAR4) of the Intergovernmental Panel on Climate Change (IPCC 2014, Topic 2, p. 56) affirms: "Clouds and aerosols continue to contribute the largest uncertainty to estimates and interpretations of the Earth's changing energy budget". Reliable identification of global cloud cover is therefore important for the accurate modeling of Earth's radiative energy balance. This requires improvement in detection of cloud scenes (cloud types, coverage, dynamics, etc.) as well as measurement of radiance in both the short and long wavelength spectral regions.

Clouds play an important role in shaping Earth's climate, and have an impact on the terrestrial environment, due to their effect on surface cooling or heating rates. [Siddiqui R. et al., 2015]. Uncertainties in the systematic effects of clouds on atmospheric radiative transfer mechanisms, and their feedback to the ecosystem, need to be resolved in order to better understand Earth's climate system [Jedlovec, G. 2009]. This requires characterization of cloud types, geographic distribution, altitude, and radiative transfer properties within different wavelength bands. Accurate identification of clouds is an issue for a wide-range of remote sensing applications, particularly for instruments operating in the visible and NIR bands, due to significant effects caused by different types of cloud constituents [Gómez-Chova, L., 2007; Siddiqui R., et al., 2015].

Clouds and other airborne particles can scatter photons into the instrument field of view (FOV), scatter photons away from the instrument FOV, or reflect solar radiation back to space before it transverse downwards preventing full atmospheric column of the trace gas measurements in the region occupied by clouds [Jagpal R.K. et al., 2010; Siddiqui R. et al., 2015]. Figure 1.1 illustrates this process schematically.

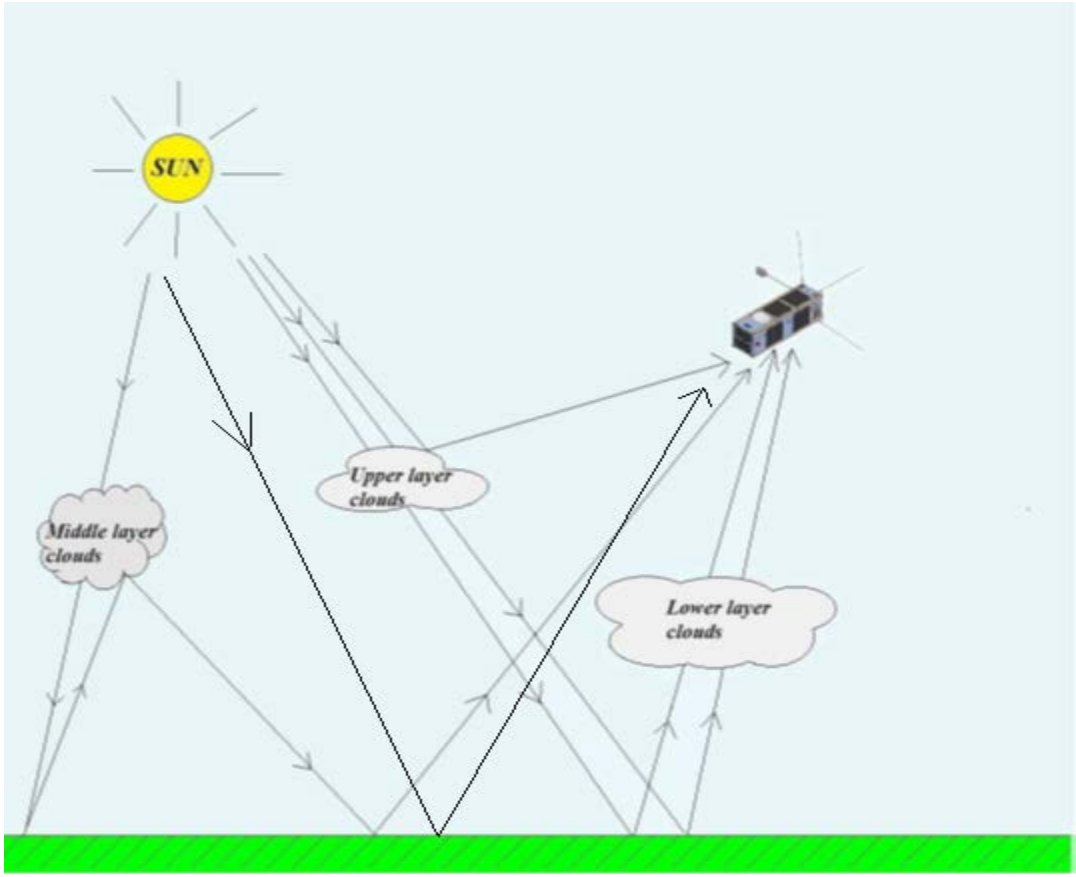

Fig. 1.1. Shortwave radiation path lengths through various cloud layers [Siddiqui R. et al., 2015, modified version]

To the best of our knowledge, this research is the first use of Radiance Enhancement [Siddiqui R., et al., 2015] and Shortwave upwelling Radiative Flux [Siddiqui R. et al., 2017] for efficient detection of clouds by a space-based spectrometer. The work covers spectral measurements over the Arabian Sea, Canada, and the North Pacific Ocean taken over a long period of time, starting in 2009. The impact of altitude, solar zenith angle (SZA), sun angle, atmospheric gas mixing-ratio concentrations (especially H_2O and CO_2), and different albedos on enhancement of radiance and radiative flux are investigated by using the GENSPECT radiative transfer model [Quine M.B. et al., 2002; Siddiqui R., et al., 2015; Siddiqui R., et al., 2016; Siddiqui R., et al., 2017]. The purpose of this work is

to develop a new cloud detection model and to demonstrate that the relatively narrow NIR-SWIR wavelength range is efficient for detecting different types of cloud scenes. The dependence of accurate cloud detection retrievals from the Argus data on variations in atmospheric mixing ratios, geolocation of the instrument, altitudes, and surface albedo is investigated [Siddiqui R., et al., 2015]. We have shown statistically that the proposed method based on the RE and SWupRF provides a significant improvement in detection of cloud scenes. Consequently, the results we developed can be used for solar energy applications, climate modeling, and atmospheric chemistry.

1.5 Thesis Organization

Chapter 2 reviews the theoretical background describing clouds, cloud formations processes and atmospheric cloud layer. A literature survey summarizes existing research. This chapter also presents the methodology for modeling radiative transfer processes in the atmosphere.

Chapter 3 details the Argus 1000 micro-spectrometer, describing the instrument's design, viewing geometry, resolution, data structure and operation, with a brief description of the GENSPECT line-by-line radiative transfer model. It also provides an overview of the remote sensing of different trace gases and clouds from space in the near infrared band.

Chapter 4 proposes a new method for the evaluation of radiance enhancement (RE), due to the presence of clouds, in Argus spectral measurements. This algorithm uses the spectral radiance in four selected bands between 1100 to 1700 nm, comparing Argus observations with model spectra in order to optimize cloud detection. The information content of these RE results is discussed.

Chapter 5 applies the integrated absorption technique to determine the total shortwave upwelling radiative flux (SWupRF) in the Argus datasets. Comparison with Moderate Resolution Imaging Spectro-radiometer (MODIS)-Aqua/Terra satellite images are made to validate the RE and SWupRF results.

Chapter 6 summarizes the main results, provides concluding remarks and makes recommendations for future work.

2.0 CLOUDS AND ATMOSPHERE

2.1 Introduction

Clouds are a special type of atmospheric layer that appears when the air becomes supersaturated with water vapor. Cloud particles grow rapidly until the cloud is visible as a singular, compact entity, in contrast to dispersed atmospheric aerosols [Stevens, B., 2011]. Clouds can also be characterized as a mass of condensed water vapor or ice particles suspended above the Earth surface.

In order to reduce the uncertainties in our understanding of Earth's global energy balance, it is useful to determine with greater accuracy the distribution of clouds at specific geographical locations. In this chapter, a brief overview is presented of the theory of cloud formation, cloud types, and their characteristics. Then a short introduction is given to remote sensing systems and how they operate. The survey of satellite remote sensing instruments within NIR wavelength bands is also discuss in the same section. Then, there is a general discussion of electromagnetic radiation and radiative transfer processes. Finally, there is a brief introduction of GENSPECT line by line (LBL) radiative transfer model and shortwave and longwave radiative flux.

2.2 Theoretical Background

Clouds are important in the regulation of the Earth climate, terrestrial atmospheric dynamics, thermodynamic chemistry and radiative transfer [Cooper, S.J. et al., 2003]. They play a key role in the water cycle and are effective in removing pollution from the atmosphere through precipitation [Wang, X.C., et al., 2015]. Therefore, it is of the great interest to understand cloud characteristics, physical presence, and distribution on a global

scale. This can be achieved effectively using satellite observations [Kokhanovsky, A.A., et al., 2011]. Efficient detection of clouds in remote sensing data is a key goal in a wide range of remote sensing applications, especially in the case of sensors working in the near infrared (NIR) range of the electromagnetic spectrum, due to the absorption and scattering characteristics of cloud layers [Feister U., et.al., 1998; Simpson J.J., 1999; Elhag, M. et.al., 2014; Siddiqui R. et.al., 2015]. Cloud particles absorb, emit, and scatter radiation over a broad range of wavelengths in the infrared (IR) [Greenhough, J., et al., 2005], and thus the effect of cloud layers may be a significant factor in the analysis of infrared data sets below 30 km. [Waters, J.W. et al., 1999]. Due to emission of radiation, clouds can also prevent cooling of the ground on a cloudy night [Stevens, B. et al., 2011].

The radiative properties of clouds include the propensity to scatter visible radiation and the ability to absorb and emit infrared radiation. Scattering of visible radiation depends both on the amount of suspended water mass and the size of suspended particles, while the efficiency of clouds in absorbing and emitting infrared radiation depends primarily on the suspended water mass [Stevens, B. et al., 2011]. The presence of clouds strongly affects radiative transfer processes in the atmosphere, with a colossal impact to the climate system [Ramanathan, V., 1987; Bernstein, L. et al., 2007; IPCC, 2007a]. Clouds and other airborne particles absorb and scatter solar radiation back to space before it traverses down the full atmospheric column, preventing the full column of CO_2 measurements [Jagpal, R.K., et al 2010]. For a long time, due to the large variation of cloud types and their different radiative properties, the impact of the net radiative effects of clouds on Earth's climate wasn't fully understood [Bouter, L.M. et al., 2007; Bastiaan Van Dieden Hoven, 2007].

The incoming solar radiation is attenuated as it penetrates the atmosphere, reflects from the surface and travels back to space [Jagpal R.K. et al., 2010; Siddiqui R. et al., 2015]. The most abundant greenhouse gas H_2O plays a very important part in radiative transfer within the clouds. This is because the water droplets in clouds can actually behave in two ways. Depending on the location and type of clouds their behavior is complex in nature and may vary considerably. At the lower altitude, the water droplets scattering the incident light cause very strong reflection (within entire wavelength spectrum) back into space, thus shielding the Earth [Mitchell, J., 2003]. The opposite is also true for the clouds located at higher atmosphere since their net effect traps outgoing IR radiation [Mitchell, J., 2003]. The attenuation appearing as a result of the water droplets in dense clouds contributes for the light extinction (scattering plus absorption) [Mao, J. et al., 2004]. Furthermore, the dense clouds also affect the path of photons travelling through the atmosphere that ultimately changes the depth of absorption band.

Clouds interact both with solar radiation, in the shortwave (SW) region of the spectrum, and with the radiation thermally emitted by the Earth and atmosphere, in the longwave (LW) region. Clouds decrease the net absorption of solar radiation by increasing the Earth albedo and they decrease the loss of terrestrial radiation to space by decreasing the effective radiation brightness temperature of the Earth [Arking, A., 1991]. Longwave cloud feedback is systematically positive and nearly the same magnitude across all global climate models used in IPCC-AR5 [Zelinka, M.D., et al., 2010]. The longwave feedback effects mainly depend on cloud top temperature, which corresponds to the height especially for thin clouds [Arking, A., 1991].

In cloud retrievals from satellite datasets, it is very important to have a reasonable estimate of the surface albedo [Fournier, N., et al., 2006]. The reason is that the cloud detection is usually performed by comparing the measured reflectance with expected reflectance from cloud scene [Li, W., et al., 2008]. According to observational estimates from the International Satellite Cloud Climatology Project (ISCCP) data set [Gómez-Chova, L. et.al., 2007], the global mean cloud cover is around 70%. This substantial cover reflects a large amount of solar radiation, about 50 W/m^2 on an annual and global average [Stevens, B., 2011], which is a factor of ten larger than the radiative forcing effect appearing as a result of increased carbon dioxide (CO_2) concentration in the atmosphere. The tendency of clouds to reflect incoming solar radiation warms the planet, and is termed the albedo effect, shortwave effect, or shortwave cloud forcing [Stevens, B., 2011]. Figure 2.1 shows the significant contribution of clouds on atmospheric radiative transfer, both in magnitude and in the number of mechanisms by which they can affect the radiative budget of the Earth. Mainly, two types of cloud radiation budget can be eminent:

(i) Shortwave radiations from the sun are scattered in the clouds and many of them are reflected back to space. The resulting cloud albedo tends to cause a cooling of the Earth.

(ii) Longwave radiation emitted by the Earth are absorbed and re-emitted by clouds, with few radiations goes to space and some of them going to the surface. The resulting greenhouse forcing tends to cause a warming of the Earth.

The resulting balance term between these two effects may cause overall cooling or warming of Earth.

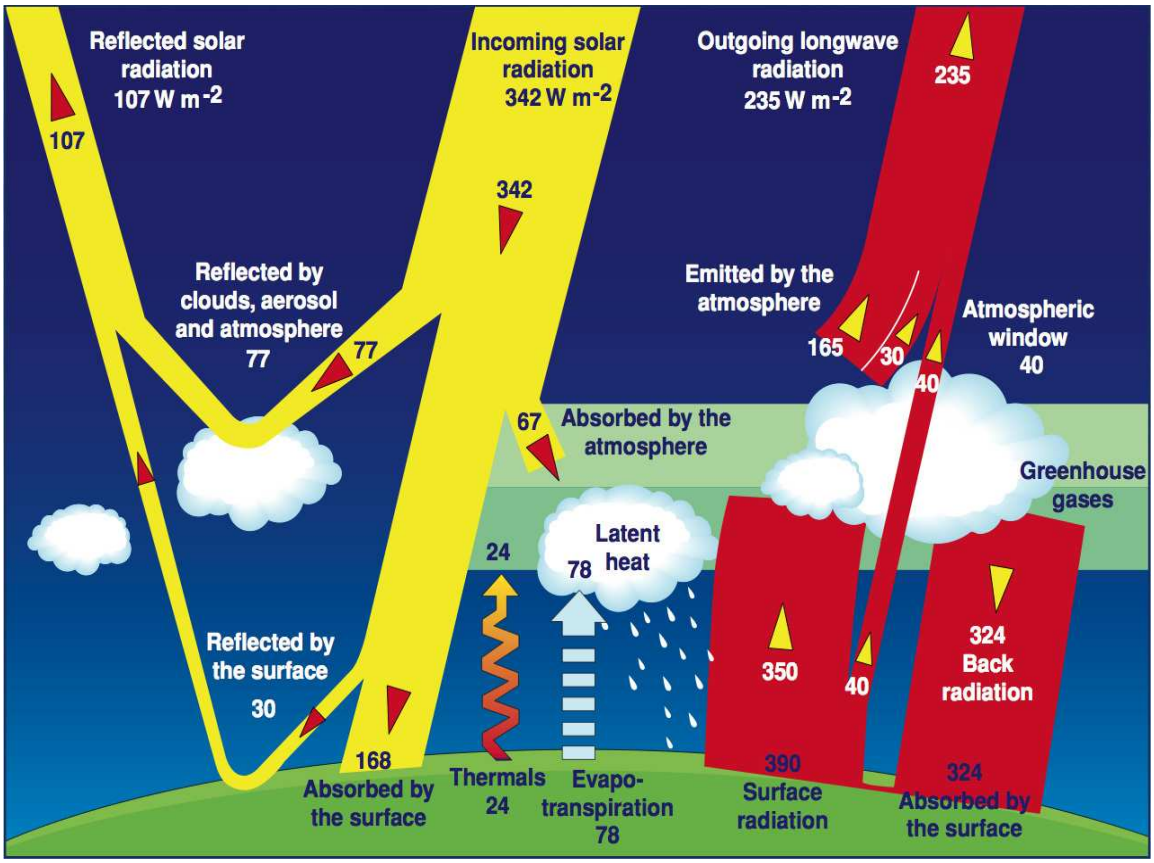

Fig. 2.1. Atmospheric radiative transfer global energy rate (W/m^2) [credits: Kiehl, J.T., 1992], [www.science.larc.nasa.gov/ceres/ 2013]

2.3 Cloud Formation

When air ascends, it cools adiabatically while retaining its specific humidity [Feather, O.R., 1971]. As the water vapor saturation pressure is a function of temperature, the relative humidity will increase until saturation is reached in the ascending air. If aerosols that can act as condensation nuclei are available, droplets will start to form and a cloud is created. As the air continues its ascent, it will cool further and the cloud droplets will start the transition from liquid phase to ice phase; the altitude where this occurs is called the freezing level [Murray, B.J., et al., 2012]. A cloud may be liquid, mixed or ice phase if its temperature is

between 0°C to -38°C [Yau, M.K. et al., 1976]. While the atmosphere has an abundance of aerosols that may act as liquid condensation nuclei, particles that are suitable as ice nuclei are much rarer. This lack of ice-forming nuclei is the main reason why liquid clouds don't immediately freeze when they reach temperatures below 0°C [Yau, M.K. et al., 1976]. Ice clouds can also be formed without liquid droplets by water vapor deposition onto an ice condensation nucleus, or by water vapor condensing to droplets at temperatures lower than about -38°C and then freezing homogeneously [Eliasson, S., 2013]. This happens, for instance, behind the exhausts of aeroplanes, since the exhaust contains both large amounts of water vapor and aerosols [Shonija, N.K., et al., 2007]. These clouds are known as condensation trails (commonly called contrails). When the Earth's surface heats up due to incoming solar radiation, the atmospheric layer closest to the ground will become buoyantly unstable [Eliasson, S., 2013]. The longer the heating process continues, the deeper the layer of instability will get and the more likely convection may be triggered. Most clouds generated by surface convection are cumulus clouds with cloud tops lower than the freezing level. These clouds are often inhibited in vertical extent due to a stable atmospheric layer above them. Sometimes, in sufficiently favorable conditions, convective clouds can grow into thunderstorms, which contain cloud water droplets below the freezing level and ice particles above it [Eliasson, S., 2013].

Thunderstorms generate ice clouds, called anvil clouds, that can be very widespread. A majority of ice clouds in the Tropics are thought to primarily arise from these storms and due to their high altitude and large vertical as well as

horizontal extent, they have substantial impact on the radiation budget [Evans, K.F., et al., 2002]. Convective storms typically have a lifetime of 30 minutes to more than one hour, whereas some thunderstorms may develop into mesoscale convective systems that can last many hours, or even days (for example, tropical cyclones) [Williams, J., 2009]. At mid latitudes, cirrus cloud is primarily generated by cyclones with frontal systems and in the jet streams [Chen, J. et al., 2002]. When the polar air moves towards the Equator while tropical air is moving towards North or South pole, Rossby waves are formed described by [Encyclopedia Britannica]. The geographical location and generation of mid-latitude cyclones and jet streams are largely governed by Rossby waves [Jensen, E. et al., 2004]. Clouds are formed when warmer, less dense air is forced upward by cooler, denser air at fronts associated with cyclone activity. These systems can be vast in area, extending over several hundreds of kilometers, impacting directly the surface and atmospheric radiation budget.

Clouds, can also be formed through orographic lifting. If air is forced to ascend over topographical features such as mountain ranges because of the prevailing winds, clouds will form where the air ascends and thereby cools enough so that the relative humidity reaches saturation and particles will condense. Although such clouds appear quasi-stationary, the cloud particles are in fact moving with the wind, often at high speeds [Eliasson, S., 2013]. The cloud appears stationary, since, as the saturated air descends along the lee-side of a mountain (and hence warms adiabatically), the downwind cloud particles evaporate when the air they are travelling in reaches the point of sub-

saturation [Eliasson, S., 2013]. However, on the windward-side new cloud particles are formed in the ascending, adiabatically cooling air. As long as the prevailing winds continue from more or less the same direction and the incoming air is sufficiently humid, clouds will continue to form at the same place. Orographic lifting can also create lee waves behind the mountain range if the atmosphere is stable [Eliasson, S., 2013]. These so-called wave clouds may then form in the ascending parts of the waves downstream from the mountains. This effect can cause considerable cloud amounts in mountainous regions such as the Himalayans and the Rocky Mountains [Pepin, N. et al., 2002].

2.3.1 Types of clouds and their characteristics

There are many different types of clouds which can be identified visually in the atmosphere. In 1804, L. Howard, established the terminology that forms the basis for modern cloud classification. Clouds may be classified by albedo, height and structure. When clouds are low enough to touch the ground, they are called fog [Erel, Y. et al., 1993]. For the classification of clouds Howard used Latin-based words to describe their characteristics [Mills, G., 2008]. These are: *cirrus* (meaning hair-like), *cumulus* (pile), *stratus* (layer), and *nimbus* (rain-producing). Each main classification may be further subdivided into ten main types, as shown in Figure 2.2. These can be divided into three main categories according to the altitudes of their base above the ground, as low clouds, medium clouds and high clouds [Cooper, S.J., et al., 2003]. These three main types are further subdivided on the basis of their structure, shape and degree of transparency.

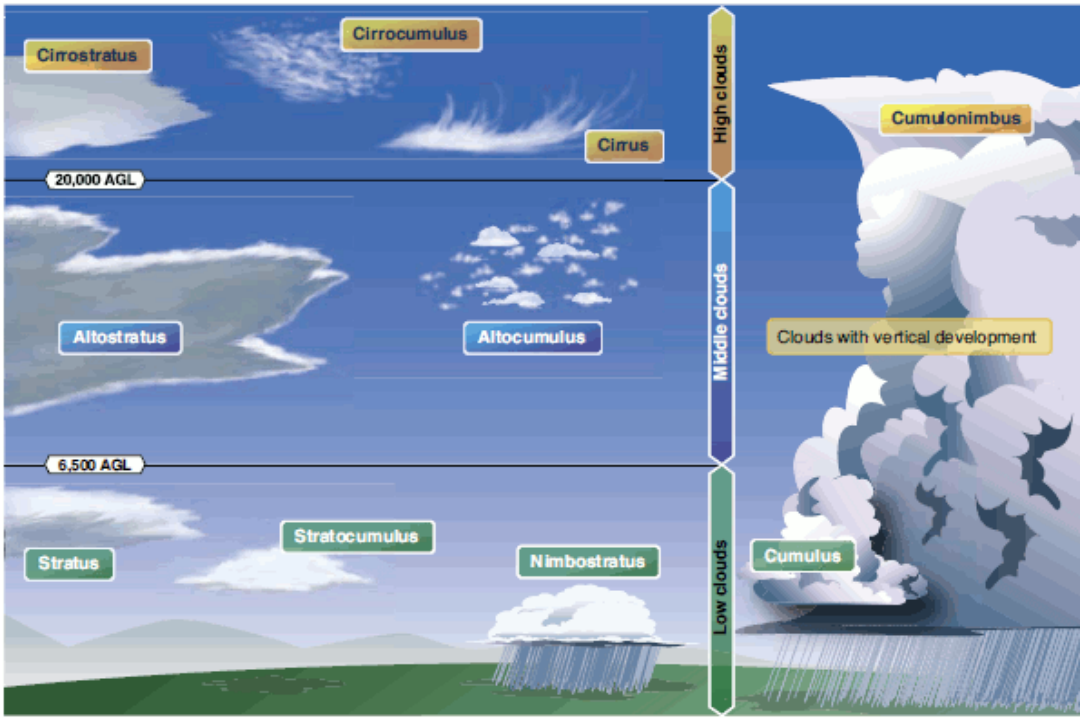

Fig. 2.2. Clouds categorized with respect to their height above ground level (AGL) [credits: Flight learning], [Wang, J., et al., 2005]

2.3.1.1 Low-level clouds

Low clouds are those that form near the Earth's surface and extend up to 2 km (6500 ft.) Above Ground level (AGL). These types of clouds are generally formed by water droplet condensation as air rises as a result of surface heating [Pacek, J.T., 1981]. They are made primarily of water droplets, but can also include supercooled water droplets. Typical low clouds types include:

- *Stratus clouds*: Evenly grey, low layer cloud, which causes fog or fine precipitation and is sometimes frazzled.
- *Stratocumulus clouds*: Cloud plaices, rollers or banks compound dark gray layer cloud.
- *Nimbostratus clouds*: Rain cloud. Grey, dark-layer cloud, indistinct outlines.

Clouds in this family create low ceilings, hamper visibility, and can change rapidly [Illman, P.E., 1995].

2.3.1.2 Middle-level clouds

These types of clouds typically form at temperatures between 0 to -40 ^{o}C and usually composed of supercooled water droplets and ice crystals [Heymsfield, A.J. et al., 1984]. Middle clouds form around 2 km and extend up to 6 km (20, 000 ft.) AGL. They are composed of water, ice crystals, and supercooled water droplets. Typical middle-level clouds include altostratus and altocumulus [Rossow, W.B. et al., 1999]:

- *Altostratus clouds*: Dense, gray layer cloud, often evenly distributed and opaque to solar radiation. These types of clouds can produce turbulence and may contain moderate icing (when temperature is below -2.2°C) [Kjerstad N., 2011].
- *Altocumulus clouds*: Grey cloud bundles, like sheds or rollers, compound like rough fleecy cloud, that are often arranged in banks. These types of clouds usually form when altostratus clouds are breaking apart. Also, may cause turbulence and icing.

2.3.1.3 High-level clouds

These clouds are typically observed solely in the form of ice crystals. High clouds form above 6 km AGL and usually form only in stable air. They are made up of ice crystals and pose no real threat of turbulence or aircraft icing. Typical high-level clouds are cirrus, cirrostratus, and cirrocumulus [Rossow, W.B. et al., 1999].

- *Cirrus clouds*: Fibrous, threadlike, white feather clouds of ice crystals, whose form resembles hair curls.
- *Cirrostratus clouds*: Milky, translucent cloud veil of ice crystals, which sometimes causes halo appearances around moon and Sun.

- *Cirrocumulus clouds*: Fleecy cloud; cloud banks of small, white flakes.

2.3.2 Ice particles

Ice particles in clouds are significant in precipitation formation, and they have a great impact on the Earth's radiation budget [Hobbs, P.V. et al., 1964]. A crucial process in our understanding of cloud particle formation is the initiation of a new phase, for example, the transition of water from vapor to liquid or solid phases. The rates of "vapor-to-liquid" and "vapor-to-ice" phase transitions are determined by vapor supersaturations with respect to liquid or ice, respectively [Korolev, A.V., et al., 2003]. Cirrus clouds may be formed at temperatures lower than 238 K, by homogeneous and heterogeneous nucleation mechanisms [O'Shea, S.J., et al., 2016]. Large and thin hexagonal-plate ice crystals discovered in low concentrations near the tropical tropopause indicate the presence of particles that can act as ice nuclei at low supersaturations with respect to ice [Lohmann, U., et al., 2008]. The predominant processes for ice formation in the atmosphere depend on temperature (which changes with altitude) and the relative humidity. as shown in Figure 2.3. In low-level mixed-phase clouds (composed of water droplets and some ice particles), freezing may occur most effectively when supercooled water droplets come into contact with Ice-Nucleating Particles (INPs) [DeMott, P.J., et al., 2016]. In mid-level mixed-phase and ice clouds, water vapor condenses on INPs, or INPs become immersed in water droplets, after which ice crystals form [DeMott, P.J. et al., 2016]. Ice crystals can also form when INPs are immersed in supercooled drops of solutions (of salts or of organic compounds, for example), or by direct deposition of ice on the particles. High-level ice clouds include ice that forms "homogeneously" when supercooled droplets freeze or water

vapor crystallizes in the absence of INPs. This whole process is well-understood and explained [Russell, L.M., 2015; Wilson, T. W., et al. 2015].

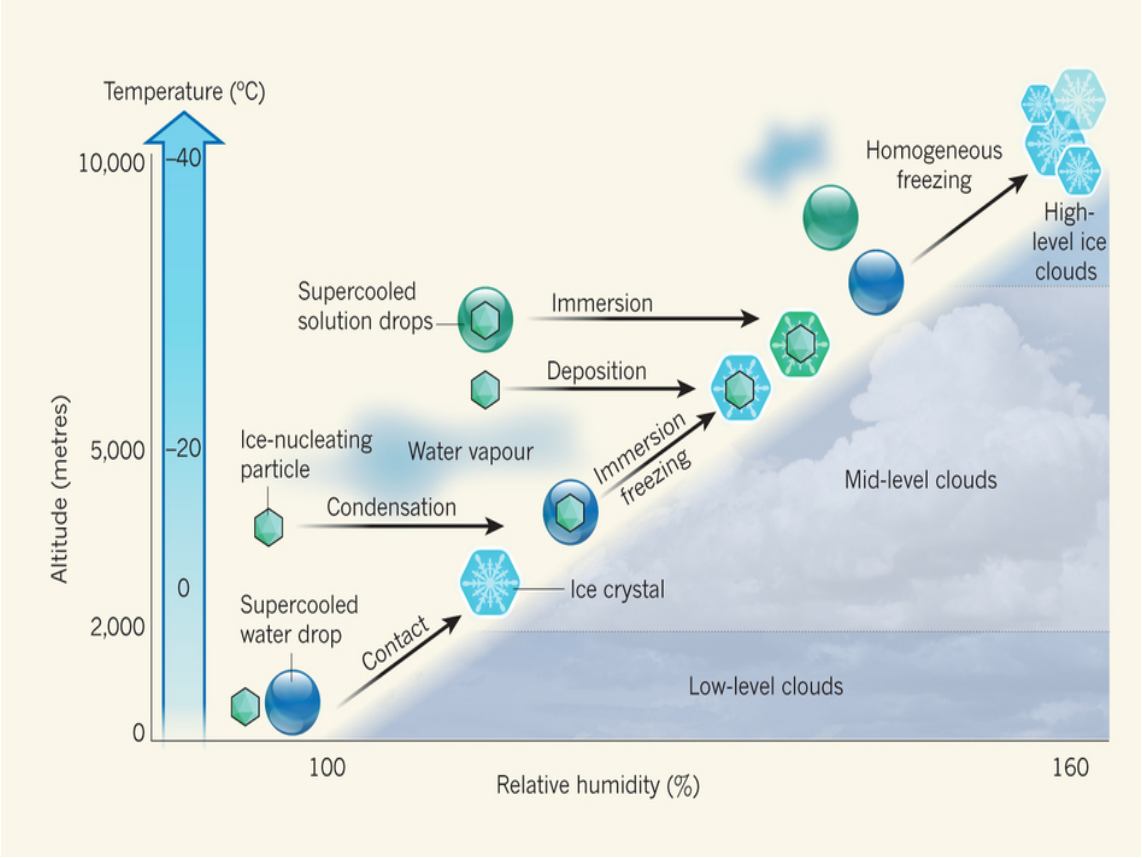

Fig. 2.3. Ice particle formation in different layers of clouds [credits: nature by Lynn M. Russell]

2.3.3 Cloud properties

The properties of clouds vary with location, time-of-day, and season. Because of these changing characteristics, satellite data can play an important role in detecting cloud scenes by measurement the reflection of solar radiation [Aggarwal, S., 2004]. The most important cloud properties for any remote sensing observations are the albedo, atmospheric concentration of greenhouse gases, and cloud height [Schuessler, O., et al., 2014].

2.3.3.1 Albedo

Albedo is a measure of the reflectivity of a surface. The albedo effect when applied to the Earth is a measure of how much of the Sun's energy is reflected back into space. It is the most important parameter for the efficient detection of cloud scenes, as well as for energy budget studies. Cloud albedo is a measurement of the amount of radiation that is reflected from the cloud's surface [Fritz, S., 1949]. The albedo of clouds varies from 10% to 90 % depending upon the type of cloud [Gómez-Chova, L., 2008]. It also depends on the liquid water vs. water vapor contents, size of the cloud droplets, and solar Sun angle. The type of surface (land, ocean, cloud, or ice) greatly influences Earth's albedo. Clouds are particularly significant to Earth's albedo because of their relatively high reflectivity and since they cover a significant portion of the Earth [Amy Elizabeth Chang et al. 2008; Salter, S., et al., 2008].

2.3.3.2 Optical thickness

Optical thickness is a determining factor in a cloud's radiative effect or opacity [Zeng, S., et al., 2012; Jensen, E.J. et al., 1994; Kristiansen, J., et al., 1999]. The variations in cloud optical thickness alter the ratio between transmitted and reflected radiation causing variation in the energy that reaches Earth's surface [Gómez-Chova, L., 2008]. Clouds that allow transmission of the majority of solar insolation are considered optically thin, while clouds that reflect the majority of the incident solar radiation are considered optically thick. The intensity of thermal emission of a cloud also depends on its optical thickness, as well as temperature. [Gómez-Chova, L., 2008].

2.3.3.3 Altitude

The altitude of a cloud base may range anywhere from ground level to almost 10 km above the surface, and the various types of clouds with their respective heights have been already explained in section 2.2.1. For the robust detection of cloud scenes, the height is an important input parameter for any cloud detection model.

2.4 Earth's Atmosphere

Earth is surrounded by an atmosphere consisting of a mixture of gases and other solid particles. The most abundant species in the atmosphere is nitrogen (N_2), which accounts for 78% of the air molecules. Next in abundance comes free oxygen (O_2), which represents 21% of atmospheric molecules. Other constituents include Argon (0.9%) [Jacob, D., 1999], followed by minor parts which are less than 0.04%. The atmosphere also contains solid and liquid particles such as aerosols, water vapor in clouds, and ice crystals in the form of snowflakes [Camps-Valls, G. et al., 2011]. The concentration and distribution of water vapor is largely variable (in contrast with for example, Argon gas), depending on location and time, and it can be rapidly removed from the atmosphere through rainfall [Arnaud C., 2016].

The vertical profile of the atmosphere is divided into four main layers: the troposphere, stratosphere, mesosphere, and thermosphere as shown in Figure 2.4.

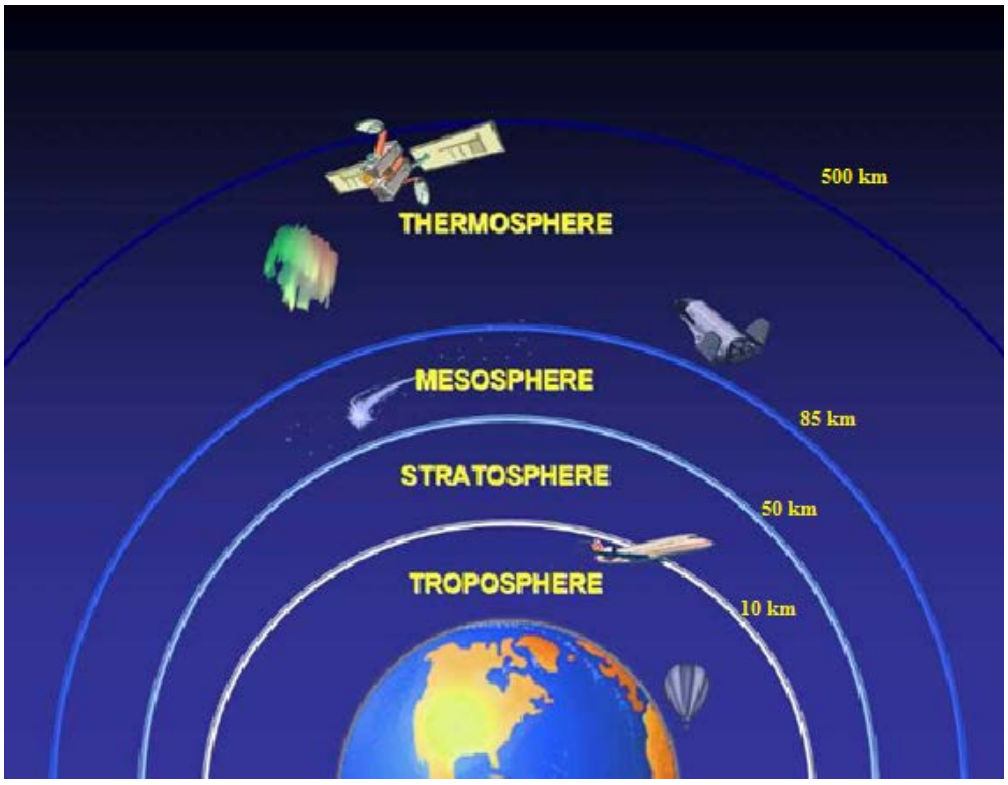

Fig. 2.4. Layers of the atmosphere

The tops of these layers are termed the tropopause (at 10 km), the stratopause (at 50 km), the mesopause (at 85 km), and the thermopause (between 500 to 1000 km). Gaseous materials extend to several hundred kilometers in altitude, though there is no well-defined limit of the atmosphere. All process related to clouds, water vapor and precipitation are confined to the troposphere. A layer of aerosol particles normally exists close to the Earth's surface. Finally, ozone is found mainly at the stratopause.

2.4.1 Atmospheric greenhouse gases

Greenhouse gases such as ozone (O_3), nitrous oxide (N_2O), methane (CH_4), carbon dioxide (CO_2), and water (H_2O) absorb and re-emit a significant amount of thermal radiation in the atmosphere compared to other gases, and are responsible for the greenhouse effect.

The Argus spectrometer records the only the NIR signature within 1100 to 1700 nm wavelength bands at the top of the troposphere to measure the atmospheric concentrations of various molecular species. The significant greenhouse gases that Argus can detect by their absorption and emission features are oxygen (O_2), carbon dioxide (CO_2), water vapor (H_2O) and methane (CH_4) [Jagpal, R. K., et al., 2010; Jagpal, R. K., et al., 2011]. The carbon monoxide (CO) is hard to get because of the low abundance at 1630 nm wavelength [Jagpal, R. K., et al., 2011]. Several different greenhouse gases are produced as by-products of complete or incomplete combustion of fossil fuels (for example, by running your car engine) and can be transported to the atmosphere. Many of these greenhouse gases have long lifetimes (on the order of years, decades, or even centuries); hence once released into the atmosphere they may have a long-term impact on atmospheric chemistry and radiative transfer. Water vapor is the most abundant greenhouse gas in the atmosphere, and a higher concentration of water vapor is able to absorb more thermal IR energy radiated from Earth's surface, thus further warming the atmosphere. The warmer atmosphere can then in turn hold more water vapor. This is referred to as a positive feedback loop. However, a large scientific uncertainty exists in defining the extent and importance of this feedback loop [NOAA]. As water vapor concentration increases in the atmosphere, this causes condensation into clouds, which are more able to reflect incoming solar radiation (thus allowing less energy to reach the Earth's surface and heat it up). The measurements of the atmospheric concentrations of other key greenhouse gases such as carbon dioxide and methane are well identified [IPCC, 2007a; Field, C. B. et al., 2014], the global concentration of water vapor is not known very reliably, so it is uncertain by how much atmospheric concentrations have risen in recent decades or centuries [NOAA].

Satellite measurements, balloon data and different ground based measurements, indicates normally positive trends in global water vapor [NOAA]. Now, clouds reflect solar radiation and reduce the amount of energy that reaches the Earth's surface to warm it, and if the amount of solar warming decreases, then the temperature of the Earth would decrease. In that case, the effect of adding more water vapor would be cooling rather than warming. But cloud cover does cause more condensed water in the atmosphere, making for a stronger greenhouse effect than non-condensed water vapor alone (it is warmer on a cloudy winter day than on a clear one) [Ervens, B., 2015].

2.5 Satellite Remote Sensing

Remote sensing instruments are of two primary types, active and passive. Active sensors provide their own source of energy to illuminate the objects they observe. An active sensor emits radiation in the direction of the target to be investigated. The sensor then detects and measures the radiation that is reflected or backscattered from the target. Passive sensors, on the other hand, detect natural energy (radiation) that is emitted or reflected by the object or scene being observed. Reflected solar radiation is the most common source of radiation measured by passive sensors [NASA, Earth data].

In order to understand observation of the atmospheric state, one can trace how radiation emitted from the Sun travels through space, arrives at the top of Earth's atmosphere, interacts with the different particles within the atmosphere and then reaches the surface. Information about these atmospheric constituents and surface properties can be extracted from ground observations of the backscattered solar radiation [van Diedenhoven, B., 2007]. Reflected solar energy is measured over a range of wavelengths and the resultant spectrum is analyzed. This method can

provide high temporal rate information but is difficult to apply over a large spatial scale. The advantage of satellite remote sensing in comparison to in situ measurements is that measurements of the whole globe can be made within a few days with the same instruments. The overall coverage is very important to study global changes in atmospheric concentrations, different cloud properties, detection of clouds, and for the measurement of trace gases at different remote locations. A satellite orbiting the globe can be used for a wide variety of measurements, depending of the specific type of instrument in its payload. Many different satellites now monitor the components of Earth surface, atmosphere, oceans and biosphere [van Diedenhoven, B., 2007]. These are known as Earth Observations (EO) satellite, whose instruments may be either active or passive.

High-resolution infrared non-gas absorption spectra can be derived, for example, from the Atmospheric Trace Molecular Spectroscopy (ATMOS) experiment that is performed for evidence of cirrus clouds [Kahn, B.H., et al., 2002]. Another approach for detecting cloud scenes in terms of radiance can be measured by high spectral resolution using infrared sounders to identify clear channels of clouds [McNally, A.P. et al., 2003]. Alternatively, Cutillo and coauthors [Cutillo, L. et al., 2004] showed an approach by developing new methods and algorithms for processing radiance data for cloud detection. In the same year, Song and coauthors [Song, X., et al., 2004] suggested an application of the Moderate Resolution Imaging Spectroradiometer (MODIS) data for cloud detection that may be especially efficient for the infrared channels. This method is based on cloud imaging by multi-spectral synthesis with cloud indexing.

MODIS data for Clouds and the Earth's Radiant Energy System (CERES) are also widely used to classify cloud phases and their optical properties [Minnis, P., et al., 2005; Chylek, P. et al., 2006; Li, W. et al., 2008; Tang, H. et al., 2013; Guo, F., et al., 2015]. Multi-directional tests can be performed in order to detect clouds from the Sun-glint regions and patches of cloud [Cheng, T. et al., 2007].

A new method was introduced on basis of advanced very high-resolution radiometer (AVHRR) cloud mask data with a focus on highly active and highly reflecting targets (for example, the Baltic Sea). According to [Krezel, A. et al., 2011], these AVHRR cloud mask data are obtained from the statistic and histogram values of albedo and temperature maps. A threshold-based technique for cloud detection in Bangladesh and its surrounding areas has been developed based on National Oceanic and Atmospheric Administration Advanced Very High-Resolution Radiometer (NOAA - AVHRR) satellite time-series data [Ghosh, R.R., et al., 2012]. It has been shown that cloud detection, classification and motion determination are required for the forecast of cloud cover [Escrig, H., et al., 2013]. This study has been extended by High Resolution Geometrical (HRG) imagery for the reflectance properties of clouds within infrared and shortwave bands [Fisher, A., 2014]. Considering the importance of shortwave (SW) radiation during the past decades, we can see that more and more studies have been conducted for estimating surface radiation for the detection of clouds using MODIS data [Wang, T. et al., 2014; Mateos, D. et al., 2014].

The Argus 1000 is a micro-spectrometer that achieves space-based measurements of solar and thermal radiation absorption by major atmospheric trace gases [Jagpal R.K., 2011]. The Argus 1000 instrument, on board the CanX-2 satellite since 2008. It is

a passive optical remote sensor based on solar radiation that travels across the Earth atmosphere before being reflected by the any surface and then arriving at the instrument sensor. The study is carried out for cloud detection by using Argus 1000 micro-spectrometer by Radiance Enhancement (RE) technique within the selected wavelength bands of the observed signal [Siddiqui R. et al. 2015]. Moreover, high and low radiance enhancement of the reflected surface on the retrieved signal enables us to discriminate the cloudy and non-cloudy surfaces.

2.5.1 Survey of satellite-based NIR instruments

Since the launch of the first Television Infrared Observation Satellite (TIROS) in 1978, clouds have been continuously observed from space by weather satellites. TIROS evolved into the currently operational TIROS- N/NOAA and MetOp series, carrying the Advanced Very High-Resolution Radiometer (AVHRR). AVHRR is a space-borne instrument designed by the National Oceanic and Atmospheric Administration (NOAA) [Price J.C., et al., 1984]. The AVHRR instruments measure Earth's reflectance in different bands: from 600 to 1100 nm, 1600 to 3500nm, and 11000 to 12000 nm [Atkinson P.M., et al., 1997].

Other important present-day satellite instruments dedicated to the retrieval of cloud information are the Polarization and Directionality of the Earth's Repentances (POLDER) [Lorsignol J., et al., 1991], the Moderate Resolution Imaging Spectroradiometer (MODIS) [Justice C.O., et al., 1998], the Cloud-Aerosol Lidar and Infrared Pathfinder Satellite Observation (CALIPSO) [Gilbrech R.J., et al., 2005] and Cloudsat [Stephens G.L., et al., 2002]. The satellites carrying these instruments are all in polar orbits. Cloud observations from

geostationary satellites started in 1966 with the launch of the Applications Technology Satellite (ATS), which evolved into the Geostationary Operational Environmental Satellite (GOES) and MeteoSat series, of which several versions are currently operational [Bastiann van D., 2007]. There is currently no instrument operating in the same wavelength bands as Argus for the detection of cloud scenes, although a few space-based instruments work in a subrange of the Argus band, where clouds and other greenhouse gasses can be detected. A majority of nadir-viewing atmospheric sounder missions (prior to 2003) were not programmed to specifically detect the near-infrared (NIR) emission signatures of greenhouse gases such as CO_2 and CH_4. Consequently, these instruments were unsuitable for the observation of gas abundances in the surface-to-lower troposphere region, at a sufficient surface resolution to identify atmospheric constituents [Gottwald et al., 2006].

The Moderate-resolution Imaging Spectroradiometer (MODIS) was launched by NASA in 1999 on board the Terra Satellite [Barnes R.A., et al., 1999], and in 2002 on board the Aqua (EOS PM) satellite. Measurements are made in 36 spectral bands, ranging in wavelength from 400 nm to 14400 nm, at varying spatial resolutions (2 bands at 250 m, 5 bands at 500 m and 29 bands at 1 km). These two instruments were designed to provide measurements of large-scale global dynamics, such as changes in Earth's cloud cover, and radiation processes occurring over the oceans, on land, and in the lower atmosphere. Three on-board systems, a solar diffuser combined with a solar diffuser stability monitor (SDSM), a spectral radiometric calibration assembly (SRCA), and a v-grooved flat panel blackbody (BB), provide in-flight calibration [Barnes, W., 2006]. MODIS is one of the most versatile space-based instruments for atmospheric remote sensing [Barnes R.A., et al. 1999]. The MODIS cloud phase product (MOD06

for Terra and MYD06 for Aqua) is a combination of two different cloud phase detection methods, one using near-infrared and visible band ratios and the other the brightness temperature-difference of two thermal infrared bands [Chylek et al. 2006]. Only one of MODIS' NIR spectral bands (band 6, from 1630 to 1650 nm) works within the same region of the Argus spectrometer [Chylek P., et al. 2006]. These two instruments are designed to give dynamic information about Earth's cloud cover, radiative flux over the oceans, and within the different atmospheric layers, especially covering lower atmosphere.

The Orbiting Carbon Observatory (OCO), is designed to measure the same NIR spectral range. The wavelength band for OCO is 760-2060 nm, with three spectral channels [Chevallier F., et al., 2007]. The specified field of view is 14.6 mrad with a spectral resolution of 20,000 which is equivalent to 0.08 nm at 1600 nm. It cannot directly measure the concentration of carbon dioxide in the atmosphere. OCO-2 records the reflection of solar radiation by molecules in an air column [OCO-2 NASA web link]. OCO-2 makes measurements in three different spectral bands over four to eight different footprints of approximately 1.29 km × 2.25 km each [Parkinson C.L., et al., 2006]. One spectral band is used for column measurements of oxygen (the A-band at 0.765 microns), and two are used for column measurements of carbon dioxide (weak band at 1.61 microns, and the strong band about 2.06 microns) [Parkinson C.L., et al., 2006]. The measurement objectives of OCO are similar to those of Argus; however, this instrument is limited to three specific bands whereas Argus observes a broader spectral range (with lower spectral resolution), and can more efficiently detect cloud scenes [Siddiqui R. et al., 2015].

SCIAMACHY (Scanning Imaging Absorption Spectrometer for Atmospheric Chartography) is yet another satellite instrument developed to analyze atmospheric

concentrations of ozone, methane, carbon monoxide and other trace gases [Bracher, A. et al., 2005]. SCIAMACHY is one of ten instruments on the European Environmental Satellite (ENVISAT), launched in 2002 by the European Space Agency (ESA). SCIAMACHY is a grating spectrometer which measures both Earth's radiance (for example solar radiation reflected by Earth's surface and its atmosphere) and the solar irradiance, in six continuous bands in the wavelength range 240–1750 nm, and 2 additional bands in the wavelength ranges 1940–2040 nm and 2265–2380 nm. The ratio of terrestrial radiance and solar irradiance is commonly referred to as reflectance. The spectral resolution ranges from 0.22 nm to 1.48 nm, and the transmission efficiency of the instrument is sensitive to the polarization of the light. SCIAMACHY can measure either in a nadir-geometry (looking downwards) or in a limb-geometry (looking through the limb of the atmosphere). In its nominal operating mode, nadir- and limb-view measurements are alternated, each taking place about 50% of the time. SCIAMACHY records nadir spectra in bands at a spatial resolution of 30 km^2 and provides near real-time H_2O, NO_2, CO, N_2O and CH_4 profile data [Sussmann, R., et al., 2005]. Figure 2.5 shows the various space instruments working in the spectral region of 900 nm to 1700 nm where clouds and other species of the atmosphere can effectively be detected.

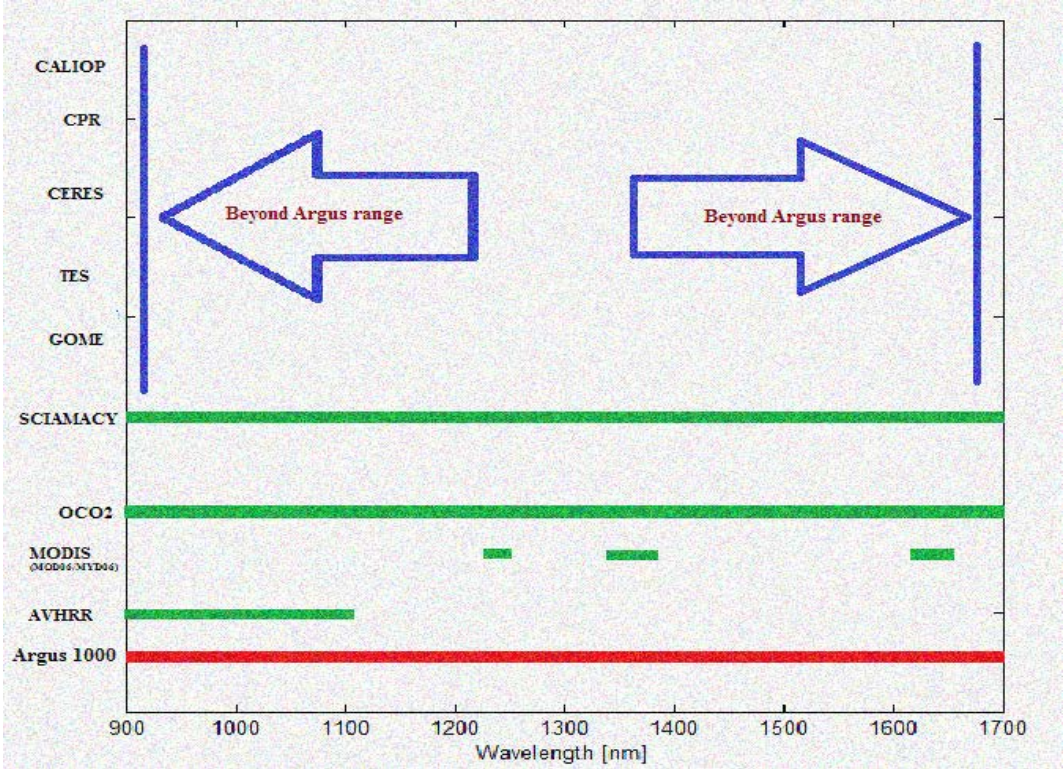

Fig. 2.5. Near Infrared space instruments (see Table 3.5 for source per references of estimates).

The Global Ozone Monitoring Experiment (GOME) [Burrows J.P., et al., 1999] is an instrument like SCIAMACHY, launched in 1995 on the second European Remote Sensing Satellite (ERS-2). It is a scaled-down version of SCIAMACHY, covering a smaller wavelength range (240–790 nm), and observes only in nadir-view with a footprint size of 320×40 km^2 [Koukouli, M., et al., 2012]. An improved version of GOME, GOME-2, was launched by EUMETSAT in 2006, on the first Meteorological Operational spacecraft (MetOp-A). GOME-2 has a footprint size of 80×40 km^2. Another instrument similar to GOME and SCIAMACHY is the Ozone Monitoring Instrument (OMI) [Levelt, P.F., et al., 2006]. OMI is a Dutch-Finnish instrument launched on NASA's EOS-Aura satellite in 2004. OMI measures in the wavelength range 270-500 nm and has a spatial resolution of about 13×24 km^2.

The Clouds and the Earth's Radiant Energy System (CERES) instrument is one of several flown aboard the Earth Observing System's Terra spacecraft, launched in late 1999. The CERES footprints are 25 km in diameter near nadir, with 400-2000 nm (total), 400 – 4500 nm (SW) and 8000-12000 nm, channels. The data from the CERES instrument were designed to investigate the top of atmosphere (TOA) shortwave (SW) and longwave (LW) radiative energy fluxes of the Earth-atmosphere system [Wielicki, B.A., et al., 1998] and are used to study the energy exchange between the Sun, atmosphere, surface, clouds, and outer space. CERES measures broadband reflected solar radiation and infrared thermal emission [Lin, B., et al. 2010]. Among many successful applications of CERES and ERBE data is the study of shortwave aerosol direct radiative forcing (SWARF) [Satheesh, S. K., et al., 2000; Loeb, N. G., et al., 2002; Christopher, S. A., et al., 2002a].

The GOMOS (Global Ozone Monitoring by Occultation of Stars) instrument was launched March 1, 2002 on board the European Space Agency's Envisat satellite. It is designed to measure O_3, NO_2, NO_3 neutral density, aerosols, H_2O, and O_2 in the stratosphere and mesosphere by detecting absorption of starlight in ultraviolet (UV), visible (VIS), and near infrared (NIR) wavelengths [Kyrölä, E., et al., 2004]. GOMOS operates in the ultraviolet- visible wavelengths 250–690 nm, with two channels are in the near- infrared at 750–776 nm and at 916–956 nm. It sits in a polar, Sun-synchronous orbit at an altitude of 800 km, with spectral resolution of 0.6 nm [Bracher, A., et al., 2005]. The primary goal of GOMOS is to accurately detect stratospheric ozone, in order to monitor long-term global trends in the abundance of this species. Detailed

information about the GOMOS instrument and its specifications may be found in [Nett, H., et al., 2001].

The CloudSat and CALIPSO satellites carry the onboard sensors CPR [Stephens, G.L., et al., 2002] and CALIOP [Winker, D.M., et al., 2009], respectively. Both of these instruments can measure different clouds on A-Train mission satellite [Stephens, G.L., et al., 2002]. The CPR is a nadir-viewing instrument with an effective horizontal resolution of 1.4 km [Stephens, G.L et al., 2008], while CALIOP is a near-nadir-viewing lidar instrument [Winker, D.M., 2003] with operating wavelengths centered at 532 nm (for thin clouds) [Vernier, J.P., et al., 2009] and 1064 nm (for aerosols) [Vernier, J.P., et al., 2009]. An overview of all of the previously mentioned satellite instruments is given in Table 2.1.

Table 2.1. Characteristics of satellite instruments

Payload	Spacecraft	Launch year	Spectral range (nm)	Spatial resolution (km)	Field of view (FOV) (degree)	Argus overlap range (nm)	Trace gases and cloud information's
Argus1000	CanX-2	2008	900-1700	1.4	0.125	900-1700	Land, ocean, atmospheric product (O_2, H_2O, CO_2, CH_4), upwelling radiative flux, detect and classify clouds
AVHRR	TIROS-N	1978	600-1100 1600-3500 11000-12000	1.09 1.09 1.09	0.080 0.083 0.080	900-1100 1600-1675 beyond	Surveillance of land surfaces, ocean state, aerosols etc., thermal emission of Earth, and cloud cover
MODIS-MOD06 (NIR/VIS) MODIS-MYD06	TERRA AQUA	1999 2002	400-14400	0.25 (2 bands), 0.50 (5 bands), 1.0 (29 bands)	Each band with different FOV	1230-1250 1360-1390 1628-1652	Water vapor Land cover classification, clouds and aerosols properties, surface temperature, ozone, cloud-top altitudes
OCO-2	OCO	2014	760-2060	1.29-2.29	0.80	900-1700	Measure only atmospheric CO_2 by reflection of solar radiation.
SCIAMACY	ENVISAT	1999, 2002	240-1750 (6 bands), 1940-2040 2265-2380	30x27 20x240	0.045x1.8	900-1700	Measure CO_2, aerosols and clouds detection, snow and ice detection
GOME GOME2	ERS-2 EUMESAT	1995 2006	240-790	80x40	0.01x0.02	beyond	Ozone, NO_2, SO_2, O_2, H_2O and aerosols
TES	EOS-AURA	2004	270-500	0.5x5	0.023	beyond	Measure tropospheric ozone, CO_2, NO and CH_4
CERES	TERRA AQUA	1999	300-5000 8000-12000	20	± 0.78 cross track	900-1700 Beyond (high spatial)	Measure Earth radiation budget and clouds properties
CPR	CLOUDSAT	2002	94-GHz	1.4 radar	0.16	beyond	Measure power back track by clouds as a function of distance
CALIOP	CALIPSO	2006	532 & 1064	0.33 and 0.03 (vertical and horizontal resolution) lidar	0.007	beyond	Cloud profile information on upper troposphere and altitudes of aerosols
CALIOP	IIR	2006	8650, 10600 & 12000	64x64 swath	N/A	beyond	Cloud profile information on upper troposphere and altitudes of aerosols

Of the instruments listed above, Argus 1000, AVHRR and MODIS (with two bands) all work within overlapping spectral ranges, measuring NIR radiation with spatial and spectral resolution suitable for atmospheric water vapor and cloud detection. The spectral range, along with spatial resolution and instrument FOV, are critical factors in the selection of their comparisons with different cloud detection techniques [Simpson J.J., et al., 1999]. Sensors with narrow spectral windows beyond 1000 nm have demonstrated an effective capability of detecting high clouds because of the strength of water vapor absorption [McIntire, T.J., et al., 2002; Gao B.C., et al., 1998]. In the spectral range of 1380 nm to 1500 nm, both high and lower level clouds can be seen with the elimination of additional absorption features of water vapor [Luis Gomez, 2007]. The RE and SWupRF results to detect cloud scenes by Argus are compared with the MODIS clouds imageries.

2.6 Electromagnetic Radiation and Radiative Transfer

2.6.1 Electromagnetic radiation

The Sun's energy has traveled across space as electromagnetic (EM) radiation and arrives at the top of Earth's atmosphere, where it interacts with various atmospheric constituents before reaching the surface. Electromagnetic radiation is described in terms of its wavelength, frequency, or energy, and includes infrared radiation, radio waves, visible light, and ultraviolet rays. All electromagnetic energy travels at the speed of light, c, which is 2.998×10^8 m/s, so wavelength (λ) and frequency (ν) are inversely related: $c = \lambda\nu$. The wavelength and frequency also indicate the energy of the wave. The relationship between wavelength and energy, E, is described by the equation, $E = hc/\lambda$, where h is

Planck's constant ($h = 6.625 \times 10^{-34}$ Joule-seconds or J s), and c is the speed of light. By replacing the constants h and c with their respective values, we see that $E = 1.986 \times 10^{-25}$ Joules-meters. An inverse relationship also exists; electromagnetic radiation with shorter wavelengths is more energetic. The relationship between energy, E, of the photon and frequency, f, is given by, $E = hv = \hbar w$, where $\hbar = h/2\pi$ is the reduced Planck's constant and $w=2\pi f$ its angular frequency. The electromagnetic spectrum is a continuum of all electromagnetic waves arranged according to frequency or wavelength which are defined as the number of wave peaks passing a given point per second and the distance from peak to peak, respectively. The spectrum is divided into region based on wavelength ranging from short gamma rays, which have wavelength of 10^{-6} μm or less, to long radio waves that have wavelength of many kilometers. Figure 2.6 shows a detailed breakdown of the electromagnetic spectrum, including the visible light (VIS) region with wavelengths from 400 to 700 nm (for example from blue to red) and the adjacent infrared (IR) region. These two regions of the EM spectrum are most commonly used in passive remote sensing, and the infrared band may be subdivided into energy waves (EWR), near infrared (NIR), shortwave infrared (SWIR), middle infrared (MIR), and thermal infrared (TIR) regions.

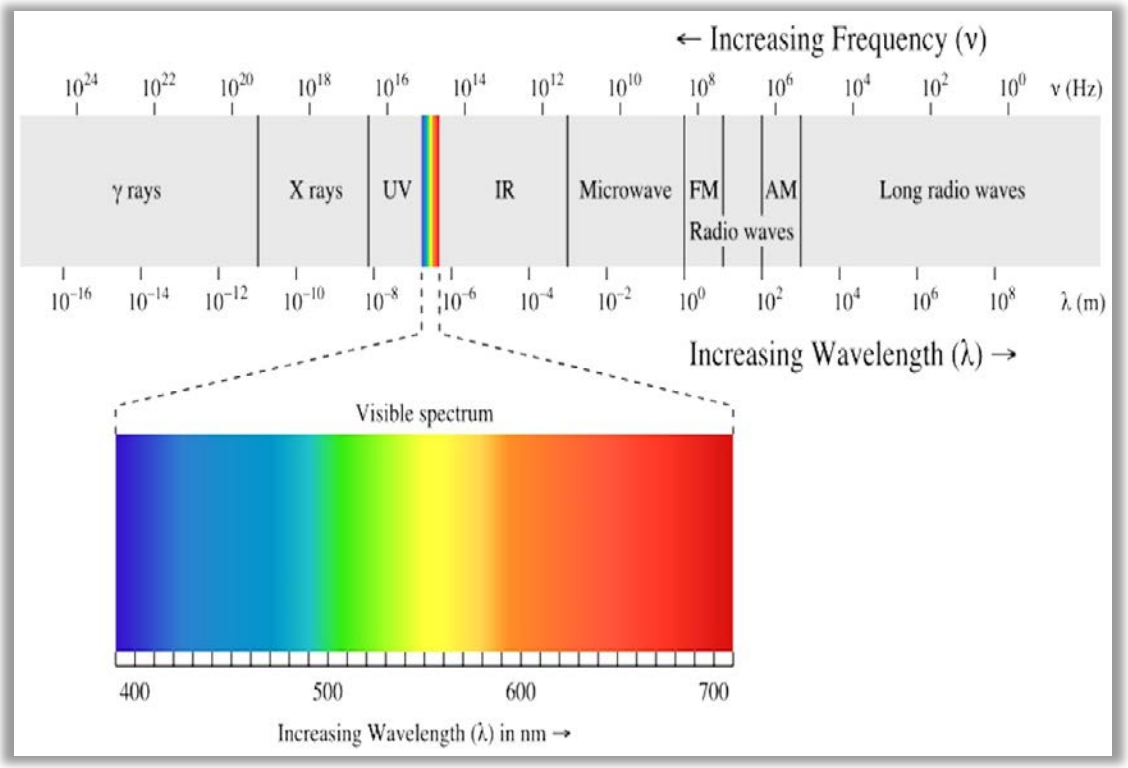

Fig. 2.6. The electromagnetic spectrum.

The predominant type of radiance detection in the wavelength band from 400 to 3000nm (VNIR and SWIR) is based on measurement of reflected solar radiation [Gómez-Chova, L., 2008]. This region is commonly used for cloud detection [Tang, H., et.al., 2013].

The rate of energy transfer per unit area by EM radiation is called the radiant flux or irradiance (W/m^2). The quantity often used in remote sensing is the irradiance per unit wavelength, or spectral irradiance ($W/m^2/nm$). The total radiant energy from the Sun is approximately 3.84×10^{26} W while the mean Earth-Sun distance is 1.496×10^{11} m. The total solar irradiance (incident at the top of the atmosphere, over all wavelengths, at normal incidence to the Earth surface) is therefore $F_0 = (3.84 \times 10^{26})/4\pi$

$(1.496 \times 10^{11})^2$ = 1370 W/m^2. This value is known as the solar constant, although it presents a significant variation with time [Gómez-Chova, L., 2008].

Space-borne instruments enable us to measure the spectral variations in solar irradiance at the top of the atmosphere (TOA), without the effects of Earth's atmosphere which, depending on wavelength, can reduce the intensity of measured radiation. The spectral distribution of solar radiation, or extraterrestrial solar spectrum, incident on the TOA is shown in Figure 2.7 in the spectral region of interest for the Argus instrument. The trend of the solar intensity curve follows the Plank distribution $B(\lambda, T)$ as given by Eq. (2.1), for a black body at temperature T= 5780 K.

$$B(\lambda, T) = \frac{2\,\hbar c^2}{\lambda^5 [\exp\left(\frac{\hbar c}{\lambda k_B \mathrm{T}}\right) - 1]} \qquad (2.1)$$

where k_B is the Boltzmann constant (k_B = 1.38 x 10^{-23} J/K).

The interaction of this incoming radiation with Earth's atmosphere and its surface produces the emitted radiation measured by Argus. Absorption and scattering processes must be considered along both incoming and outgoing atmospheric paths, which depend on the Sun-Earth-satellite geometry, characterized by the solar zenith angle, satellite viewing angle and relative azimuth with respect to the point of observation.

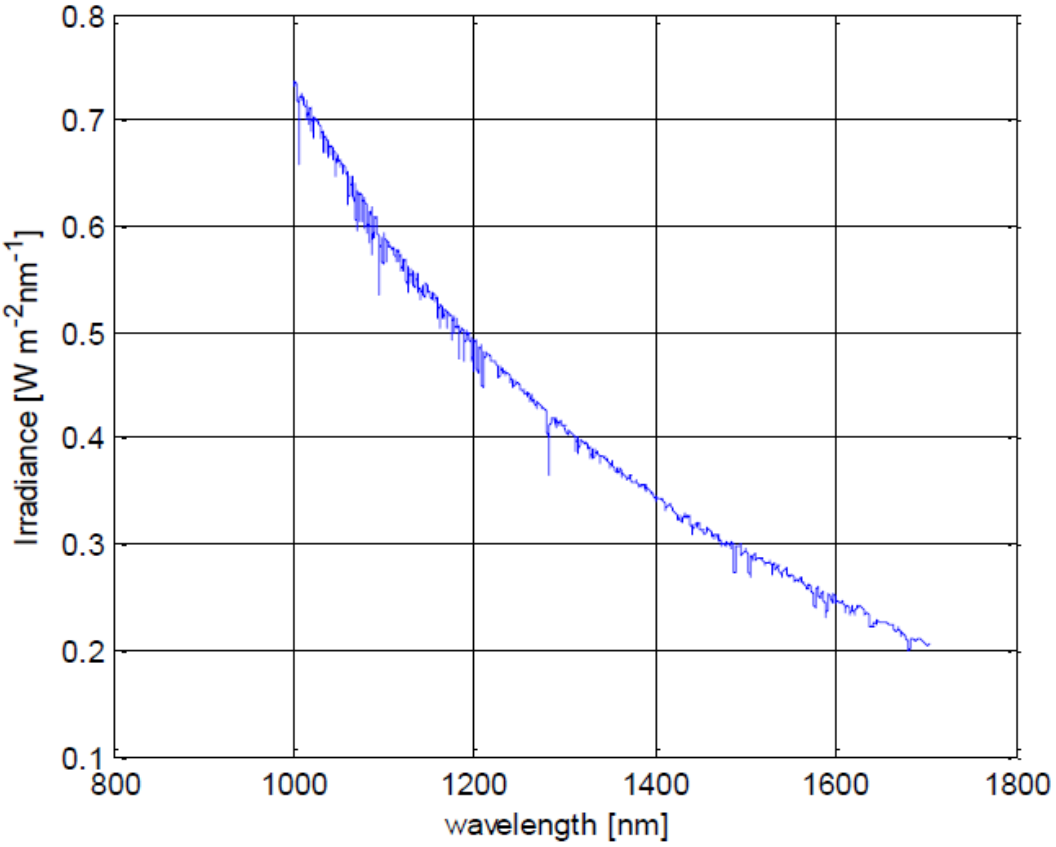

Fig. 2.7. Solar Spectrum in the Argus spectral window. Reproduced from the 2000 ASTM Standard Extraterrestrial Spectrum Reference E-490-00. [Jagpal R.K., 2011]

In this work, remote sensing within NIR wavelength spectrum of Argus 1000 spectrometer has been applied for the efficient detection of cloud scenes covering the 1100 to 1700 nm range.

2.6.2 Radiative transfer

In this section, the interaction of solar irradiance with the atmosphere is described by a simplified version of the radiative transfer equation in order to quantify the different contributions to the observed signal in the instrument.

2.6.2.1 Radiometric quantities

The theory of radiative transfer involves various radiometric quantities. The radiant power ϕ (W) is the total radiative flux, incident from all directions, intercepted by a surface, while the directional radiant intensity I, given by Eq. (2.2), is a differential flux, defined as the power received per unit solid angle Ω (measured in stereoradians, sr) subtended by the surface,

$$I = d\phi/d\Omega \text{ (W/sr)}. \qquad (2.2)$$

The irradiance (or flux density) E, given by Eq. (2.3), is defined as the intercepted radiant power per unit surface area,

$$E = d\phi/dA \text{ (W/m}^2\text{)}. \qquad (2.3)$$

The radiance L, given by Eq. (2.4), is a directional angular-area flux density, defined as the intercepted power per unit area per unit solid angle,

$$L = d^2\phi/ (d\Omega\, dA) \text{ (W/m}^2\text{/sr)}. \qquad (2.4)$$

Finally, the spectral radiance L_λ is the radiance per unit wavelength (W/m^2/sr/nm), and is the quantity commonly used in radiative transfer calculations. There is also a corresponding spectral irradiance E_λ with units of (W/m^2/nm)

2.6.2.2 Radiance at TOA

Consider for example the geometry in Figure 2.8, and take the horizontal plane to be the x- y plane. The net downward radiation incident on the infinitesimal area element dA is made up of radiation pens (cone shapes), each coming from different polar angle θ and azimuthal angle ϕ. Calculating the spectral irradiance E_λ is then a matter of integrating over all

these pencils of infinitesimal solid angle dΩ, and projecting onto the normal to the surface: $L\lambda \rightarrow L\lambda \cos\theta$. Thus,

$$E(\lambda) = \int L(\lambda, \theta, \phi) cos\ \theta d\Omega \qquad (2.5)$$

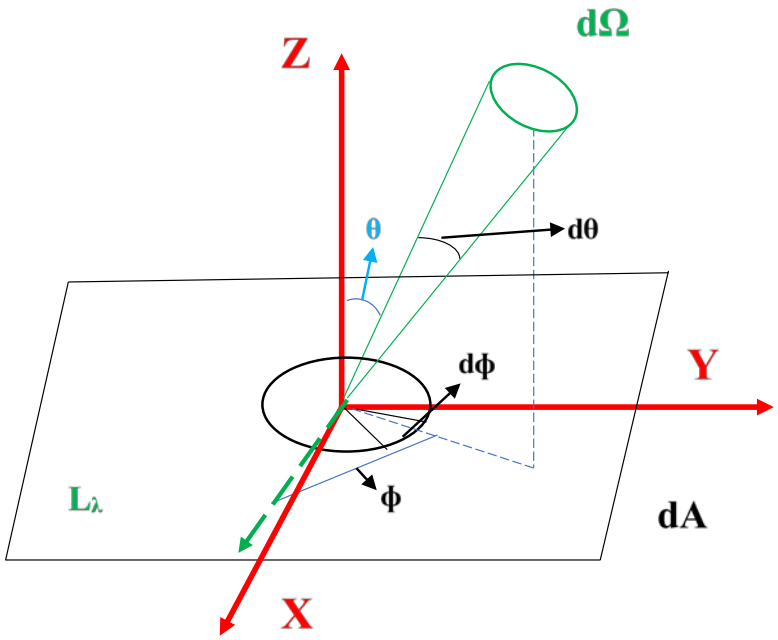

Fig. 2.8. Geometry for the calculation of spectral irradiance: a pen-shaped green cone of L_λ propagating downward (green dashed arrow) across the horizontal plane at an angle θ.

Using $d\Omega = \sin\theta d\theta d\phi$, Eq. (2.5) can be written as

$$E(\lambda) = \int_{\phi=0}^{2\pi} \int_{\theta=0}^{\pi/2} L(\lambda, \theta, \phi)\ cos\theta sin\theta d\theta d\phi \qquad (2.6)$$

If the radiation is isotropic (for example $L\lambda$ is independent of θ and Φ), then the integral of Eq. (2.6) simplifies to:

$$E(\lambda) = 2\pi L\lambda \int_{\theta=0}^{\pi/2} cos\theta sin\theta d\theta \ = \pi L\lambda \qquad (2.7)$$

Eq. 2.1 is exact for Blackbody radiation, for which $L\lambda = B\lambda$ as discussed in section (2.4.1). Eq. (2.7) can be rearranged to give the expression for the spectral radiance:

$$L(\lambda) = \frac{E(\lambda)}{\pi} \qquad (2.8)$$

2.6.2.3 Radiation extinction

The absorption and the scattering responsible for the loss of energy in a particular direction can be treated as two separate processes, and their combined effect is known as radiation extinction. The extinction of the radiation can be described by means of the Bouguer-Lambert-Beer law, which is defined by a simple differential equation that assumes that the radiance loss is proportional to the total energy amount and to the distance traveled through the interacting material. If we consider a layer of thickness dp in an absorbing and scattering medium perpendicular to a radiation beam of radiance L, after passing through the material, the radiance is reduced by an amount dL given by Eq. (2.9):

$$dL = -\beta_e(p)Ldp \qquad (2.9)$$

where β_e is the volume extinction coefficient, which is the sum of the volume absorption and scattering coefficients. If we integrate between two positions, p_1 and p_2, we have:

$$L(p_2) = L(pz_1)exp(-\int_{p_1}^{p_2} \beta_e(p)dp) = L(p_1)e^{-\tau} \qquad (2.10)$$

where τ is called optical thickness including volume extension coefficients. Eq. (2.10) is known as Beer's exponential extinction law, and yields an expression for

the transmittance T (p_1, p_2) of the layer between p_1 and p_2 along the direction of propagation as given by Eq. (2.11):

$$T\ (p_1, p_2) = \frac{L(p_2)}{L(p_1)} = e^{-\tau} \tag{2.11}$$

From an altitude p above the Earth's surface to the TOA, the total optical depth is calculated by Eq. (2.12):

$$\tau_{tot}\ (\lambda) = \int_p^{\infty} \beta_e(\lambda, p) = \int_p^{\infty} k_{tot}(\lambda)\delta_{atm}(z)dz \tag{2.12}$$

where $k_{tot}(\lambda)$ is the total extinction coefficient and δ_{atm} is the intervening atmosphere between p and TOA. The solar intensity measured at the Earth's surface assume the form of the extinction Bouguer-Lambert-Beer law as described by Eq. (2.13):

$$L_s\ (\lambda) = L_0\ (\lambda) \exp(-\ \tau_{tot}\ (\lambda)) \tag{2.13}$$

2.7 The GENSPECT Radiative Transfer Model

Thoth Technology's GENSPECT software package computes the absorption and emission of radiation as it passes through the gases in a model atmosphere, based on spectral line data and associated physics. The software is able to estimate the spectral effect of changes in near-surface gas concentrations, and this information can be used in an inversion algorithm to estimate the composition of the atmosphere based on space-based observations. The GENSPECT toolbox has been successfully employed in the analysis of satellite data from the Measurement of Pollution in the Troposphere (MOPITT) instrument [McKernan, E., et al., 2002] and is used as the basis for development of data-processing routines to retrieve gas amounts in this thesis. GENSPECT incorporates a line-by-line

radiative transfer algorithm for the modeling of absorption, emission, and transmission characteristics of a wide range of atmospheric gases. The code uses a variable frequency grid to compute absorption parameters to a specified accuracy [Quine, B. M. et al., 2002]. High Resolution Transmission (HITRAN) line strengths [Duggan, P., et al., 1993] are pre-adjusted for normal isotopic abundances and tabulated to model an Earth atmosphere with natural abundance. Given information including gas types and amounts, pressure, path length, temperature, and frequency range for an atmosphere, the GENSPECT model computes the spectral characteristics of the gas. GENSPECT employs a unique computation algorithm that maintains a specified accuracy for the calculation by pre-computing where a line function may be interpolated without a reduction in accuracy [Quine, B. M. et al., 2002].

The typical GENSPECT computation points near line center. The pre-computed points are denser close to the central part of the Voigt function [Abrarov, S. M., et al., 2010a] and thin at its annexes as shown in Figure 2.9, where the points with its corresponding grids are linearly interpolated.

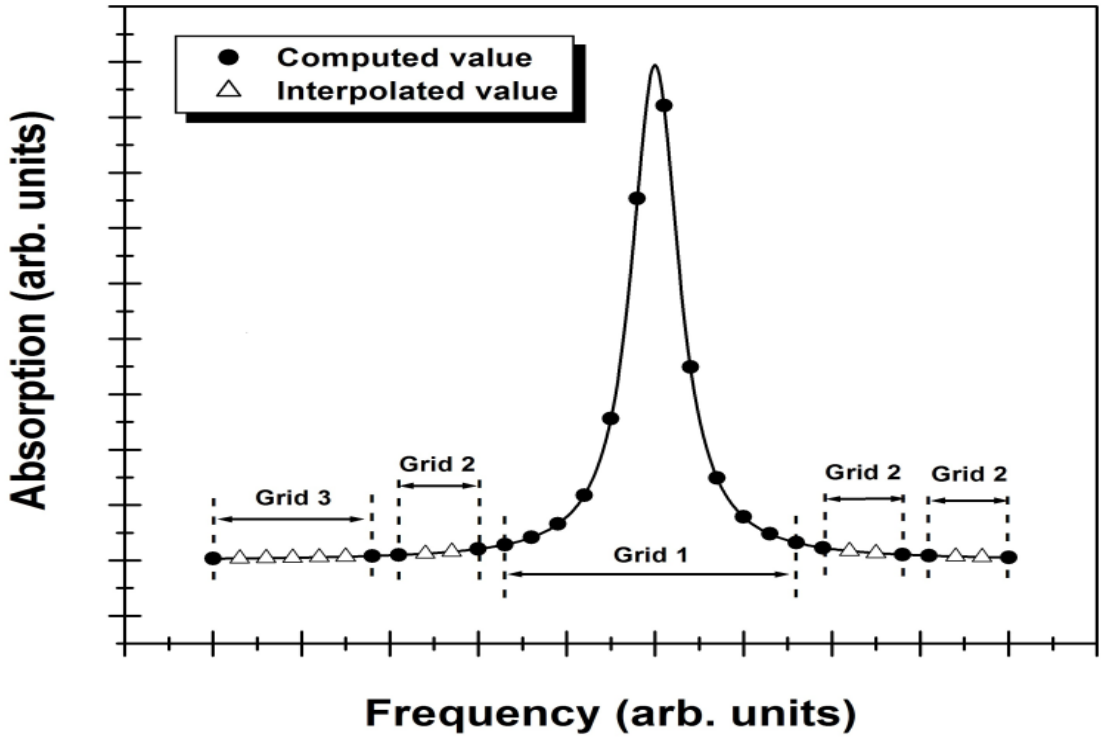

Fig. 2.9. Computation points near center line.

The approach employs a binary division of the spectral range, and calculations are performed on a cascaded series of wavelength grids, each with approximately twice the spectral resolution of the previous one. The GENSPECT error tolerances are 0.01%, 0.1%, and 1%, which may be selected according to the application [Quine, B. M. et al., 2002]. GENSPECT has been used to compute synthetic spectra for comparison with data collected by Earth observing instruments deployed in the air, in space and on the ground, including MOPITT-A, MOPITT, Atmospheric Chemistry Experiments- Fourier Transform Spectrometer (ACE-FTS), and MAESTRO. [Quine B.M., et al., 2007; Jounot, L. J., et al., 2002; McKernan, E. et al., 2002; Drummond et al., 2002; Dufour, D. G., et al., 2006; Dufour, D. G., et al., 2005].

Radiative transfer simulations were also performed using the GENSPECT in order to model the NIR spectra measured by the Argus instrument. Figure 2.10 shows a typical absorption spectrum computed by GENSPECT.

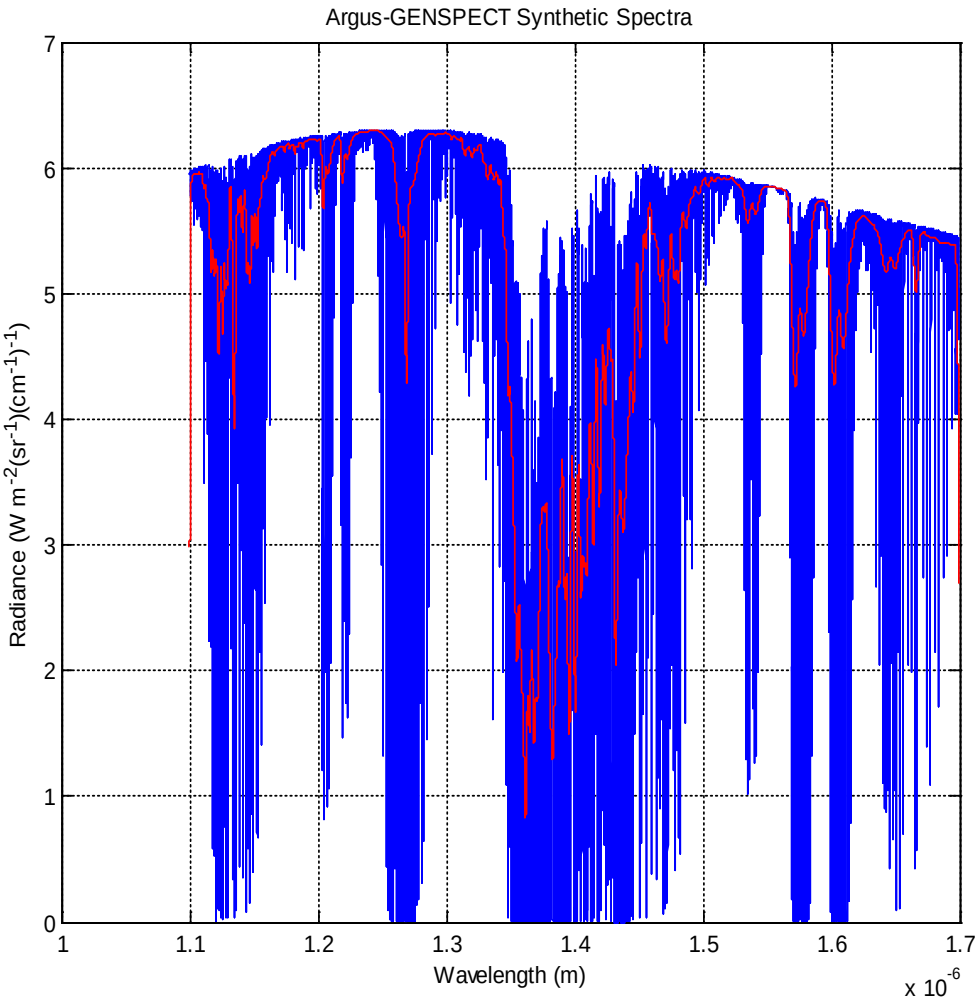

Fig. 2.10. GENSPECT simulated spectrum

The input parameters for the radiative transfer model are the solar zenith angle, Earth temperature, the mixing-ratio concentrations of O_2, H_2O, CO_2, CH_4 and the surface albedos. The code then produces a high-resolution spectrum, from which one can calculate radiance enhancement and upwelling radiative flux within selected wavelength bands. The

spectrum is in reasonable agreement with observed Argus absorption features of O_2, H_2O, CO_2 and CH_4 within the NIR wavelength bands of interest.

2.8 Shortwave and Longwave Radiative Flux

Clouds are an important of factor in Earth's radiation budget (ERB) and have a great impact on shortwave (SW) and longwave (LW) radiative flux. Clouds normally reflect solar or SW radiation back to space (upwelling flux) while restricting the escape of thermal or LW radiation to space as shown in Figure 2.11. The overall radiation budget due to clouds is often defined as the net energy between SW and LW fluxes measured at the TOA [Wielicki, B.A., et al., 2002]. One convention used to measure of this type of radiative effect is called cloud radiative forcing (CRF), which is defined as the difference in radiative fluxes at the tropopause in the presence of a cloud relative to a clear sky situation, in accordance with [Boucher, O., et al., 1998; Chen T., et al., 2000; Solomon, S. ed., 2007].

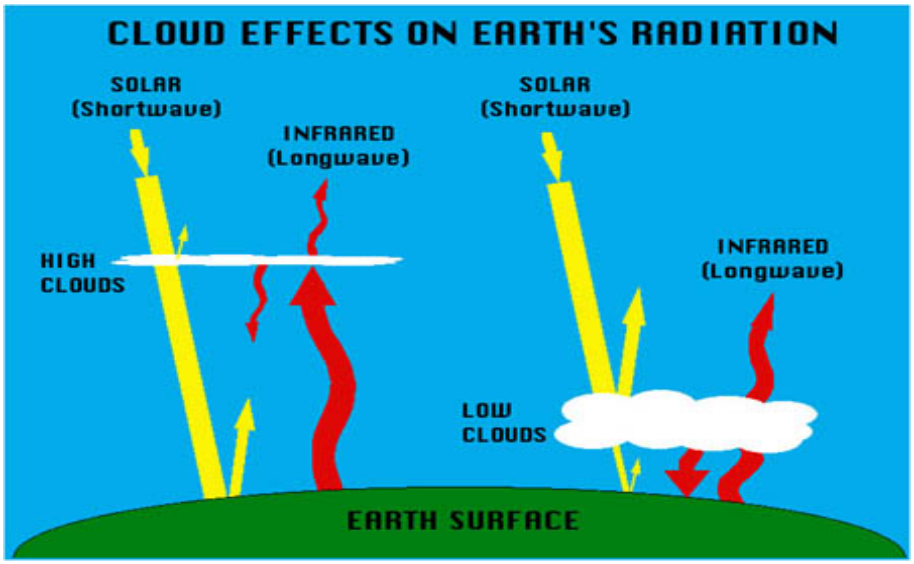

Fig. 2.11. Effect of clouds on distribution of shortwave and longwave radiation [Source: NASA].

A global mean average 342 W /m^2 of solar energy enters the TOA, and 107 W /m^2 of this energy is reflected back to space by the atmosphere, including clouds, suspensions of tiny airborne particles known as aerosols, and atmospheric gases. A small portion of solar energy, around 67 W /m^2, is absorbed by the atmosphere and is radiated back to space as LW radiation. The remaining energy that is directed downwards towards the Earth's surface is known as the down-welling SW radiation. Of the 198 W /m^2 of solar energy that reaches the Earth's surface, 168 W /m^2 is absorbed by the surface while about 30 W /m^2 is reflected back to space [Nankervis, C.J., 2013]. The current work only considers the SW-NIR wavelength region for cloud detection, utilizing the total shortwave upwelling radiative flux (SWupRF) within the 1100 to 1700 nm band [Siddiqui R. et al. 2016]. Individual upwelling cloud radiative effects have not been discussed within this wavelength band, because different types of clouds have different radiative effects, it is difficult to determine the individual cloud effect or impact of cloud changes on global climate system within this small SW range.

3.0 THE ARGUS SPECTROMETER

3.1 Argus 1000 Background

The Argus 1000 (Figure 3.1) is mini-spectrometer designed for space based measurements of near-infrared upwelling radiation reflected or emitted to space by Earth's surface and atmosphere [Quine B.M., 2010; Jagpal, R. K., et al., 2010; Siddiqui R. et al. 2016]. Launched in 2008, it was developed at York University, Canada in association with Thoth Technology Inc., and is a part of the Canadian Advanced Nano space eXperiment 2 (CanX-2) satellite payload [Sarda K. et al., 2006].

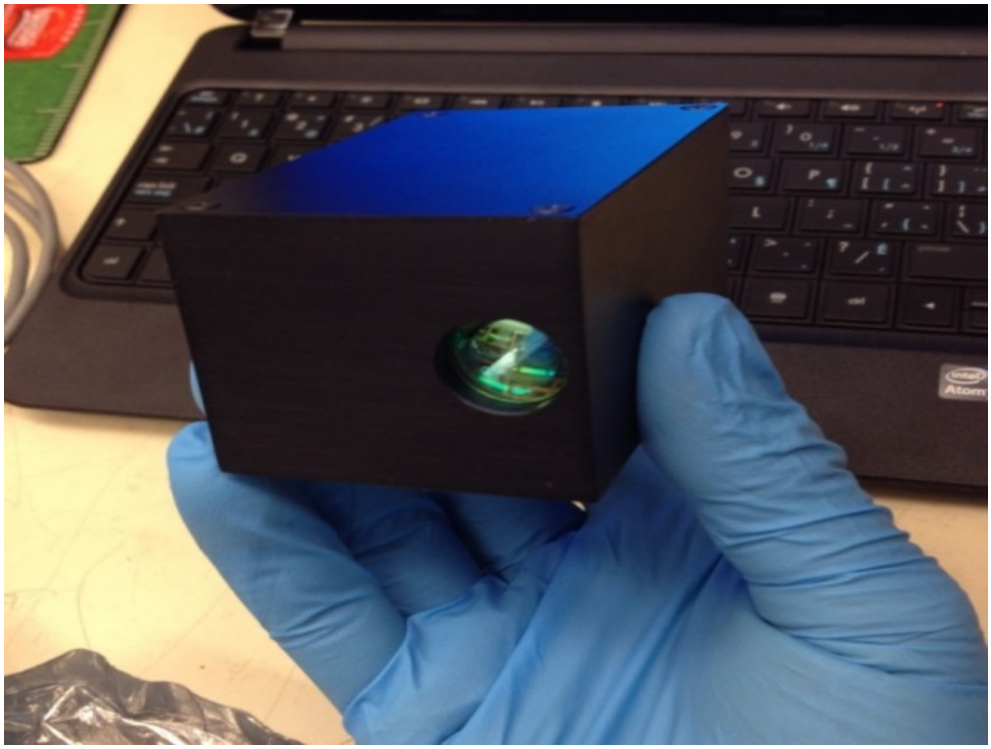

Fig. 3.1. Argus 1000 spectrometer at the Earth and Space Science and Engineering Laboratory, York University [Siddiqui R. et al. 2016].

The Argus spectrometer operates in the 900 to 1700 nm wavelength range and is mainly intended for use a space-based pollution monitor, and to measure concentrations of different greenhouse gases [Jagpal R.K., 2010]. CanX-2 sits in low Earth orbit (LEO) 640 km above the Earth's surface, where Argus' 0.15^0 field of view (FOV) yields a spatial resolution of 1.4 km [Quine B. M., 2010, user manual; Jagpal, R. K. et al., 2010]. Table 3.1 lists some Argus' technical specifications.

Table 3.1. Technical specifications, Argus 1000 Spectrometer (Owner's Manual, Thoth Technology Inc.)

Argus 1000	**Specification**
Type	Grating spectrometer
Configuration	Single aperture spectrometer
Field of View	0.15º viewing angle around centered camera bore sight with 15mm fore-optics
Mass	>230 g
Detector	256 element InGaAs diode arrays with Peltier cooler (100 active channels)
Grating	300 g/mm
Operational Modes	–Continuous cycle, constant integration time with co-adding feature –Adaptive Exposure mode
Spectral Channels	100 (typical)
Integration Time	500 µs to 4.096 sec

Figure 3.2 shows a front view of CanX-2 configuration during the assembly process. The Argus 1000 micro-spectrometer operates in the near infrared (NIR) band from 900 to 1700 nm, with spectral resolution of about 4-6 nm [Jagpal R. K. et al., 2010]. The

space-based instrument records IR spectra of solar radiation reflected lection from Earth's surface, using a linear photodiode array that records the incident radiant energy [Jagpal, R. K., 2011]. These spectra contain significant absorption features (associated with molecular absorption by particular gas species), that can be used to predict the atmospheric composition above a particular area of the planet [Quine B. M. et al., 2002; Jagpal R. K., 2011].

Fig. 3.2. The front-end view of Argus 1000 engineering model mounted on the CanX-2 nano-satellite [Source UTIAS].

The Argus spectrometer records the NIR signature of the at the top of the troposphere to measure the atmospheric concentrations of various molecular species. These include significant greenhouse gases such as oxygen (O_2), carbon dioxide (CO_2), water vapor (H_2O) and methane (CH_4), and carbon monoxide (CO). The NIR spectra can also be

used to monitor and identify sources and sinks of pollutants in the atmosphere. Finally, Argus data can be employed to detect the presence of cloud scenes [Siddiqui R., et al., 2015; Quine B. M. et al., 2002]. The measured spectra can be compared with theoretical IR absorption signatures, obtained by linear path forward modeling of absorption processes, to determine the various concentrations of absorbing species, and also to obtain the total upwelling radiative flux [Siddiqui R., et al., 2016]. In the absence of saturation or scattering effects, the amount of absorption depends upon the density of the absorber gas along the path. Therefore, the primary measurement objective of the instrument is to observe any changes in optical depth associated with the variation of the various atmospheric gas species in the spectral interval 900-1700 nm (11,111-5,882 cm^{-1}).

Table 3.2 shows the typical absorption characteristics of various gases in this spectral range and their typical absorption strengths [Jagpal R. K., 2011].

Table 3.2. Species observed by Argus

Observed Target Gas	Absorption wavelength (nm)	Comments
Oxygen (O_2)	1260	Very strong absorption due to O_2 abundance
Water (H_2O)	900 1200 1400	Dominant IR absorber 900-1700 nm
Carbon Dioxide (CO_2)	1240 1420 1570 1600	1600 nm features are well isolated
Methane (CH_4)	1660	Low abundance in this spectral band

The instrument is designed to take nadir observations of reflected solar radiation from Earth's surface and atmosphere [Jagpal R. K., 2011] as the satellite's flight path passes over a target geographical region. The Argus team at the Space Engineering Laboratory at York University prepares the observation tables for the desired targets around the globe using the Systems Tool Kits (STK) software.

The nadir-viewing geometry is especially useful for observations of regions that are partially cloudy or have surface topography of practical interest [Tsouvaltsidis C. et al., 2015; Alsalem N.Z.M., 2016], providing high spatial resolution over bright land surfaces and returning more useable soundings in areas that are partially cloudy or have significant surface topography. The availability of large sets of recorded data, with broad spectral coverage within the H_2O band, and high spectral resolution, also makes Argus an efficient tool for characterizing cloud scenes [Siddiqui R. et al. 2015]. In this work cloud detection is performed by the Argus spectral data set over various locations with the correlations of water vapors concentration and surface albedo.

3.1.1 Instrument design

The Argus 1000 micro-spectrometer has a mass of approximately 230g, and is designed to make nadir-view observations of different surface. The instrument on CanX-2 scans the Earth with an instantaneous surface resolution of approximately 1.4 km, with a ground speed of 7.5 km/s as the spacecraft orbits around the Earth. Argus 1000 has an instantaneous field of view (IFOV) of 2.18 mRad as shown in Figure 3.3 [Siddiqui R. et al. 2017].

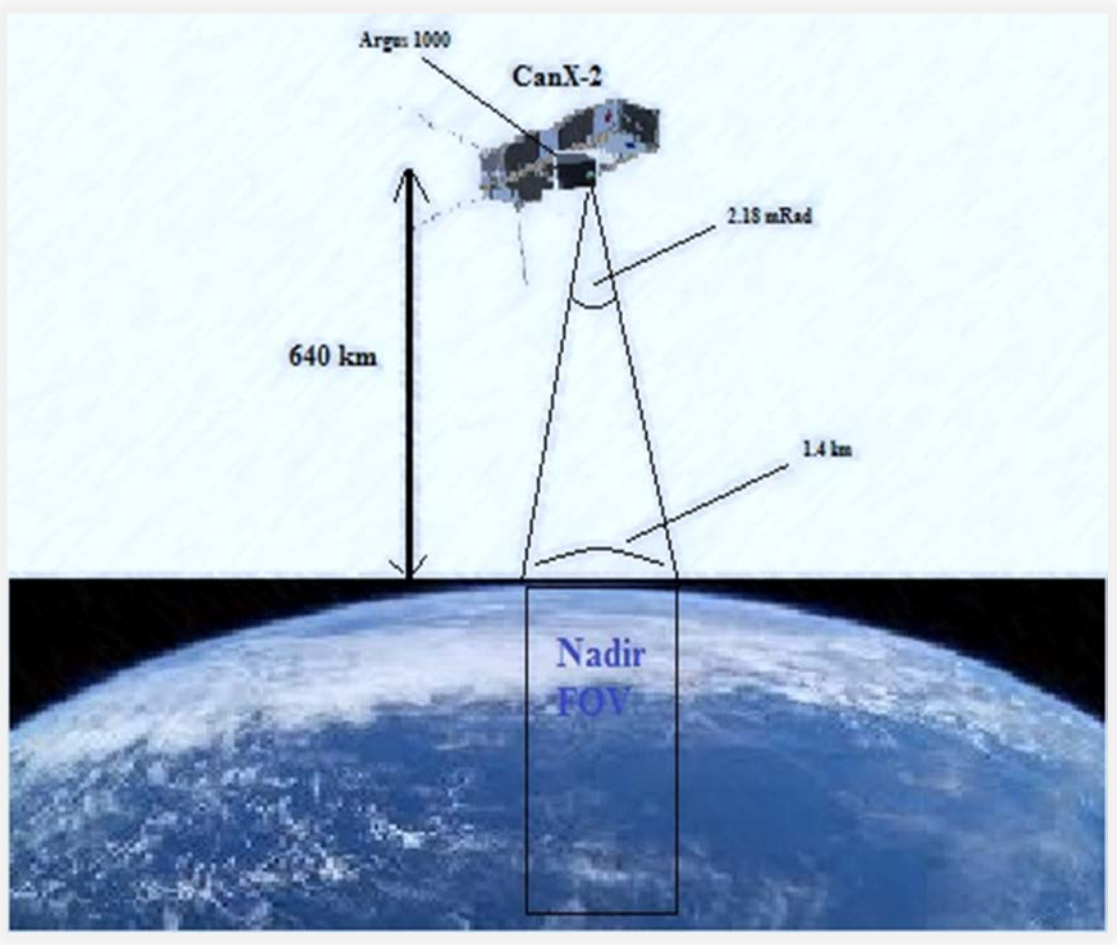

Fig. 3.3. Argus 1000 field of view (FOV)

Argus provides a high-resolution mapping capability for the detection of greenhouse gas absorption features, as shown in Figure 3.4. These characteristics enable the precise identification of atmospheric constituents, and identification of local variations of cloud cover by means of measured reflection of solar radiation. The same kind of Argus spectrometer was launched for technology demonstration mission and Earth's observation by Satish Dhawan Space Centre (SDSC) in 2011 and by Sathyabama University in 2016 on board SRMSAT-1 nanosatellite [SRMSat: satellite mission] and SathyamabaSat [SB Sat mission] respectively.

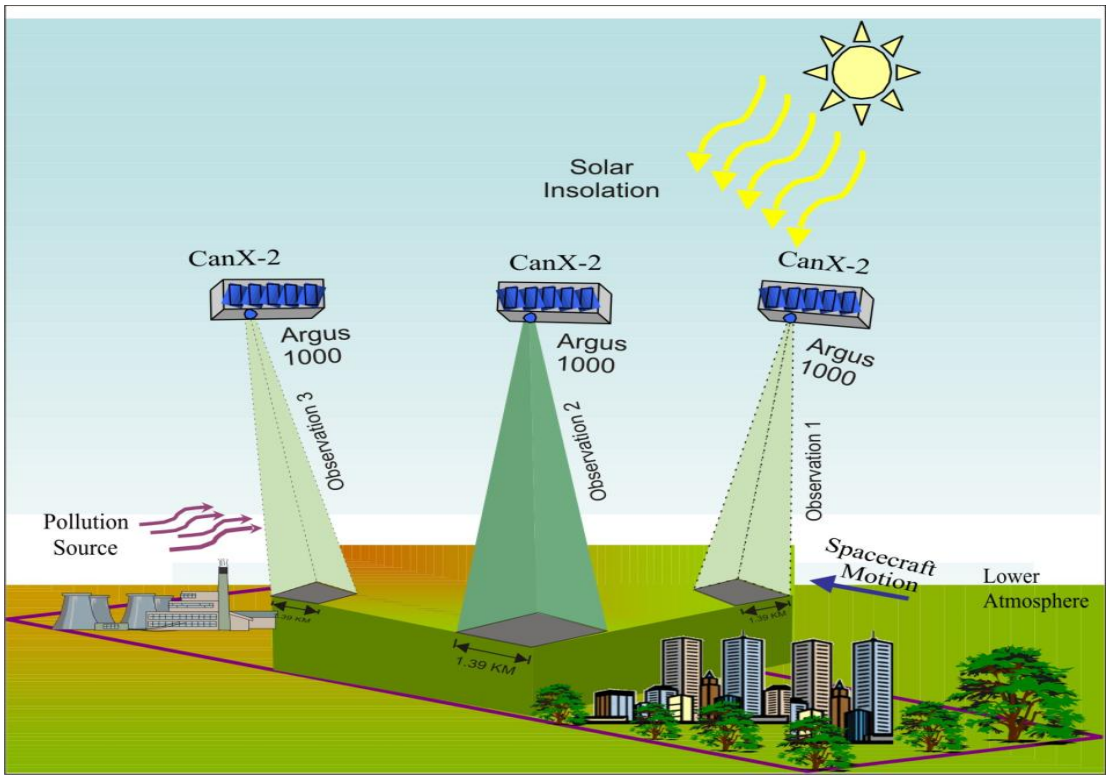

Fig. 3.4. Nadir viewing geometry of Argus 1000 spectrometer. [credit: Jagpal R.K., 2011]

Argus features an actively-cooled detector array of 1×256 elements. Each pixel has a radiometric resolution of 12 bits, with an exposure time ranging from microseconds to seconds for data recording. The instrument functions as a quantum detector, directly measuring spectrally-filtered incident radiation, and converting photonic flux into electrical charge in a high-efficiency process that conserves energy and provide measurements of absolute radiance [Jagpal R.K., 2011].

3.1.2 The CanX-2 satellite

The Canadian Advanced Nano space eXperiment 2 (CanX-2) satellite that carries Argus was launched on April 28, 2008, aboard the Indian Polar Satellite Launch Vehicle (PSLV) (Figure. 3.5), from Satish Dhawan Space Centre (SDSC), Sriharikota, India. It

occupies a Sun-synchronous, near-polar, low Earth orbit (LEO). The Canadian Advanced Nano space eXperiment (CanX) are a series of satellites that were launched by the University of Toronto Institute for Aerospace Studies/ Space Flight Laboratory (UTIAS/SFL) in September 2001 [Rankin D., et al., 2005] as part of a technology demonstration mission.

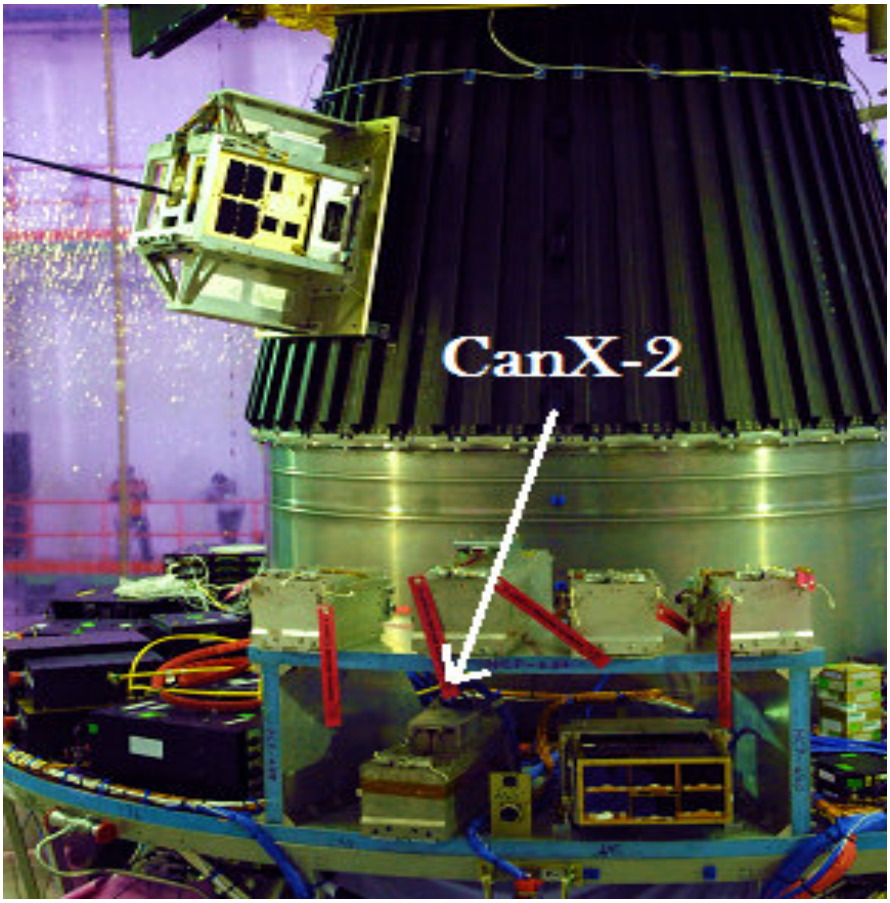

Fig. 3.5. PSLV-C9 upper stage and the position of CanX-2 [Courtesy: ISRO]

The CanX-2 program was developed to provide Canada with a continuous supply of highly-skilled and experienced space- system and microsatellite engineers, while at the same time offering a low-cost, quick-to-launch satellite platform for executing scientific and technology demonstration missions [Sarda K., et al., 2006]. After its successful

launch, both CanX-2 and Argus 1000 were commissioned, and the first full operation began in March 2009. The first set of scientific data was downloaded during the commissioning phase, on September 23, 2008 [Jagpal R.K., 2011].

3.2 Observational Data Format

The Argus instrument collects data for a four-week long period as it passes over its determined targets, and then stops for two-month break, allowing the two other experiments aboard CanX-2 to function. The Argus-1000 target list comprises 35 sites around the Earth. Some of the targets corresponding to very recent dataset profiles along with their respective locations [Jagpal R.K., 2011; Siddiqui R. et al., 2015] are shown in the world map of Fig. 3.6.

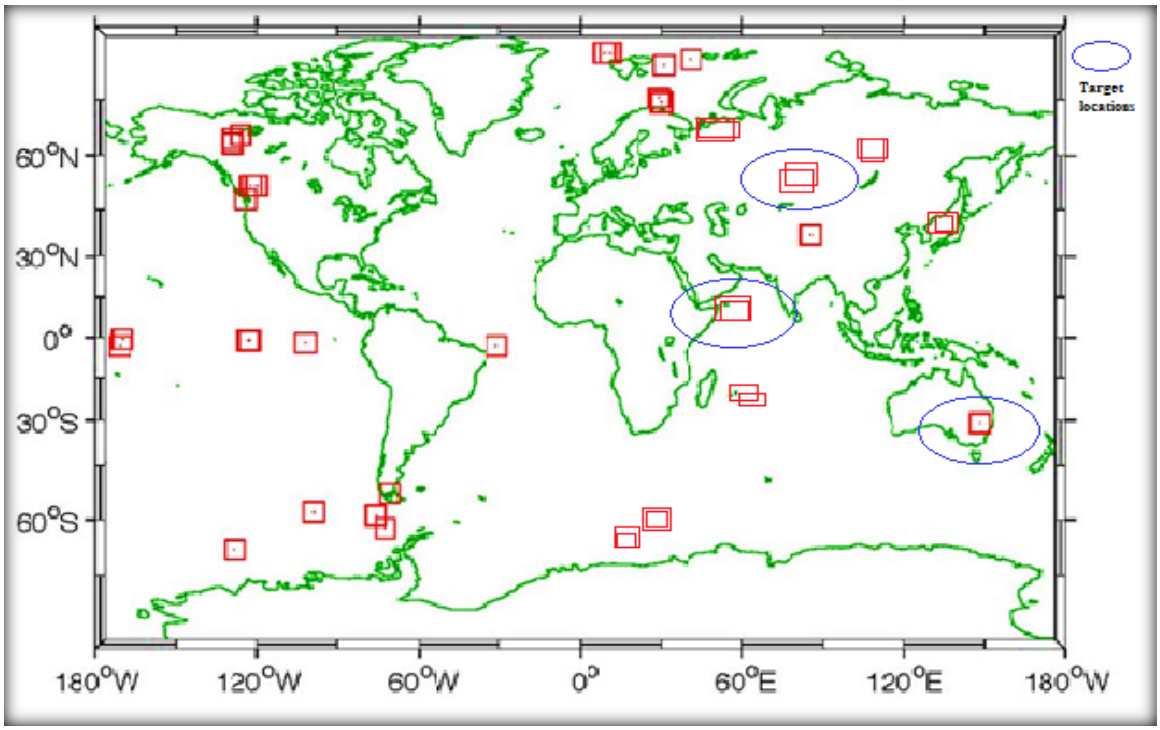

Fig. 3.6. Argus measurement locations (modified version) for approximately 300 recorded profiles (red: Argus locations; blue: target locations for cloud scenes.

In the nine years that Argus has been in operation, over 300 datasets have been obtained [Siddiqui R et al., 2015] over a series of land and ocean targets. A dataset is labeled by the operational week and pass, which corresponds to a continuous trajectory of the satellite over a target region. For each pass, a series of consecutive NIR spectra are captured and recorded, numbering from about fifty to over two hundred. Each of these is termed an "observation", and a subset of these observations carries useful data. A few examples of the retrieved datasets are as shown in Table 3.3 Each dataset consists of three parts: (i) a record of various instrument parameters (exposure time, sensitivity, temperature, etc.) that were applied during the observation period, (ii) the raw spectral data collected over the selected target, and (iii) the parameters defining the satellite's attitude and orientation as is passed over the target region.

Table 3.3. Typical Argus dataset with observations range and length of each week per pass

Week No. /Pass No.	File Name *. CX@MEM	Date	Observation Numbers	Total Observations
Week02_Pass94	144207_ 20100000_ 98028	2009March10	25-162	162
Week03_Pass05	150049_ 20100000_ 93240	2009March11	38-174	174
Week03_Pass20	034752 _20100000_ 48636	2009March13	38- 91	91
Week08_Pass61	134216_ 20100000_ 150696	2009October30	35-275	282
Week14_Pass10	013903_ 20100000_ 67788	2010March02	14-125	125
Week14_Pass52	171624_20100000_67284	2010March04	14-125	125
Week17_Pass42	015938_20120000_77868	2010April29	14-144	144
Week75_Pass43	022523_20100000_35784	2013August14	12-65	65

For every week of the observation campaign, the STK package is used to chart the paths of the CanX-2 satellite over the selected targets, providing a list of start and stop times and the duration time in seconds for each pass. Table 3.4 shows a typical observation table generated by STK for the case of cloud detection. The generated Argus target lists are sent to the operations unit at UTIAS at the start of every observation week, who then return the collected weekly data to the Argus team at York University for processing and analysis.

Table 3.4. List of the selected weeks per passes with target, start and stop time of Argus flight

Week per pass	Target	Start Time (UTCG)	Stop Time(UTCG)	Duration (sec)
Week08 Pass61	Arabian Sea, Indian	2009/Oct/30 05:46:18.18	2009/Oct/30 05:51:48.48	329.77
Week14_Pass52	Toronto, Canada	2010/Mar/04 15:40:13.13	2010/Mar/04 15:42:34.34	140.18
Week75_Pass43	Pacific Ocean, Australia	2013/Aug/14 22:08:57.57	2013/Aug/14 22:13:41.41	283.87

The different types of the data files provided by UTIAS are shown in Figure 3.7. The Argus raw data file consists of a series of spectral observations. The maximum amount of data that can be stored aboard the CanX-2 satellite is 500 KB per day (after data compression), which corresponds to approximately 6 minutes of Argus instrument operation times [Quine B.M., 2010, user manual; Jagpal R.K., 2011]. The spectra are obtained using exposure times of around 102.4 ms to 204.8ms. A few datasets used longer integration times to study certain strongly absorbing features, at the expense of saturation in the CO_2 and H_2O wavelength bands.

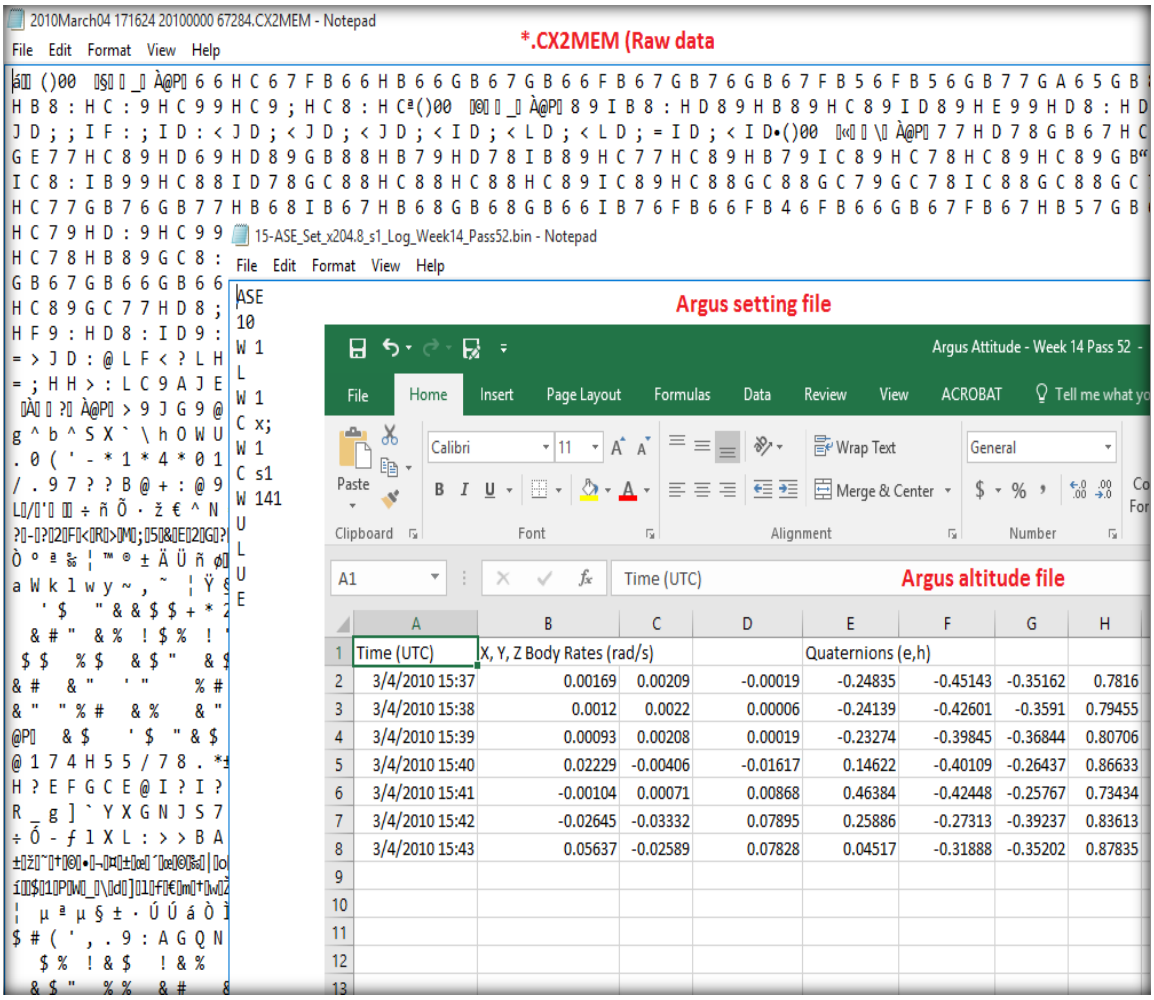

Fig. 3.7. Data files provided by UTIAS for week 14 pass 52 during Argus observational campaign.

3.3 Geolocation of Argus Spectral Observations

The CanX satellite's position and altitude measurements are used for the geolocation of Argus remote sensing observations. Since the launch of the CanX-2 satellite [Jagpal R.K., 2011; Chesser H., et al. 2012], Argus has been in operating mode, transmitting data sets starting from February 2009. In the commissioning phase of the instrument, the first data was downloaded by Argus science team at York University in collaboration with space craft operators at the University of Toronto's Institute of

Aerospace Studies Space Flight Laboratory (UTIAS-SFL). The geolocation software is based on the NORAD two-line element (TLE) set that consists of 69 orbital characteristics [Jagpal R.K., 2011]. Argus datasets consist of a series of periodic measurements which are referred as granules [Chesser H., et al. 2012], currently designated using Argus week per pass per observation numbers [Siddiqui R et al., 2015]. The Argus science team has retrieved more than 300 data sets, with each week/pass of Argus flight data representing a duration of about 5-15 minutes. The coordinates of the CanX-2 satellite are analyzed by using three different frames of references: the Earth-centered inertial (ECI) frame, the Earth-centered Earth-fixed (ECEF) frame and the spacecraft body (SCB) frame [Jagpal R.K., 2011]. The NORAD TLE details can be obtained from the Space Track website, and the satellite's position can be determined by applying the Simplified General Perturbation Mode 4 (SPG4) orbital prediction algorithm [Jagpal R.K., 2011; Chesser H., et al. 2012; Siddiqui R. et al., 2015]. In order to minimize propagation error, the closest NORAD TLE is chosen for the particular Argus week/pass/observations [Siddiqui R. et al., 2015], and satellite altitude information can be obtained at one-minute time intervals over the period of the requested data set.

4.0 RADIANCE ENHANCEMENT TECHNIQUE FOR CLOUD DETECTION (PROPOSED METHODOLOGY)

4.1 Radiance Enhancement (RE) by Space-Orbiting Argus 1000

We used the method of radiance enhancements retrievals by means of a forward model to output simulated radiance profiles [Siddiqui R. et al., 2015]. GENSPECT introduced an updated retrieval algorithm for the space instrument described by [Quine B. M. et al., 2002; Chesser, H. et al., 2012], based on detailed forward modeling of the atmosphere and instrument claimed by [Abrarov S. M. et al., 2009]. Given atmospheric temperature and pressure information, expected trace gas abundances, and some instrument calibration parameters, our model simulates the spectral scans recorded by the instrument during flight. An optimization routine is used to obtain a best fit between the simulated and measured spectra by adjusting the instrument parameters and trace gas amounts [Toohey, M., et al., 2007; Toohey, M., 2009; Jagpal R.K., 2011]. The main advantage of this technique is the incorporation of instrument parameters into the retrieved state vector, which allows the analysis of flight data with the calibrated data.

4.1.1 Methodology

Efficient detection of cloud and their surface features means detecting and recording of enhancement of radiant light energy by cloud surfaces. In this study, the detection of clouds is implemented by finding the maximum or minimum RE_i and their

combined radiance enhancement (CRE(i)) effects by using Eq. (4.1) to Eq. (4.4), within selected NIR wavelength bands of O_2, H_2O, CO_2 and CH_4 [Siddiqui, R., et al., 2015]. The RE method is mainly based on the mean value of the ratio of the difference of the observed data with simulated data for the selected week per pass with single observation or multiple observations of the Argus wavelength bands. The RE algorithm has been developed by using the Sun elevation angle, satellite nadir angle, variable path length, atmospheric water vapor and different albedo [Siddiqui R. et al., 2015].

$$RE_i = \frac{1}{N} \sum_{j=1}^{N} \left\{ \frac{OBS_i[j] - SYN_j\,[j]}{SYN_j} \right\} \tag{4.1}$$

where

RE_i = Radiance Enhancement for all wavelength bands for i = 1 to 4.

OBS_i[j] = Observed (real) data.

SYN_i[j] = Synthetic (GENSPECT-simulated) data.

$$CRE(1) = \frac{RE(2)}{RE(1)+RE(4)} \tag{4.2}$$

$$CRE(2) = \frac{RE(1)}{RE(2)+RE(3)} \tag{4.3}$$

$$CRE(3) = RE(1) + RE(2) + RE(4) \tag{4.4}$$

CRE(i) = Combined Radiance Enhancement (i =1 to 4)

RE(1) = Radiance Enhancement in the H_2O & O_2 bands of interest

RE(2) = Radiance Enhancement in the H_2O & CO_2 band of interest

RE(3) = Radiance Enhancement in the CO_2 band of interest

RE(4) = Radiance Enhancement in the CH_4 band of interest.

Each CRE result measures combined effect of enhancement within the selected wavelength band of interest. The Eq. (4.2) calculates the CRE within O_2 (RE1), H_2O(RE2), and CH_4 (RE4) which gives high enhancement when the combined radiance of RE1 and RE4 is high as compared to the total enhancement within RE2. The Eq. (4.3) also calculates the CRE within O_2 (RE1), H_2O (RE2), and CO_2 (RE3) which gives high enhancement when the combined radiance of RE2 and RE3 is high as compared to the total enhancement within RE1. The Eq. (4.4) calculates the total radiance enhancement within O_2, H_2O and CH_4 wavelength bands. All three relationships of CRE are applied for the classification of clouds.

Cloud detection techniques are generally based on the assumption that clouds present some useful features for their identification. Clouds are usually brighter and colder than the underlying surface; clouds increase the spatial variability of detected radiance, and the spectral response is different from that of the surface cover clearly described by [Coakley Jr J.A. et al., 1982]. Table 4.1 shows the input parameters used for the efficient detection of cloud scenes described above.

Table 4.1. Input parameters used for RE model.

Types of parameter	Significance values and ranges
Mixing Ratios of gases	refmod 95_ O_2.mxr, refmod 95_ CO_2.mxr, refmod 95_ CH_4.mxr, refmod 95_ H_2O.mxr [1976 U.S. Standard Atmospheric Model]
Gases in %	O_2 (0-100), CO_2 (1-200), CH_4 (1-100), H_2O (1 to 100)
Cloud height from surface to top of clouds	2 km to 50 km (cloud altitude from 2 to 10 km, above the Erath surface)
Surface Type	Lambertian
Database type	HITRAN
Satellite Sun angle*	Argus geo location (average of observation .)
Satellite nadir angle*	Argus geo location (average. of observation.)
Albedo (surface reflectance)	0.01 to 0.3 (over oceans) 0.3 (over land, generic vegetation and bare soil) 0.1 to 0.9 (over snow, clouds and ice)
Scattering Type	Rayleigh

*Satellite viewing angle: Nadir

The RE technique for the efficient detection of cloud scenes is mainly divided into four major steps as shown in Figures 4.1 and 4.2. The first step is to specify atmospheric mixing ratios, water vapor concentration, and reflectivity, and to compute absorption coefficients for all the gases at all spectral points and heights using the combined MATLAB script atmospheric_synthetic_spectra_H2O.m, which combines the Argus atmospheric model computation and the synthetic spectrum generation model. After successful running of this code, the absorption coefficients of all the gases in the synthetic atmosphere are obtained. The second step is to run the observed_spectra_radiance.m module, which reads the raw Argus data, calibration, and background files. After execution of this code, we generate all the spectra of counts as a function of wavelength and radiance for the full range of observation numbers of all week per pass data as shown in Figure 4.1.

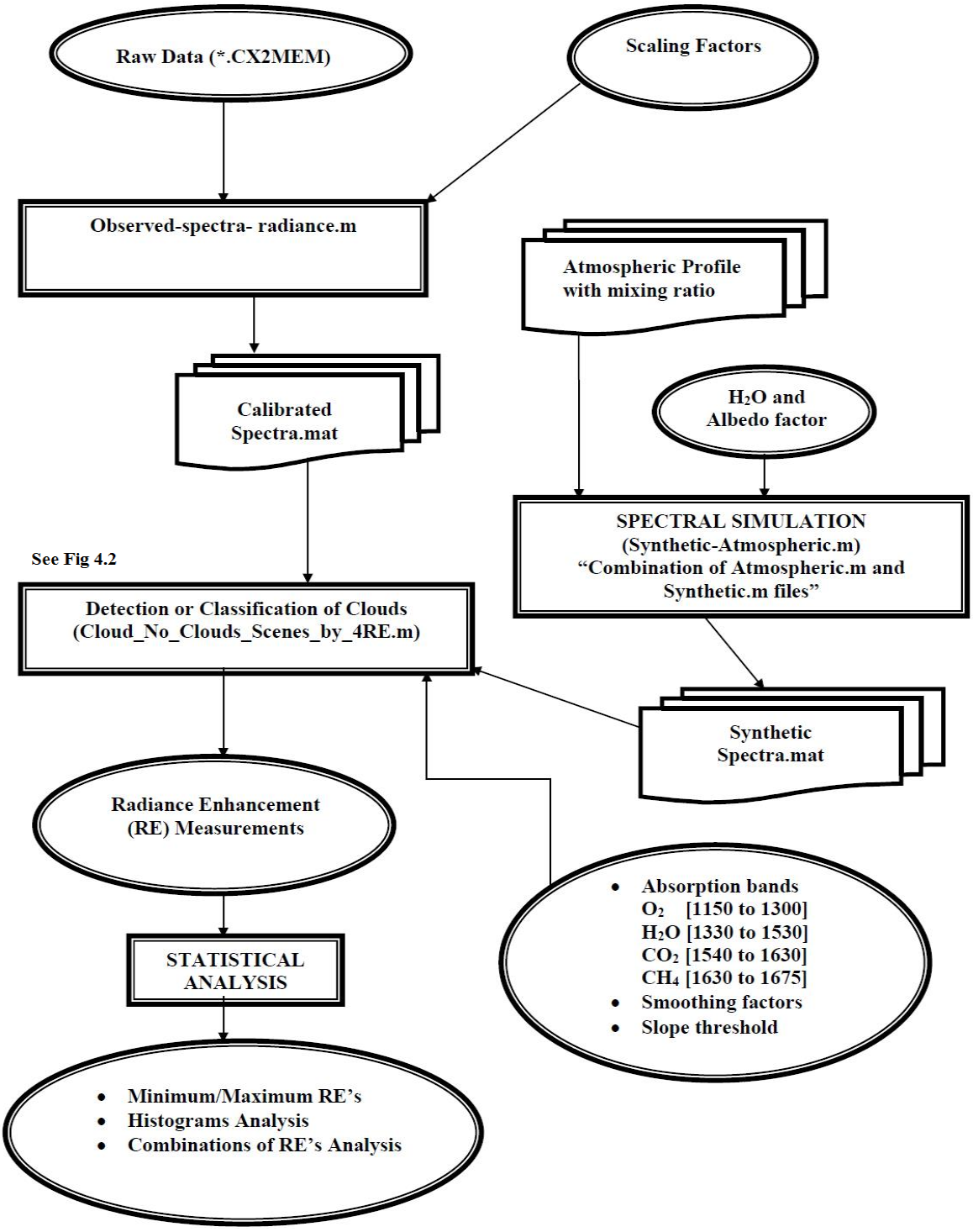

Fig. 4.1. General layout classification of cloud scenes using the Argus 1000.

Some of the parameters (for example, albedo) need to be adjusted either manually or through optimization [Siddiqui R., et al. 2015]. The optimization is implemented through looping by consecutive increment or decrement of the corresponding parameters. The third step is to run the Clouds_NoClouds_Spectrums_by4RE.m module, which generates the mean value of the ratio of the difference of the observed data with simulated data for single or full range of Argus observations with each week per pass by using the GENSPECT LBL radiative transfer model. The selected wavelength and other parameters for the RE model are shown in Table 4.2.

Table 4.2. Wavelength and Smoothing Bands used for cloud classification for model.

Radiance Enhancement (RE)	**Name of Bands**	**Wavelength Bands range (nm)**	**Smoothening Bands**	**Slope Threshold***
RE1	H_2O and O_2 absorption band	[1150 to 1300]	O_2 synthetic, O_2 observed [50,50]	0.5e-6
RE2	H_2O and CO_2 absorption band	[1330 to 1530]	H_2O synthetic, H2O observed [50,50]	0
RE3	CO_2 absorption band	[1540 to 1630]	CO_2 synthetic, CO_2 observed [0,0]	0.
RE4	CH_4 absorption band	[1630 to 1675]	CH_4 synthetic, CH_4 observed [0,0]	0

*Plateau detection threshold for the O_2 band (its variable height and % position require us to detect the sub-band where it is most “flat”).

The current version of GENSPECT applies linear paths and photons that have experienced mainly single scattering. In most of the cases, the multiple scattering in the IR spectral region is not observed to be as significant as in the SW-NIR spectral region; this

complex process is often simplified, or neglected, in most IR remote sensing applications [Zhang, Z., et al., 2007]. The basic GENSPECT [Quine B. M. et al., 2002] modeling runs the following library function files: paths.m, path_source.m, path_atmosphere.m, path_reflect.m, atmospheric_cell.m, atmospheric_read.m, and cell_mixing_ratio.m. The paths.m function generates a viewing path through a set of gas cells using function cells. The path is a linear path through the set of gas cells (the order and cells used are determined by the start and stop altitudes) at a specified incidence angle. To generate the outputs, the function calls on the structure cells and returns structure paths containing all the required information for radiance calculations. The paths.m function defines a path segment corresponding to a reflecting surface in the reflectivity of the Earth's surface. The paths_radiance.m function calculates the radiance through a path. It uses library functions called path_gas.m, path_source.m, and path_reflects.m to form a path and generates the radiance after each path segment. The atmospheric cell generates a set of data that represent the atmosphere structure. Atmospheric cells are divided on the basis of height as pressure increments according to the choice of input division. The function then performs the Curtis-Godson approximation [Walshaw, C.D., et al., 1963] and finds mean pressure, temperature, and number density values for each cell. The atmospheric_read.m function reads and saves an atmospheric profile. The radiances obtained are given in the units [$(Wm^{-2}\ sr^{-1}\ (1/cm)^{-1}$]. The details of the selected week per pass of the Argus with the selected observation numbers are shown in Table 4.3.

Table 4.3. Argus selected week per pass per observations with geolocation.

Week No._Pass No.	Date	Selected Observation Numbers	Observation number with satellite Sun angle, Nadir angle, Latitude and Longitude.	Location
Week08_Pass61	2009October30	64,116,196,238 Total packet length (282)	OBS64: Sat. nadir angle = 5° 45' 28.44" Sat. Sun angle = 35° 18' 16.91" Lat. = 6° 30' 22.36" N Long. = 60° 57' 43.92" E OBS116: Sat. nadir angle = 6° 48' 40.32" Sat. Sun angle = 32° 21' 24.84" Lat. = 3° 12' 19.8" N Long. = 60° 7' 35.76" E OBS196: Sat. nadir angle = 3° 27' 29.15" Sat. Sun angle = 29° 16' 22.08" Lat. = 1° 31' 35.4" S Long. = 59° 14' 52.44" E OBS238: Sat. nadir angle = 3° 36' 23.75" Sat. Sun angle = 29° 8' 42.35" Lat. = 4° 16' 5.16" S Long. = 58° 44' 51.36" E	Arabian Sea & Seychelles
Week14_Pass52	2010March04	22,100,120,124 Total packet length (125)	OBS22: Sat. nadir angle = 24° 42' 54.71" Sat. Sun angle = 58° 6' 48.95" Lat. = 47° 22' 26.4" N Long. = 77° 43' 42.96" W OBS100: Sat nadir angle = 23° 52' 33.6" Sat. Sun angle = 54° 54' 39.23" Lat. = 42° 50' 28.68" N Long. = 79° 43' 8.04" W OBS120: Sat nadir angle = 23° 52' 33.65" Sat. Sun angle = 54° 54' 39.31" Lat. = 42° 50' 28.79" N Long. = 79° 43' 8.13" W OBS124: Sat nadir angle = 21° 52' 39.72" Sat. Sun angle = 54° 32' 36.23" Lat. = 42° 17' 21.48" N Long. = 79° 56' 43.08" W	Toronto/ Kitcisakik (Canada)
Week75_Pass43	2013August14	19,30,43,65 Total packet length (65)	OBS19: Sat. nadir angle = 1° 53' 19.53" Sat. Sun angle = 38° 40' 51.12" Lat. = 31° 45' 33.12" N Long. = 148° 12' 48.6" E OBS30: Sat. nadir angle = 1° 44' 51.72" Sat. Sun angle = 38° 14' 43.08" Lat. = 28° 55' 23.88" N Long. = 147° 33' 54.72" E OBS43: Sat nadir angle = 1° 40' 8.04" Sat. Sun angle = 37° 58' 44.04" Lat. = 25° 34' 55.92" N Long. = 146° 48' 29.88" E OBS65: Sat nadir angle = 1° 41' 15.72" Sat. Sun angle = 38° 9' 54.71" Lat. = 19° 55' 28.56" N Long. = 145° 32' 53.16" E	North Pacific Ocean

The next and final step is to run the module Cloud_NoClouds_Data_by4RE.m, which calculates the RE tabulated mean values of the ratio of the difference of the Argus (observed) and GENSPECT (synthetic) spectrum data using Eq. (4.1) through Eq. (4.4) and generates a data file cloudvals.mat. The main methodology to calculate RE_i and CRE_i,is shown in Figure 4.2 [Siddiqui R., et al. 2015].

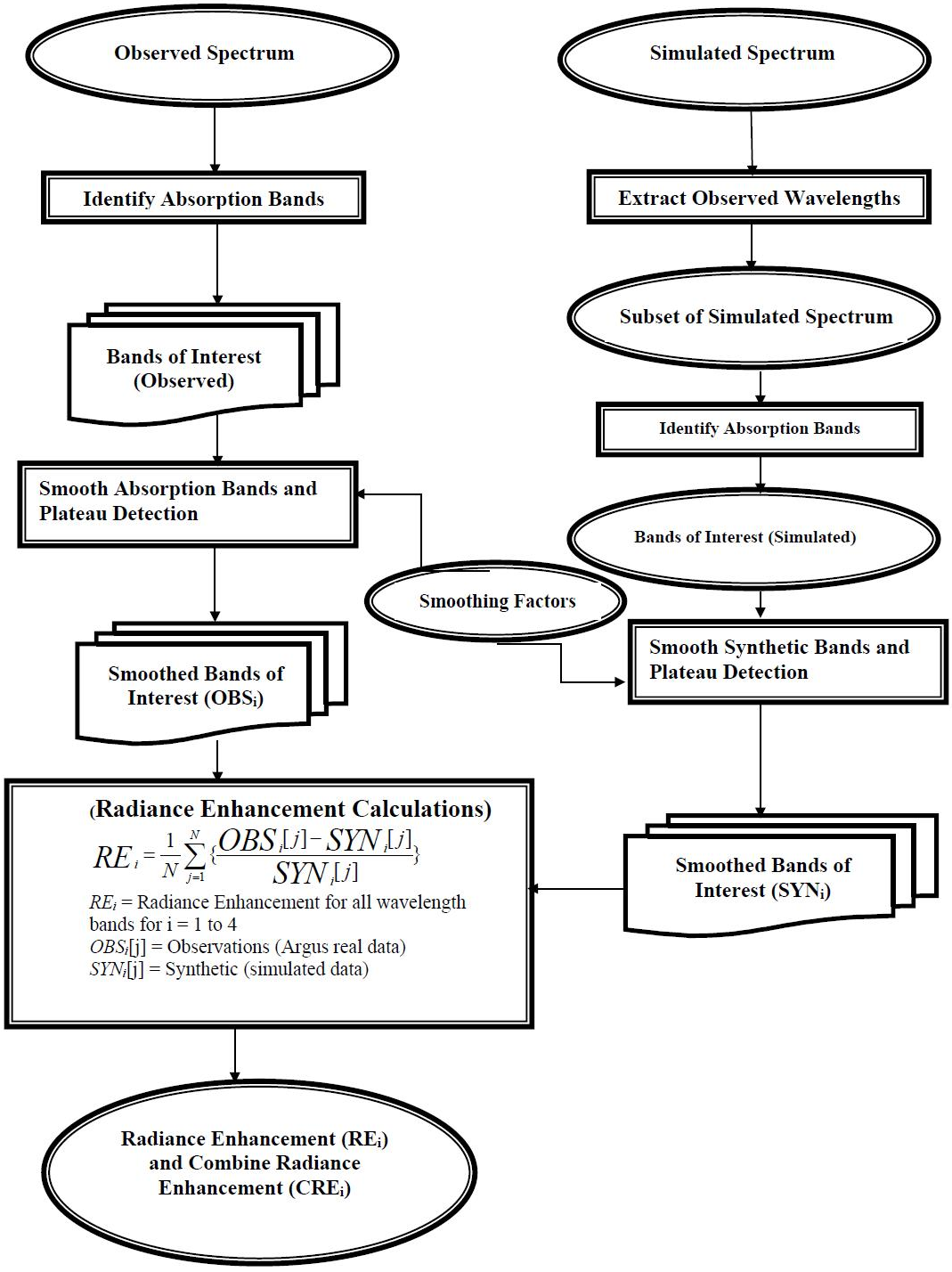

Fig. 4.2. Main technique used for the efficient detection of cloud scenes by the Argus 1000 along with the GENSPECT synthetic model.

4.1.2 RE-GENSPECT model on SHARCNET

The GENSPECT model with all its functions and data files is fully functional at SHARCNET. We have developed a script Synthetic_atmospheric.m, which combines the atmospheric and synthetic profile using the OCTAVE model. This script can easily run different jobs in series and parallel mode at the SHARCNET platform. Each single job can take 15 to 30 minutes to complete on either SAW or ORCA SHARCNET clusters. We submit the diverse types of synthetic jobs with different information's of input parameters both in series and parallel mode and take some time 4 to 5 hours, subject to the availability of the cluster on SHRCNET servers. The output of this SHARCNET version of the synthetic model is applied to the RE optimization for the detection of cloud scenes. More than 300 jobs on the SAW and ORCA clusters of SHARCNET have been successfully finished and used for the different types of comparisons with real Argus data.

4.1.2.1 Non-linear least squares technique for RE model

We developed a series of functions to optimize the GENSPECT-Synthetic output with the Argus observed dataset by using the joules-per-count with each pixel value so that the calibrated Argus spectrum matched a reference spectrum at a set of wavelength bands. The optimization technique is applied on different Argus real data set along with synthetic model. The overall model and optimization scheme at Sharcnet is shown in Figure 4.3 with these test functions: (i) calibfit.m, (ii) calibtest.m, (iii) lsqcal.m, and (iv) lsqtest.m.

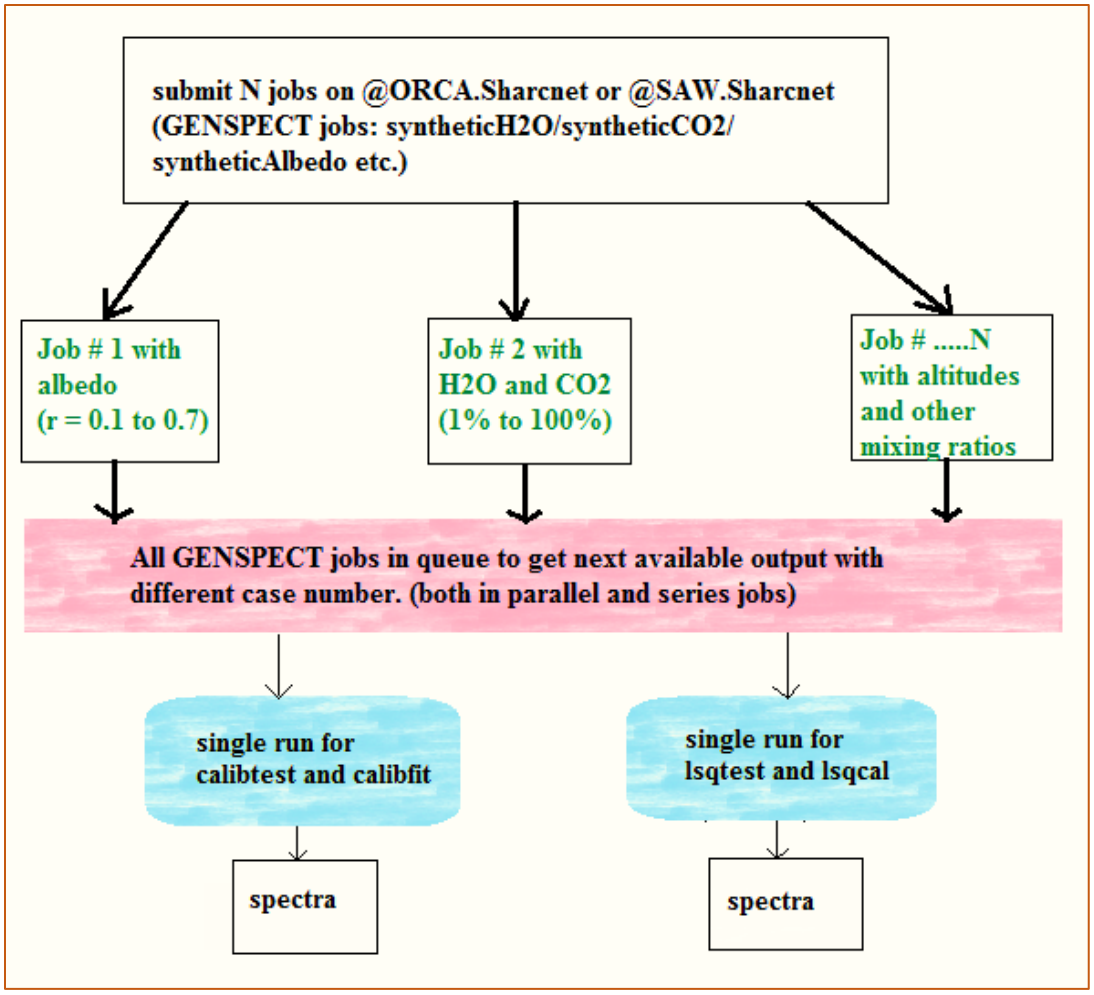

Fig. 4.3. General layout of GENSPECT-synthetic jobs on Sharcnet platform.

4.1.2.2 Calibfit (Argus spectral fitness function)

The function calibfit is used in conjunction with a nonlinear optimization algorithm such as lsqnonlin (x) and computes matching fitness values between a reference synthetic absorption spectrum and an observed spectrum, which is standardized according to a profile that is defined by the parameters to be optimized. The parameters in x are interpreted as Joules-per-count (JPC) values that define the calibration profile [Jagpal R., 2011].

4.1.2.2.1 Calibtest (Test script to read Argus data file)

The script calibtest reads the Argus data file and uses the calibration params (JPC) to generate spectral plots and save them to files.

4.1.2.3 Lsqcal (optimizes Argus data)

The script lsqcal optimizes the Argus data set by using the generated values of the synthetic model so that the calibrated Argus spectrum matches a reference spectrum at a set of wavelength bands.

4.1.2.3.1 Lsqtest (Test script for non-linear optimization):

The script lsqtest is a test script for nonlinear least-squares optimization of Argus spectra, based on fitness of match to a synthetic reference spectrum.

4.2 Model predictions (simulated radiance for cloud detection)

To interpret the total radiance [$(Wm^{-2}\ sr^{-1}\ (1/cm)^{-1}$] measured at the Argus detector for the detection of cloud and no-cloud scenes, different parameters including H_2O, CO_2, altitudes, and albedo must be estimated by using the synthetic model. The amount of smoothed reflected radiance is plotted as a function of wavelength, which provides a better visualization for the optimization technique. We set our model mixing ratio concentrations of O_2, H_2O, CO_2 and CH_4 to zero and run different simulations cases with r is equal to 0.3 and H2O is equal to 30% (not a case when we set H_2O is equal to zero), to check the absorption features validity of each selected gas within the wavelength band of interest.

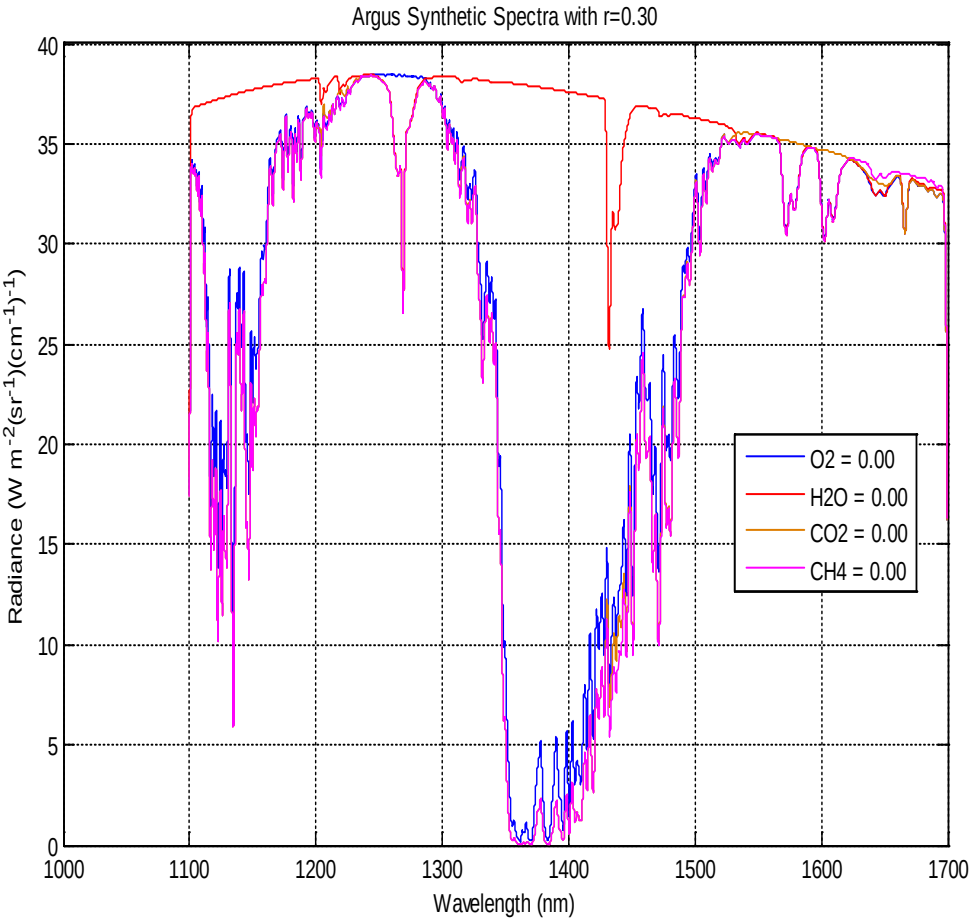

Fig. 4.4. Validity of absorption peaks of the selected gas within the wavelength band of interest when set to zero value. (Synthetic spectrums with r=0.3).

Figure 4.4 illustrates that when we set the mixing ratio concentration of O_2 is equal to zero no absorption peaks has been found at 1260nm, which is shown by blue color. Similarly no absorption peaks have been found for H_2O (red color) within 1100 to 1500 nm wavelength bands, for CO_2 (brown color) from 1570 to 1620 nm and for CH_4 (pink color) at around 1670 nm.

4.2.1 Effect of H_2O concentrations on radiance

In this section, we describe the synthetic radiance for the different concentrations of water vapor and radiance variation by changing the H_2O concentrations (mixing ratio concentration of water) within Argus wavelength band. H_2O is the main absorber of solar radiation in the atmosphere. The 13 million tons of water in the atmosphere are responsible for about 70% of all atmospheric absorption of radiation, mainly in the infrared region, where water shows strong absorption features [Feistel R., et al., 2016]. The water absorption spectrum is very complex [Bernath P.F., et al., 2014]. All other mixing ratios concentrations are the same as in the U.S. Atmospheric Model 1976, with albedo = 0.3. Figure 4.5 shows the variation in the radiance by changing H_2O concentration from 1% to 2%. This is due to the strong features of water vapor absorption within two wavelength bands from 1100 to 1200 nm and from 1300 to 1500 nm.

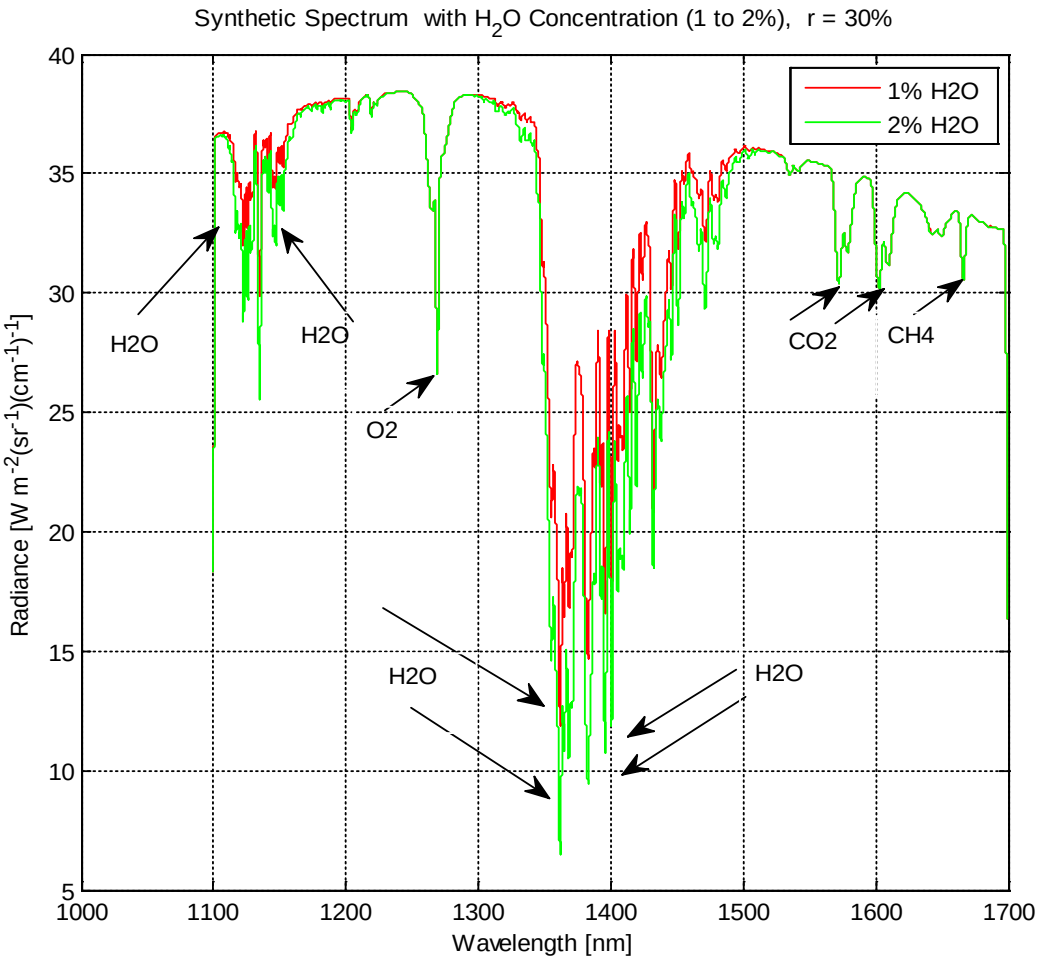

Fig. 4.5. Expected radiance (GENSPECT-synthetic spectrums with H_2O from 1% to 2%).

Figures 4.6 through 4.8 illustrate the variation in the radiance by changing H_2O concentration from 30% to 100%. In all these cases, we change the water vapor concentration to estimate the overall spectral change in radiance for the radiance enhancement model. We found two different types of absorption radiance characteristics. The spectral layout we obtained indicates that, for typical atmospheric conditions according to the U.S. Atmospheric 1976 data, the radiance change near 1100 to 1200 nm

is sensitive to changes in the integrated amount of water vapor, whereas the wavelength bands near 1300 to 1500 nm are repeatedly saturated.

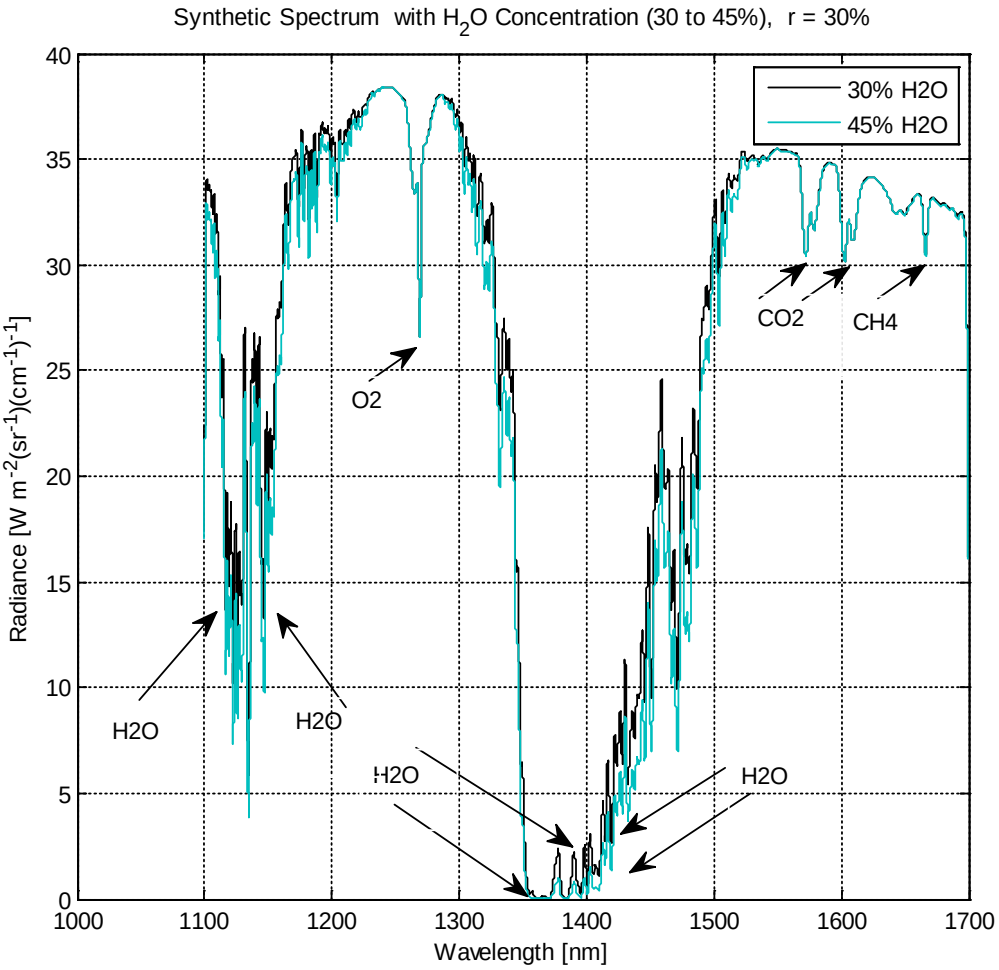

Fig. 4.6. Expected radiance (GENSPECT-Synthetic spectrums with H_2O from 30% to 45%).

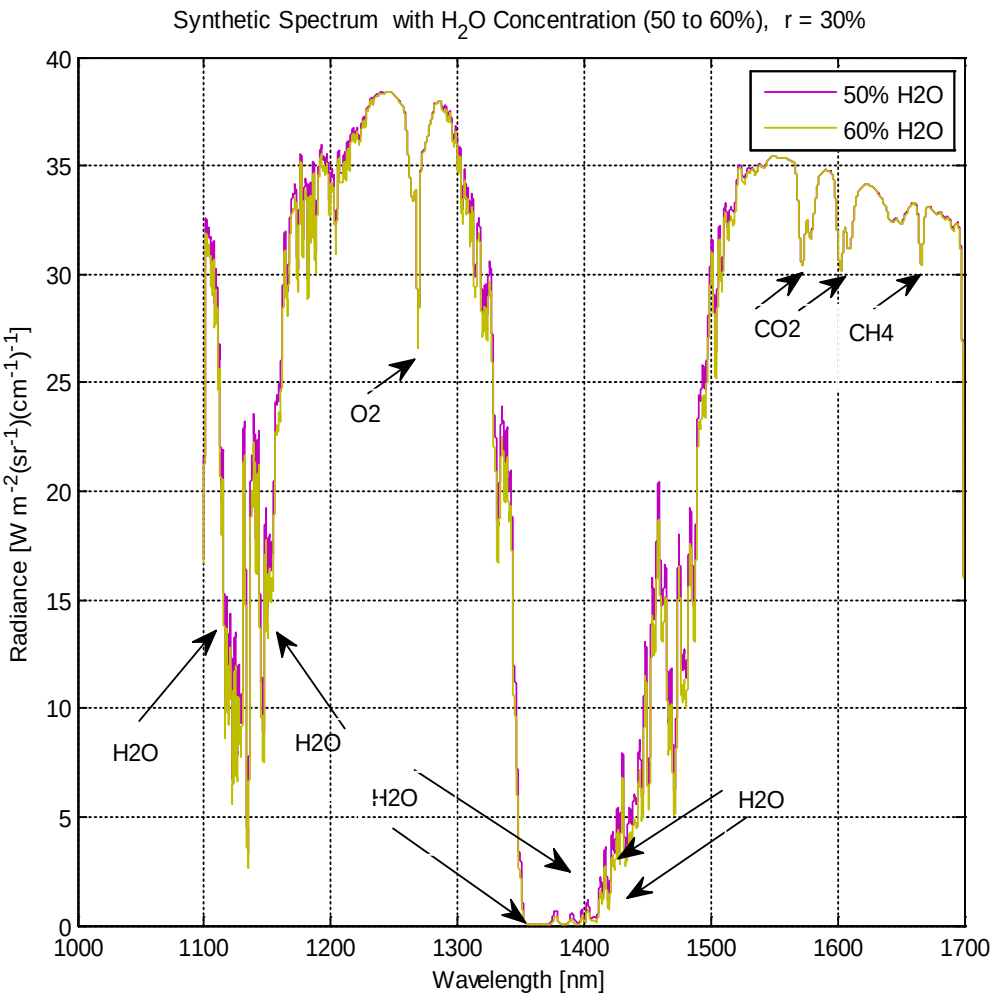

Fig. 4.7. Expected radiance (GENSPECT-Synthetic spectrums with H_2O from 50% to 60%).

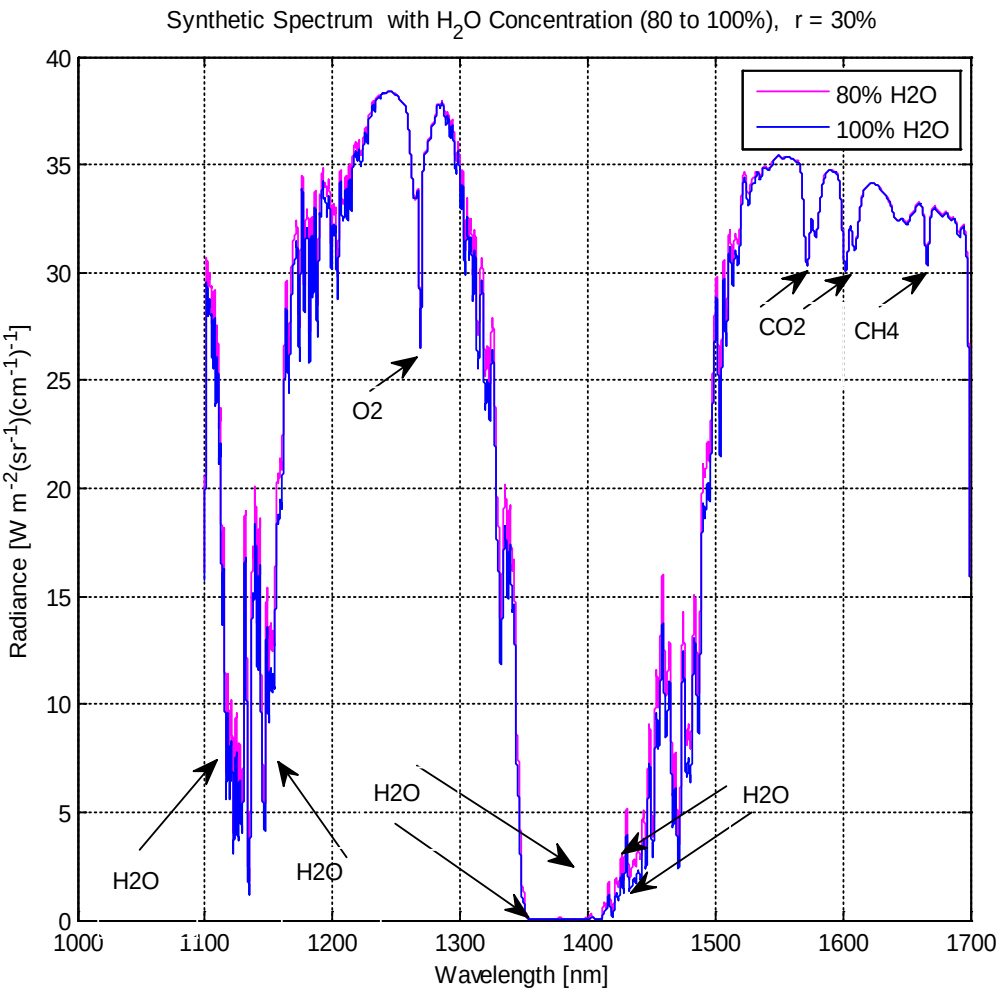

Fig. 4.8. Expected radiance (GENSPECT-Synthetic spectrums with H_2O from 80% to 100%).

Table 4.4 illustrates the variation of model spectral radiance in terms of minimum, maximum, mean, and range of radiance due to the various levels of water vapor relative to that specified in the standard atmosphere was varied between 1 to 100%.

Table 4.4. The radiance (Wm^{-2} sr^{-1} $(1/cm)^{-1}$) variations of model spectra within Argus band with change in H_2O concentration.

Radiance Type	1%	2%	30%	45%	50%	60%	80%	100%
Minimum	11.880	6.742	0.0135	0.001	4.6e-4	8.8e-5	3.1e-6	1.0e-7
Maximum	38.430	38.430	38.420	38.420	38.420	38.420	38.410	38.410
Mean	34.070	32.970	26.440	25.200	24.870	24.290	23.350	22.610
Range	26.550	31.960	38.410	38.420	38.420	38.420	38.410	38.410

The estimated absolute spectral radiance variability by changing water vapor concentration is from 0.1 to 38 Wm^{-2} sr^{-1} $(1/cm)^{-1}$. The estimated spectral radiance for no clouds varies from 0.1 to 15 Wm^{-2} sr^{-1} $(1/cm)^{-1}$ and for thick or thin cloud scenes varies from 26 to 38 Wm^{-2} sr^{-1} $(1/cm)^{-1}$. We can see the spectral saturation region in terms of the absorption features of H_2O starts at the 30 % level of atmospheric mixing ratio concentration of water as shown in Fig 4.5. The spectral absorption saturation features as shown in Fig 4.6 and Fig 4.8 are very dominant between 50 to 100 % of H_2O variation of water level concentration and can be negligible in terms of radiance (solar radiation absorbed not reflected), we used 30% H_2O concentration as a spectral saturation point, an input for the RE cloud model.

4.2.2 Effect of CO_2 concentrations on radiance

In this section, we describe the model radiance for the different CO_2 mixing ratio was increased by a factor of between 10 to 100%, with fixed concentration of atmospheric

mixing ratio of H_2O. Figure 4.9 illustrates the overall estimated radiative effect due to CO_2 the selected wavelength bands. The selected three areas 1, 2 and 3 show the typical spectral absorption radiance within Argus band. Figures 4.10 (a), (b) and (c) indicate that increasing the amount of CO_2 shows maximum sensitivity near Area no. 1 (1200 to 1230 nm), Area no.2 (1430 to 1446 nm) and Area no.3 (1570 to 1620 nm) respectively. The calculated CO_2 radiance from 10% to 100% gives an approximate sensitivity of radiance within the instrument range. Our full forward model allows us to predict the variation of radiance in the given atmospheric composition as shown in Table 4.5.

Table 4.5. The radiance (Wm^{-2} sr^{-1} $(1/cm)^{-1}$) variations of model spectra within Argus band with change in CO_2 concentration.

Radiance Type	**10%**	**20%**	**40%**	**80%**	**100%**
Minimum	0.080	0.080	0.080	0.080	0.080
Maximum	38.730	38.730	38.730	38.730	38.730
Mean	27.810	27.790	27.760	27.700	27.680
Range	38.650	38.650	38.650	38.650	38.650

The estimated change in radiance with respect to wavelength and CO_2 is not quite high, we observe negligible variability in the spectral statistics but it may affect the detection of clouds in terms of their chemical properties as well as scattering and absorption features. In few cases, the change in CO_2 absorption features is crucial to the increase in the spectral radiance profile [Jagpal R., 2011; Salomon E., 2013]. It is also

found that water vapor has strong absorption especially between Areas no. 1 and 2, resulting in the observed discrepancies in these regions.

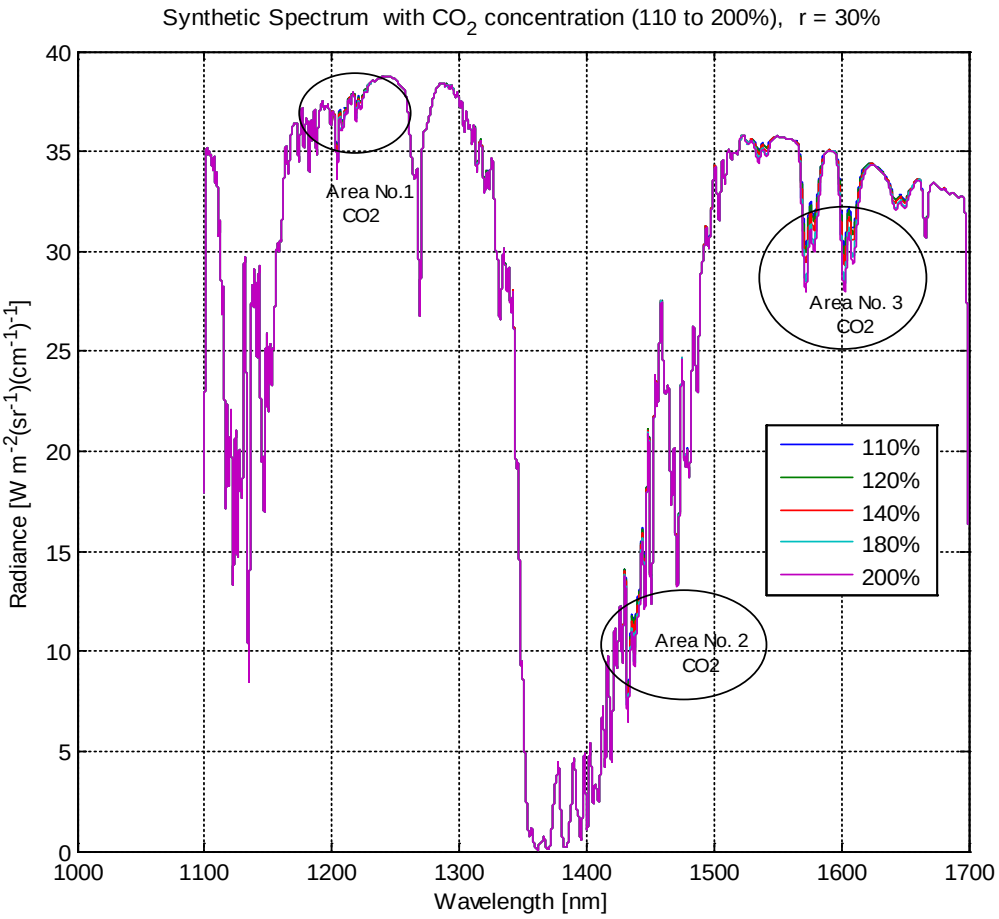

Fig. 4.9. Expected radiance (GENSPECT-Synthetic spectrum of CO_2 from 110% to 200%) (show different areas of absorption effects by increasing concentration).

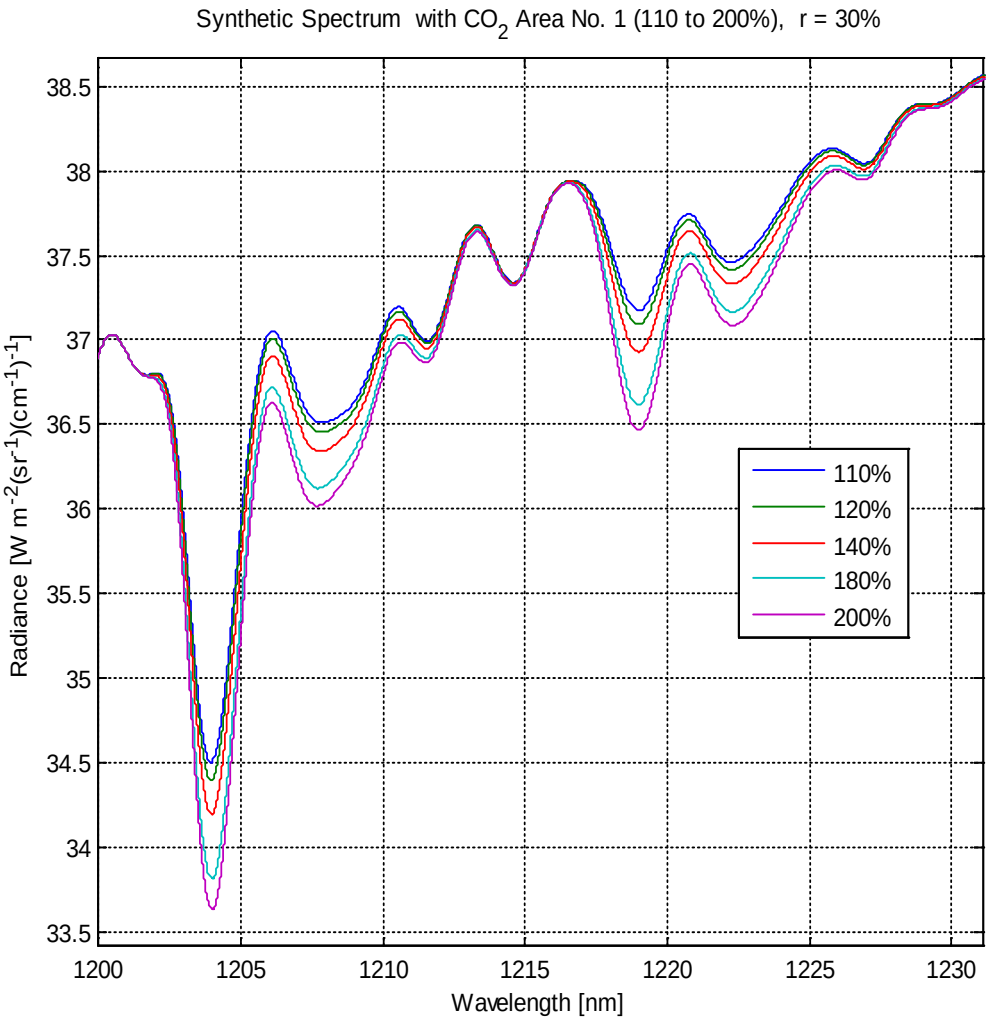

Fig. 4.10 (a). Area 1: Radiance change from 1202 to 1230 nm.

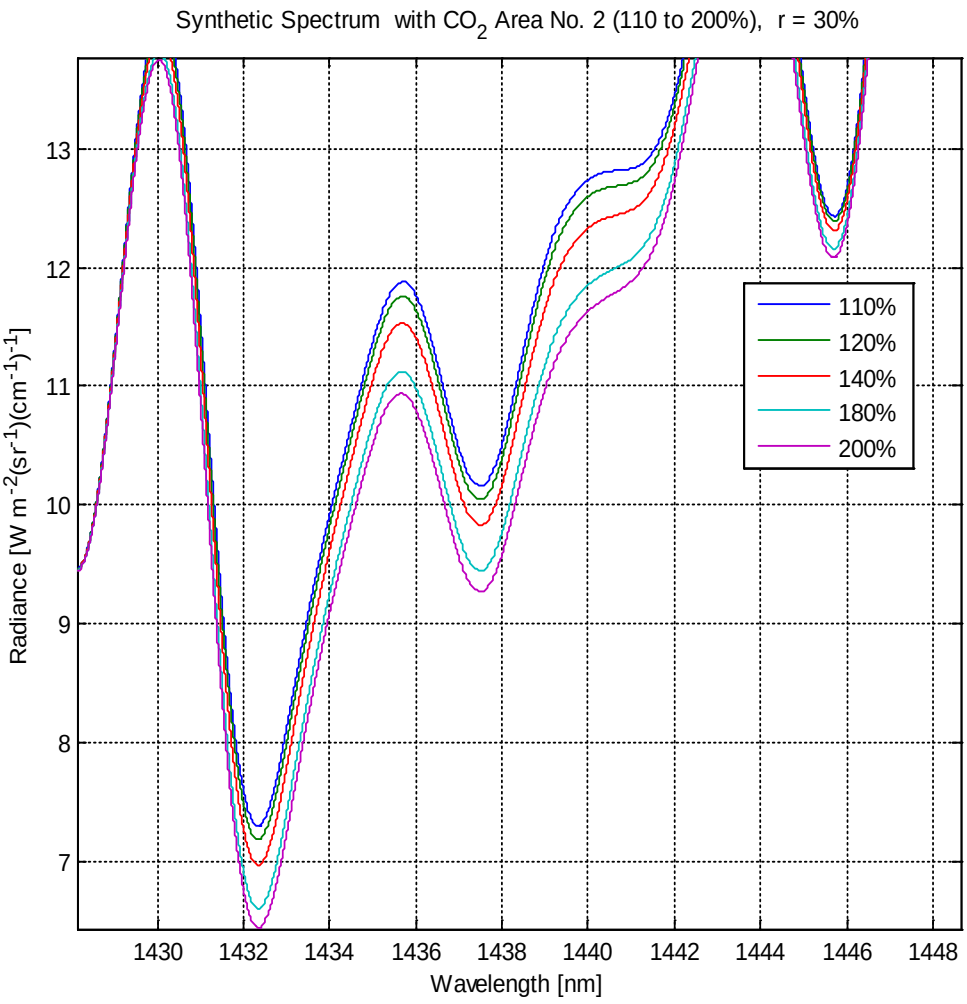

Fig. 4.10 (b). Area 2: Radiance change from 1430 to 1446 nm.

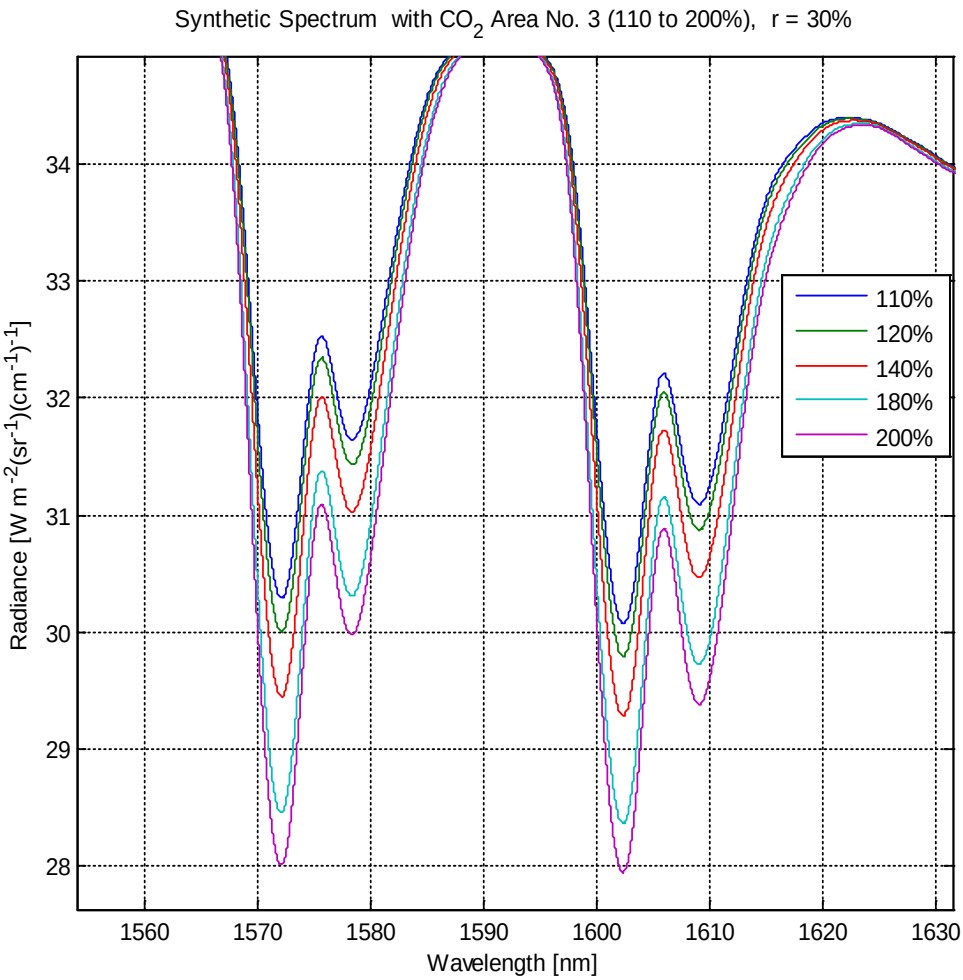

Fig. 4.10 (c). Area 3: Radiance change from 1570 to 1630 nm.

4.2.3 Effect of surface albedo on radiance

In this section, we estimate the synthetic radiance for the different values of Earth surface albedo with the fixed concentration of atmospheric mixing ratio of other greenhouse gases within Argus wavelength bands. This is the most crucial factor for estimating the types of reflecting surfaces and as well as a very critical factor to detect clouds. The output estimated radiance of the apparent selection of albedo at the TOA gives the better understanding for detecting the clear and cloudy sky.

The estimated absolute spectral radiance is illustrated in Table 4.6 with Earth surface albedo varies over a range of 0.1 to 0.9. It is found that by changing this parameter resulted in the largest variation in the radiance of the model spectra, with increases over an order of magnitude in the various characteristics.

Table 4.6. The radiance (Wm^{-2} sr^{-1} $(1/cm)^{-1}$) variations of model spectra within Argus band with change in surface albedo (H_2O = 30%).

Radiance Type	**0.1**	**0.2**	**0.3**	**0.4**	**0.5**	**0.6**	**0.7**	**0.8**	**0.9**
Minimum	0.0045	0.0089	0.0135	0.0179	0.0224	0.0269	0.0314	0.0359	0.0404
Maximum	12.810	25.610	38.420	51.230	64.040	76.840	89.650	102.5	115.30
Mean	8.812	17.620	26.440	35.250	44.060	52.870	61.680	70.500	79.310
Range	12.800	25.610	38.410	51.21	64.010	76.820	89.62	102.40	115.20

Figure 4.11 shows change in radiance by increasing the surface albedo from 0.1 to 0.25, it can be seen that the overall radiance profile has been shifted from 12 to 32 Wm^{-2} sr^{-1} $(1/cm)^{-1}$. Similarly, Figure 4.12 and Figure 4.13 illustrates the higher radiance from 38 to 76 Wm^{-2} sr^{-1} $(1/cm)^{-1}$ and 76 to 115 Wm^{-2} sr^{-1} $(1/cm)^{-1}$ by increasing albedo from 0.30 to 0.60 and from 0.60 to 0.90 respectively. The estimated absolute spectral radiance for no clouds are varies from 10 to 15 Wm^{-2} sr^{-1} $(1/cm)^{-1}$ (with albedo less than 0.15), for thin cloud scenes are varies from 25 to 38 Wm^{-2} sr^{-1} $(1/cm)^{-1}$ (with albedo from 0.25 to 0.30), for middle level cloud (thick/thin) scenes varies from 40 to 75 Wm^{-2} sr^{-1} $(1/cm)^{-1}$ (with albedo from 0.35 to 0.60), for thick cloud or ice cloud scenes varies from 75 to 115 Wm^{-2} sr^{-1} $(1/cm)^{-1}$ (with albedo from 0.60 to 0.90).

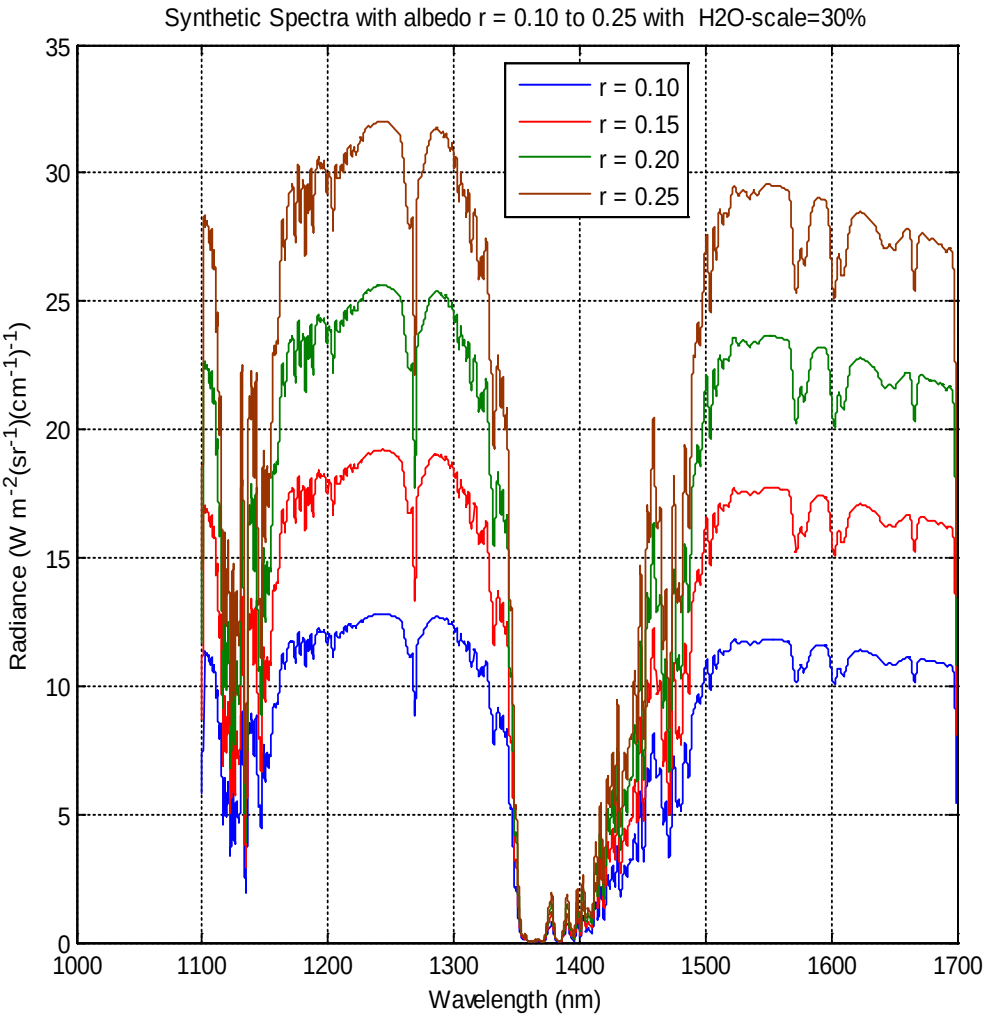

Fig. 4.11. Expected radiance (GENSPECT-Synthetic spectrum with different albedo from 0.10 to 0.25 with H_2O =30%).

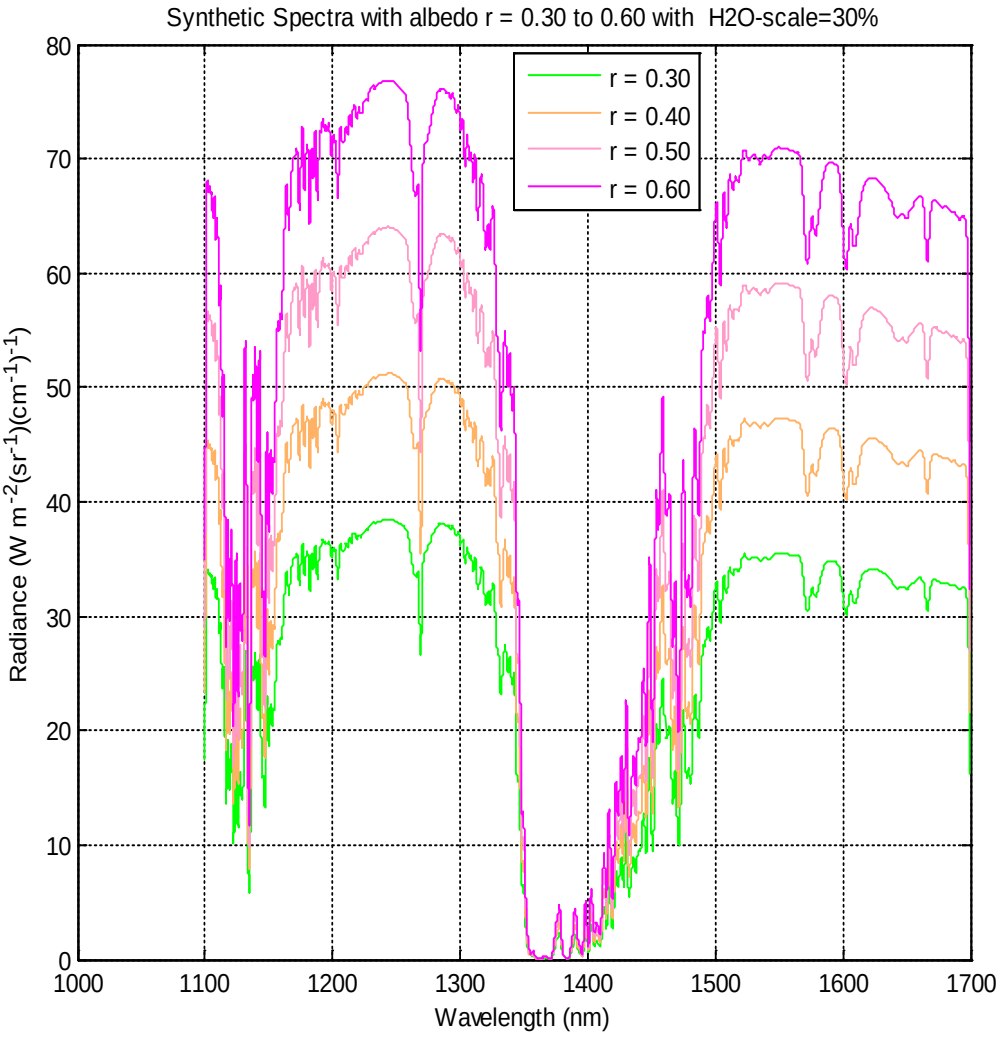

Fig. 4.12. Expected radiance (GENSPECT-Synthetic spectrum with different albedo from 0.30 to 0.60)

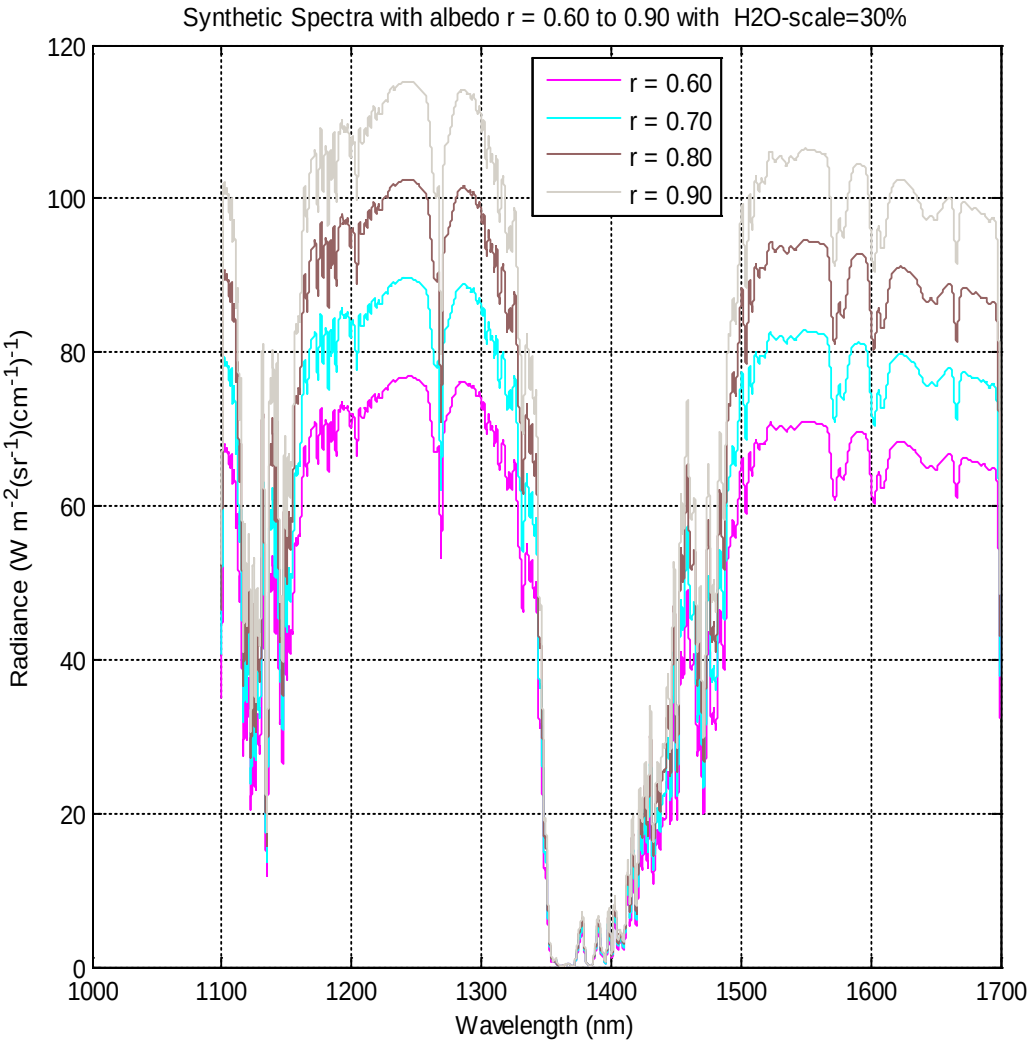

Fig. 4.13. Expected radiance (GENSPECT-Synthetic spectrum with different albedo from 0.60 to 0.90).

It is evident that the albedo parameter is the most important input to the RE model in terms of radiance variability, and thus needs to be considered as a key parameter when comparing the measured Argus spectra to the model. By calculating the radiance enhancement of the measured Argus data relative to the model spectra at different albedos, the effective albedo for the observed spectra can be estimated.

4.2.4 Effect of altitudes on radiance

The variation in the vertical profile in terms of height is also a very important phenomenon for the detection of clouds within the different atmospheric layers. In general, the solar irradiance increases with increasing altitude above sea level. This increase is mainly due to a distinct increase of direct irradiance [Blumthaler, M., et al. 1997]. As discussed in chapter 2, the Beer-Lambert-Law depends strongly on wavelength increase with altitude. The estimation of spectral irradiance with different altitudes show the dependence of water vapor concentrations and albedo effect within NIR range. The strong decrease of radiance absorption profile is shown in Figure 4.14. This is due to the high absorption features of H_2O within the full wavelength band of the instrument specially within the wavelength

bands from 1140 to 1200 nm and 1350 to 1500 nm as discussed in section 4.2.1.

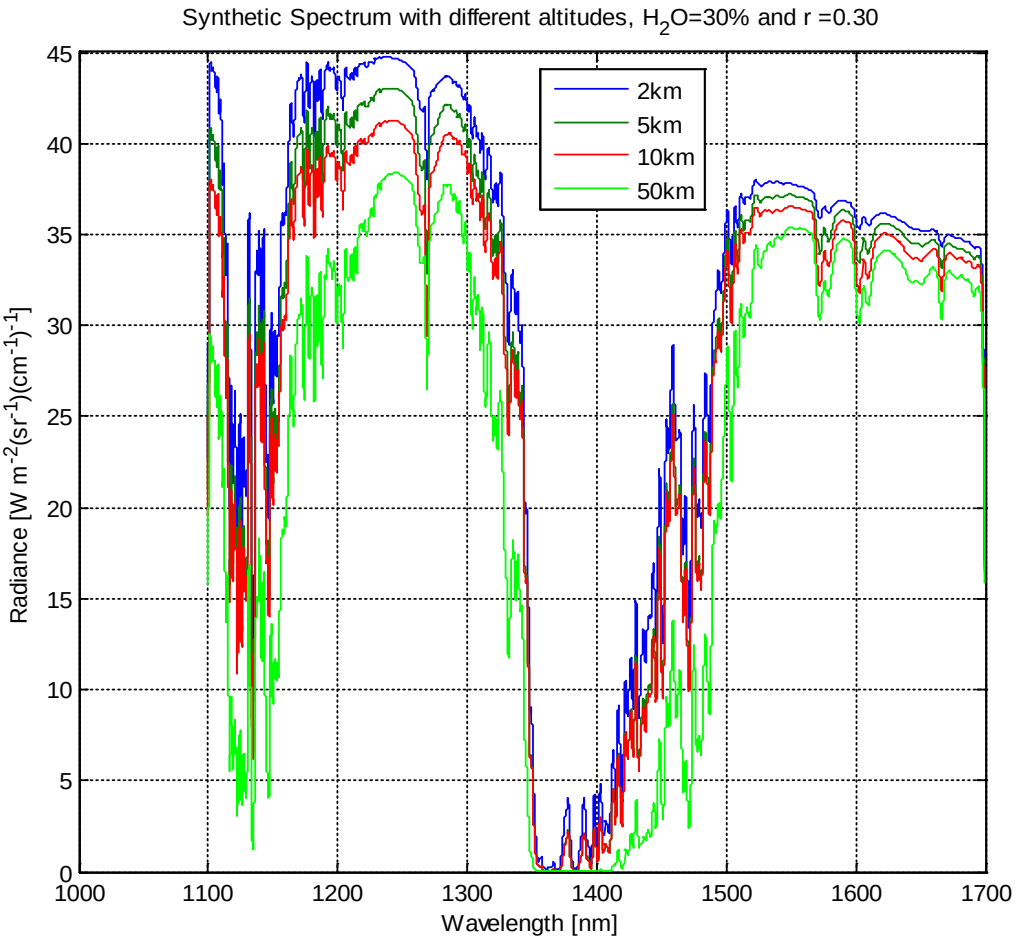

Fig. 4.14. Expected radiance (GENSPECT-Synthetic spectrum with different altitudes from 2 to 50 km).

Table 4.7 shows the estimated absolute radiance for different altitudes. It is found that by increasing this parameter resulted in the decreasing of radiance profile. This is due to the high absorption features of H_2O and surface albedo at different atmospheric layers.

Table 4.7. The radiance (Wm^{-2} sr^{-1} $(1/cm)^{-1}$) variations of model spectra within Argus band with change in altitudes.

Radiance Type	02 km	05 km	10 km	50 km
Minimum	0.0482	0.0102	0.0104	1e-7
Maximum	44.780	43.040	41.250	38.410
Mean	31.340	29.080	27.960	22.610
Range	44.730	43.030	41.240	38.410

The estimated parametrization of radiance profile by synthetic model has been applied for the present study for the detection of cloud by using RE technique. It is concluded that H_2O and albedo variations are the major source for analyzing the cloud scene within the Argus NIR wavelength band.

4.3 Argus Retrieval Results for Cloud Detection

The Argus weeks per passes with different observation numbers for the RE model are presented and discussed in the following sections.

4.3.1 October 30, 2009 (week 08 pass 61 observations 64/116/196/238)

The four selected spectrums for the detection and classification of cloud scene shown in Figure 4.15 was observed by Argus over the Arabian Sea on October 30, 2009 at latitudes and longitudes (6° 30' 36" N) and (60° 57' 43.92" E), (3° 12' 19.8" N) and (60° 7' 35.76" E), (1° 31' 35.4" S) and (59° 14' 52.44" E), (4° 16' 5.16" S) and (58° 44' 51.36" E) for observation numbers 64, 116, 196 and 238 respectively. We observe the signature of oxygen at 1250 nm. Whereas carbon dioxide absorption is found near 1560 to 1600 nm, we can also observe the signature of methane at 1665nm. The water absorption features have also been found at around 1120 to 1175 nm and 1380 to 1450 nm for the observation numbers 64, 196 and 238. Observation number 64 has high radiance profile and it may be due to thick or ice clouds.

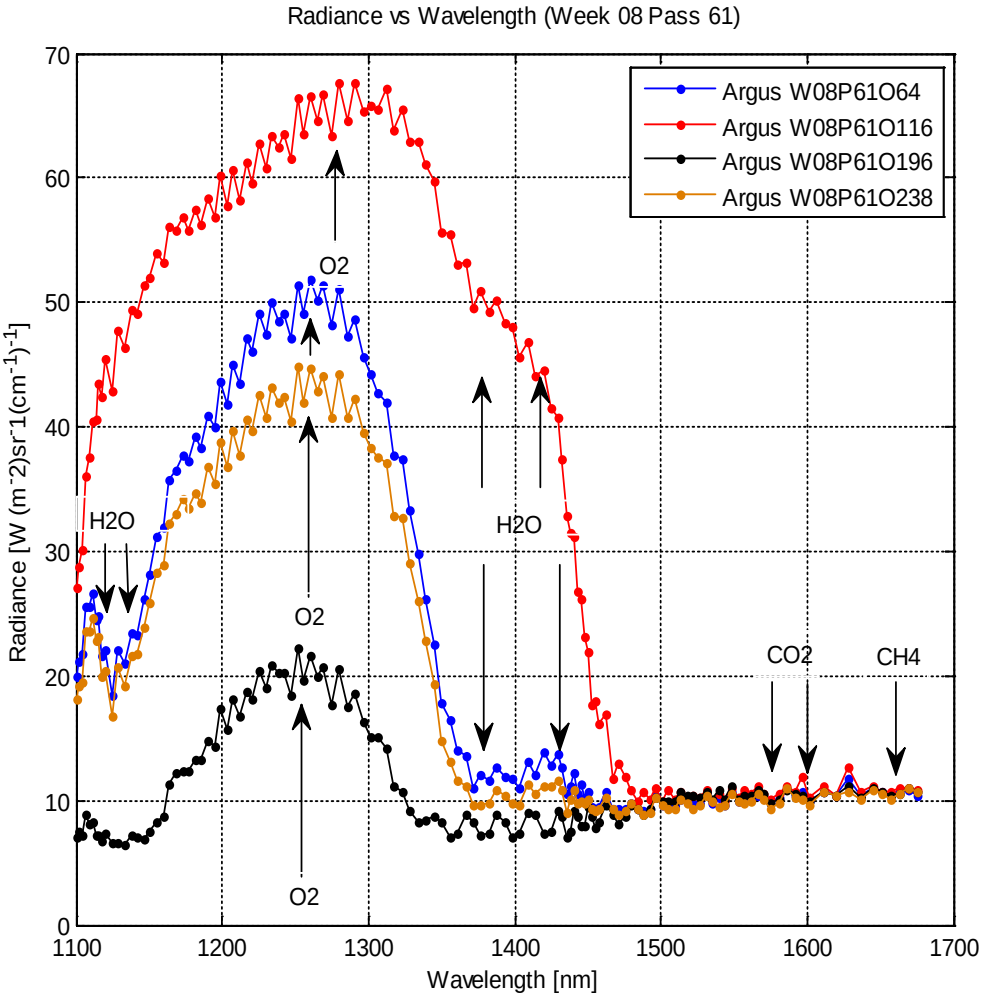

Fig. 4.15. Argus spectra - radiance vs wavelength of week 08 pass 61 observation number 64/116/196/238 (October 30, 2009, over the Arabian Sea).

4.3.2 March 04, 2010 (week 14 pass 52 observations 22/100/120/124)

Figure 4.16 show the observed spectrums with the corresponding radiance profile recorded near Toronto, Canada on March 04, 2010 at latitudes and longitudes (47° 22' 26.4" N) and (77° 43' 42.96" W), (42° 50' 28.68" N) and (79° 43' 8.04" W), (42° 50' 28.79" N) and (79° 43' 8.13" W), (42° 17' 21.48" N) and (79° 56' 43.08" W) for observation numbers 22, 100, 120 and 124 respectively. All the spectra clearly observe H_2O absorption

prominently near 1120 nm and around 1400 nm, O_2 absorption at 1250nm, CO_2 absorption at 1570 nm and 1600nm, and signature of CH_4 at 1665nm. The spectral radiance shift from 10 to approximately 60 Wm^{-2} sr^{-1} $(1/cm)^{-1}$, show in each spectrum due to the different types of surface albedo, latitudes and Argus viewing angle.

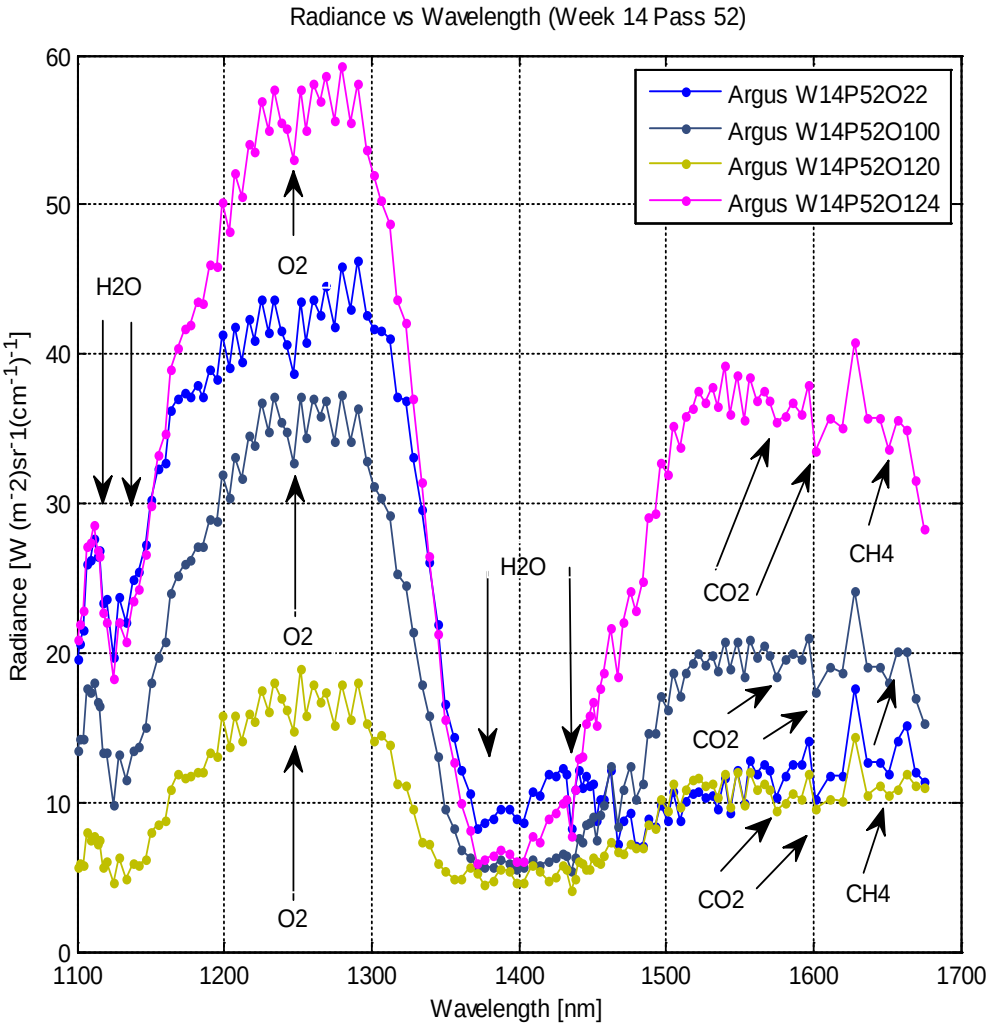

Fig. 4.16. Argus spectra - radiance vs wavelength of week 14 pass 52 observation number 22/100/120/124 (March 04, 2010, near Toronto, Canada).

4.3.3 August 14, 2013 (week 75 pass 43 observations 19/30/43/65)

The radiance profile with the prominent signatures of greenhouse gases O_2, H_2O, CO_2 and CH_4 has been shown in Figure 4.17 taken on August 14, 2013 over north pacific ocean at a longitudes and longitudes (31° 45' 33.12" N) and (148° 12' 48.6" E), (28° 55' 23.88" N) and (147° 33' 54.72" E), (25° 34' 55.92" N) and (146° 48' 29.88" E), (19° 55' 28.56" N) and (145° 32' 53.16" E) for observation numbers 19, 30, 43 and 65 respectively. The absolute radiance profile varies by latitude due to the solar geometry of the Argus observation.

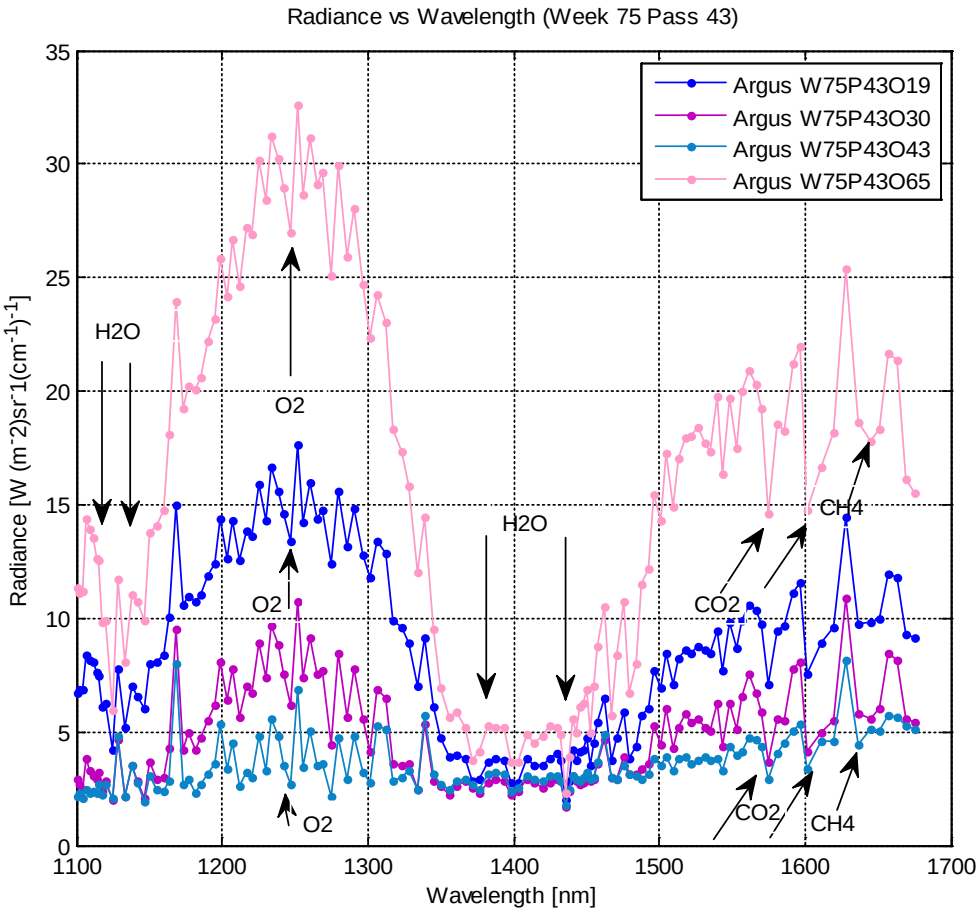

Fig. 4.17. Argus spectra - radiance vs wavelength of week 75 pass 43 observation number 19/30/43/65.

4.4 RE Results (Synthetic vs Observed)

The detection of cloud or non-cloud scene is implemented by finding the maximum or minimum RE within selected NIR wavelength bands of O_2, H_2O, CO_2 and CH_4. [Siddiqui, R., et al., 2015]. The RE approach is based on the mean value of the ratio of the difference of the observed data with simulated data for the selected week per pass with single scan or multiple scan [Siddiqui, R., et al., 2015]. Rayleigh scattering is also used as one of the input parameter in the model. In this model, the cloud detection is

determined by selecting the Sun elevation angle, satellite nadir angle, variable path length, atmospheric water vapor, variable albedo, and cloud structure over land or sea. We assume the reflecting surface as a Lambertian surface, which is defined as a reflecting surface where the apparent brightness is constant regardless of the observer's angle of view.

The RE model loads a synthetic spectrum at different or fixed water concentrations and a set of all selected observed spectra as described in the following different scenarios:

4.4.1 Case No. 1: RE with albedo = 0.1 (W08P61O64/116/196/238)

Figure 4.18 shows a comparative plot of synthetic spectra (r = 0.1, H_2O = 30%, pink color) with each of the four-selected observed spectrum of week 08 pass 61 in the set all of the four spectrums show a high spectral absolute radiance in contrast with synthetic spectra with albedo is equal to 0.1.

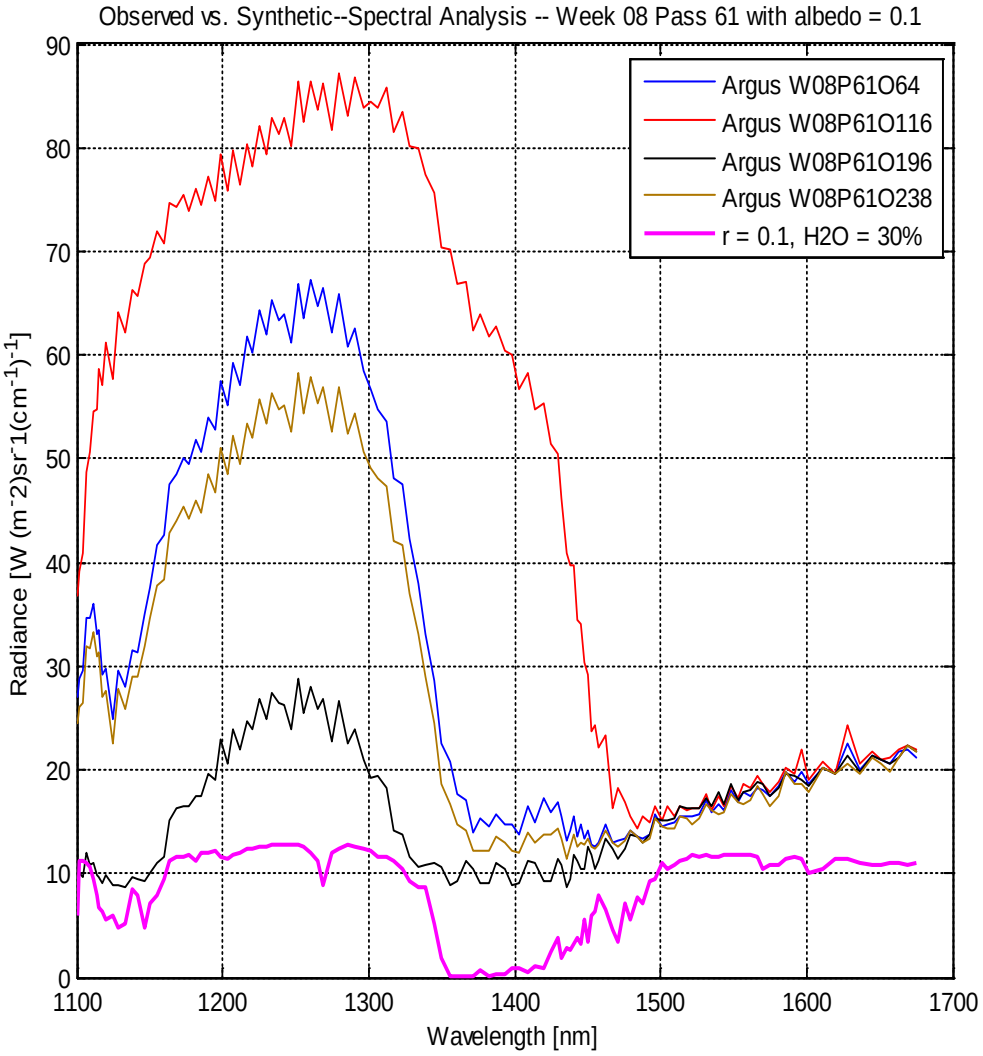

Fig. 4.18. RE model: Argus spectra (observed) of week 08 pass 61 with different observations number 64/116/196/238 vs. GENSPECT model spectra (synthetic) with (r=0.1, H_2O = 30%).

The model calculates the radiance enhancement (RE) and combined radiance enhancement (CRE) of all the four selected observed spectra relative to the synthetic model in four bands of interest as shown in Table 4.8. In this case, we set the surface reflectivity is equal to 0.1 (with H_2O = 30%) in our synthetic model to calculate the enhancement factor within the full spectral wavelength bands. The RE1 (H_2O & O_2 band), RE2 (H_2O & CO_2

band), RE3 (CO_2 band) and RE4 (CH_4 band) of observation number 116 show a probability of thick clouds. In this case the spectra with cloud have the probability of more reflected radiance because in the presence of clouds a significance factor of the solar radiation is immediately reflected back to space by clouds. The same effect can also be found by calculating the CRE (observation no. 116) of all the selected four greenhouse gases. Observation numbers 64 and 238 also show high RE's and CRE's having a possibility of middle or high clouds (thick or thin), similarly observation 196 show thick clouds or non-cloud scene.

Table 4.8. RE & CRE of week 08 pass 61 with observations 64/116/196/238, albedo = 0.1

Week/Pass/Obs.	RE1	RE2	RE3	RE4	CRE1	CRE2	CRE3	Types of cloud
08/61/64	3.71928	12.2285	1.08919	0.713446	2.75868	0.304149	17.7504	middle/thin
08/61/116	5.64717	44.2513	2.12665	0.768573	6.8973	0.127616	52.7937	Thick
08/61/196	0.743106	6.67291	0.925828	0.722761	4.55219	0.111362	9.0646	no/thick
08/61/238	3.15884	10.237	1.01861	0.675258	2.66999	0.30857	15.0897	middle/thick

Obs. (116) $_{red}$ = Thick clouds, Obs. (64) $_{blue}$ = middle/thin clouds, Obs. (238) $_{green}$ = middle/thick clouds and Obs. (196) $_{grey}$ = thick clouds or non-cloudy scenes.

4.4.2 Case No. 2: RE with albedo = 0.2 (W08P61O64/116/196/238)

Figure 4.19 shows a comparative plot of synthetic spectra (r = 0.2, H_2O = 30%, green color) with each of the four-selected observed spectrum in the set. The three observations numbers 64, 116 and 238 show high spectral absolute radiance in contrast

with synthetic spectra with albedo is equal to 0.2. The observation number 196 shows a good agreement with synthetic spectra.

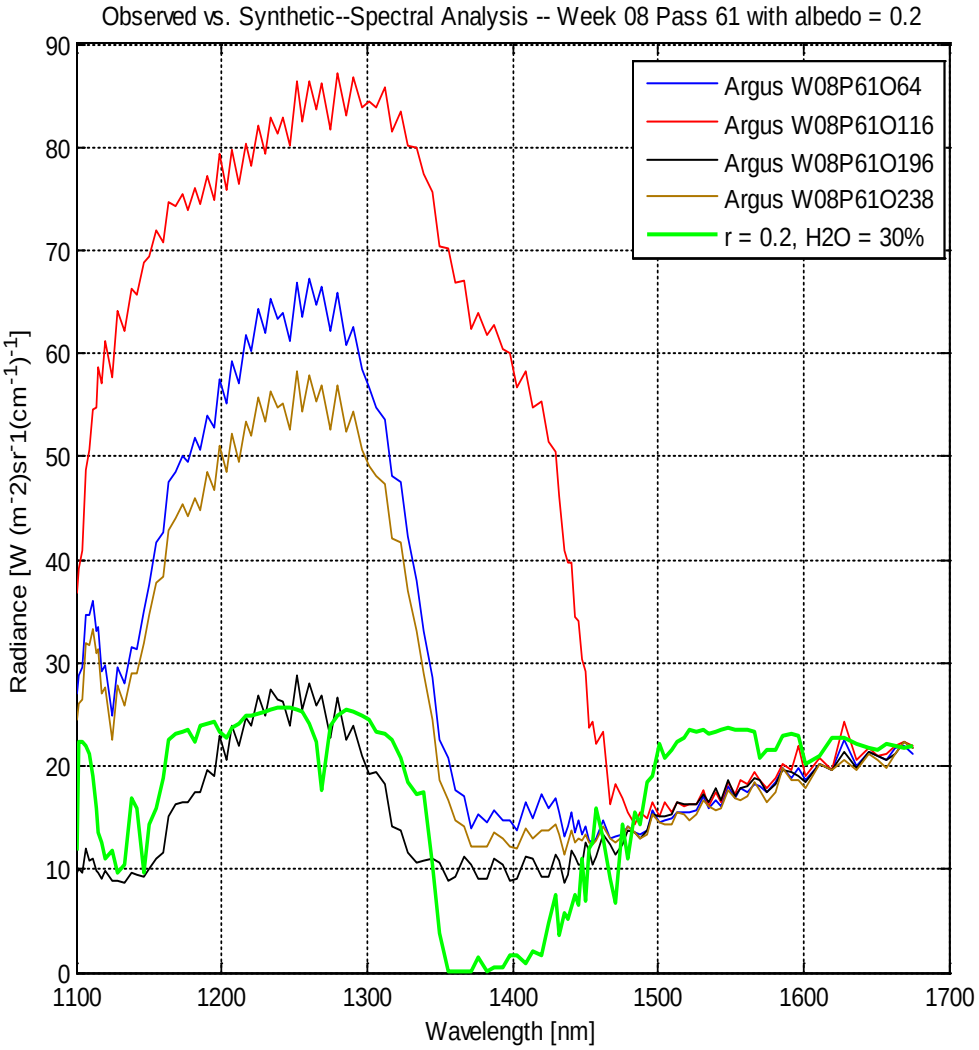

Fig. 4.19. RE model: Argus spectra (observed) of week 08 pass 61 with different observations number 64/116/196/238 vs. GENSPECT model spectra (synthetic) with (r=0.2, H_2O = 30%).

In this case 2, we set the surface albedo is equal to 0.2 (with H_2O = 30%) in our synthetic model to calculate the enhancement ratio within the full spectral wavelength bands of Argus. When we increase the surface albedo, the RE1, RE2 and RE3 of

observation number 116 still show a high radiance enhancement as shown in Table 4.9. The RE4 shows good agreement within this band with negative (RE effect) in terms of no absolute radiance change within methane wavelength band of interest. The same high CRE's effect still shows with observation no. 116. Observation numbers 64 and 238 show same effects as compared with case 1 with high RE's and CRE's. When we increase the albedo effect, the observation 196 shows good agreement for the probability of low clouds or non-cloud scene.

Table 4.9. RE & CRE of week 08 pass 61 with observations 64/116/196/238, albedo = 0.2

Week/Pass/Obs.	RE1	RE2	RE3	RE4	CRE1	CRE2	CRE3	Types of cloud
08/61/64	1.35964	5.61423	0.0445925	-0.143277	4.61559	0.242177	6.87519	middle/thin
08/61/116	2.32359	21.6257	0.563323	-0.115713	9.7948	0.107446	24.3969	thick
08/61/196	-0.128447	2.83645	-0.0370862	-0.138619	-10.6208	0.0452843	2.5323	no/thick
08/61/238	1.07942	4.6185	0.00930499	-0.162371	5.03628	0.233716	5.54486	middle/thick

Obs. (116) $_{red}$ = Thick clouds, Obs. (64) $_{blue}$ = middle/thin clouds, Obs. (238) $_{green}$ = middle/thick clouds and Obs. (196) $_{grey}$ = thick clouds or non-cloudy scenes.

4.4.3 Case No. 3: RE with albedo = 0.3 (W08P61O64/116/196/238)

Figure 4.20 illustrates a comparative plot of synthetic spectra (r = 0.3, H_2O = 30%, orange color) with each of the four-selected observed spectrum in the set. In case 3, the three observations numbers 64, 116 and 238 still show high spectral absolute radiance in contrast to the synthetic spectra with albedo is equal to 0.3 and gives a high degree of

assurance for the detection of the middle and high level of clouds by using Argus data set. The observation number 196 shows less absolute radiance within 1100 to 1200 nm (H_2O band) and from 1200 to 1350 nm (O_2 and H_2O band).

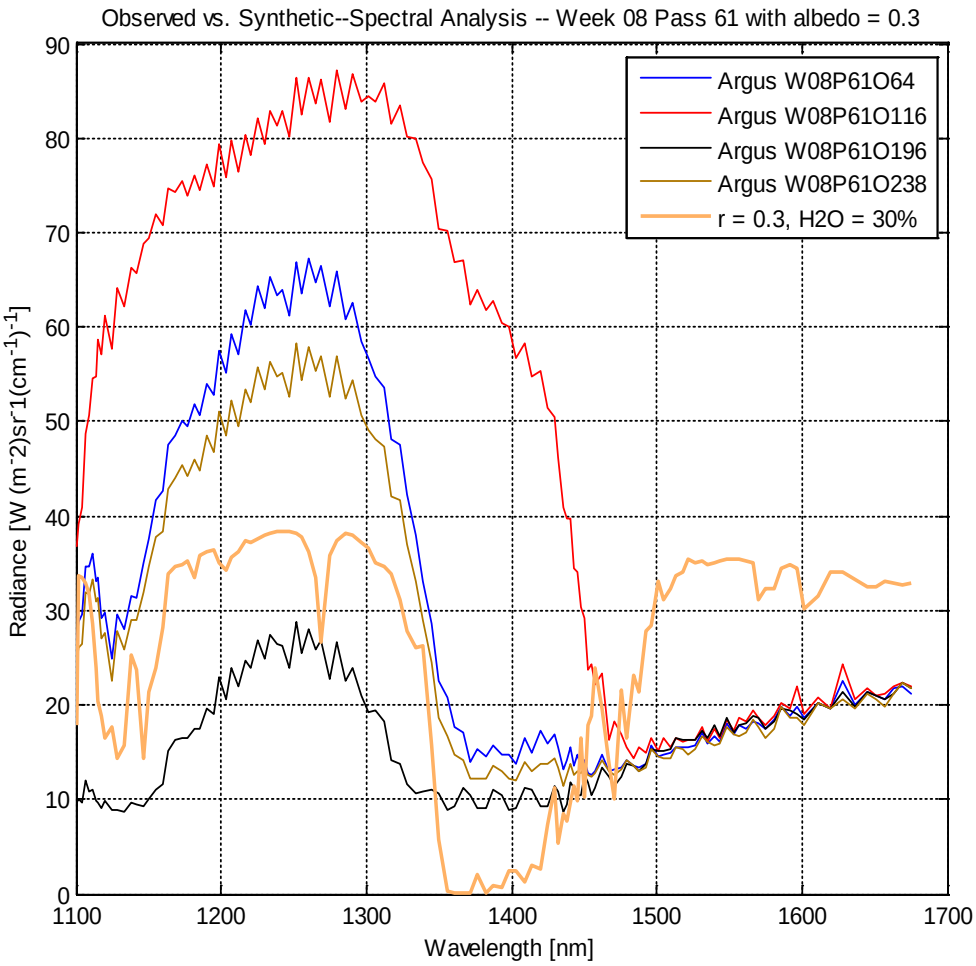

Fig. 4.20. RE model: Argus spectra (observed) of week 08 pass 61 with different observations number 64/116/196/238 vs. GENSPECT model spectra (synthetic) with (r=0.3, H_2O = 30%).

In this case 3, we set the surface albedo is equal to 0.3 (with H_2O = 30%). When we increase the surface albedo, the RE1, RE2 and RE3 of observation number 116 still show the same result as discussed in case 1 and case 2. The results are shown in Table

4.10. The RE3 and RE4 show negative radiance ratios, because of high surface albedo and low absorption effects within this wavelength band. The observation number 64 and 116 show high CRE's effect, suggesting high possibility of cloud scenes. When we increase the albedo effect, the observation 196 shows good agreement for the probability of low clouds or non-cloudy scene.

Table 4.10. RE & CRE of week 08 pass 61 with observations 64/116/196/238, albedo = 0.3

Week/Pass/Obs	RE1	RE2	RE3	RE4	CRE1	CRE2	CRE3	Types of cloud
08/61/64	0.573093	3.40949	-0.303605	-0.428851	23.6374	0.168088	3.25013	middle/thin
08/61/116	1.21572	14.0838	0.0422154	-0.410476	17.4900	0.0863209	14.9312	thick
08/61/196	-0.418965	1.55764	-0.358057	-0.425746	-1.84399	-0.268975	0.354867	no/thick
08/61/238	0.386279	2.74567	-0.32713	-0.441581	-49.6489	0.140687	2.36324	middle/thick

Obs. (116) $_{red}$ = Thick clouds, Obs. (64) $_{blue}$ = middle/thin clouds, Obs. (238) $_{green}$ = middle/thick clouds and Obs. (196) $_{grey}$ = thick clouds or non-cloudy scenes.

4.4.4 Case No. 4: RE with albedo = 0.5 (W08P61O64/116/196/238)

Figure 4.21 illustrates a good agreement between absolute value of synthetic and observed radiance spectrum, especially for observation number 64 and 238 with surface albedo is equal to 0.5. In case 4, the observation number 116 still shows high spectral absolute radiance in contrast with synthetic spectra with albedo is equal to 0.5, resulting high level of clouds.

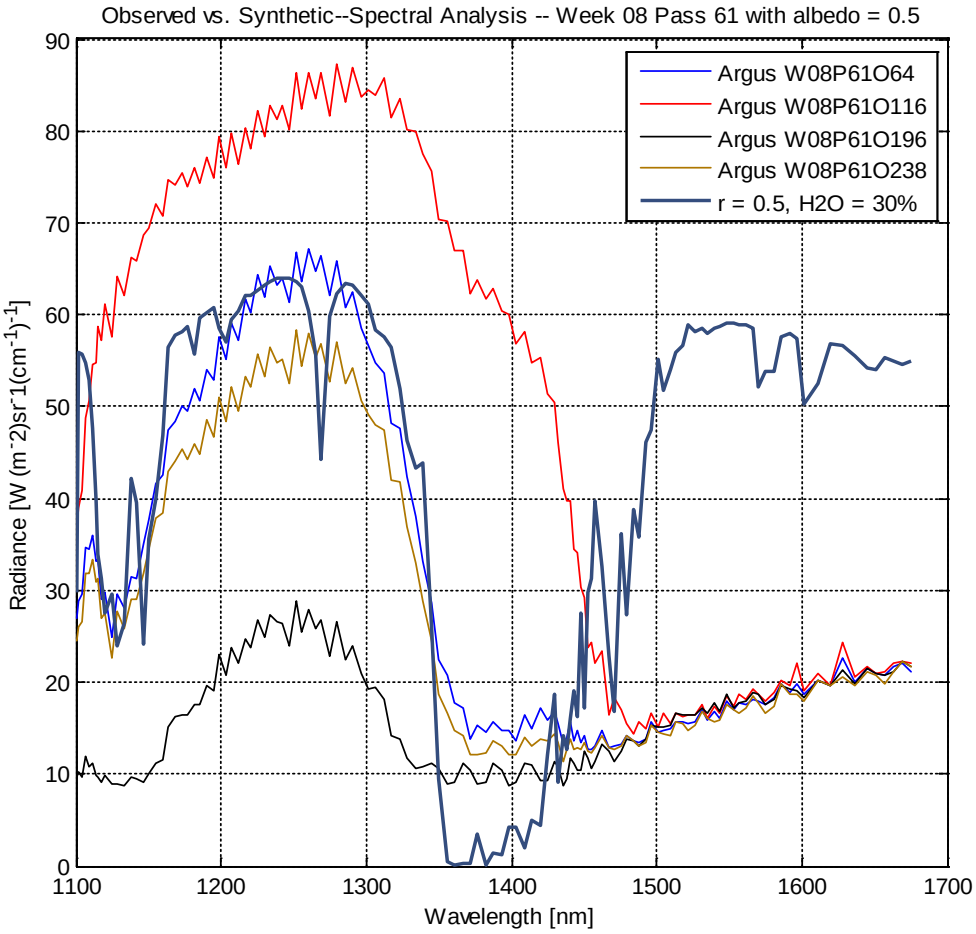

Fig. 4.21. RE model: Argus spectra (observed) of week 08 pass 61 with different observations number 64/116/196/238 vs. GENSPECT model spectra (synthetic) with (r=0.5, H_2O = 30%).

All the RE's and CRE's show good agreement of middle and low clouds for the observation numbers 64 and 238, but observation number 116 shows high RE2 and CRE3, suggesting thick clouds. The results are shown in Table 4.11.

Table 4.11. RE & CRE of week 08 pass 61 with observations 64/116/196/238, albedo = 0.5

Week/Pass/Obs	RE1	RE2	RE3	RE4	CRE1	CRE2	CRE3	Types of cloud
08/61/64	-0.0561444	1.64569	-0.582163	-0.657311	-2.30665	-0.034116	0.350075	middle/thin
08/61/116	0.329434	8.05026	-0.374671	-0.646285	-25.4071	0.0409222	7.35874	thick
08/61/196	-0.651379	0.534581	-0.614834	-0.655448	-0.409068	-1.21848	-1.38708	no/thick
08/61/238	-0.168233	1.2474	-0.596278	-0.664948	-1.49716	-0.134867	-0.182058	middle/low

Obs. (116) $_{red}$ = Thick clouds, Obs. (64) $_{blue}$ = middle/thin clouds, Obs. (238) $_{green}$ = middle/thick clouds and Obs. (196) $_{grey}$ = thick clouds or non-cloudy scenes.

4.4.5 Case No. 5: RE with albedo = 0.7 (W08P61O64/116/196/238)

In this case, we increase albedo from 0.5 to 0.7. The observation numbers 64 and 238 within 1100 to 1300 nm spectral bands and around 1450 nm band only agrees with the synthetic model for detecting low or middle cloud layers. Consequently, observation number 116 is a candidate for thick clouds, as illustrated in Figure 4.22. The results are shown in Table 4.12.

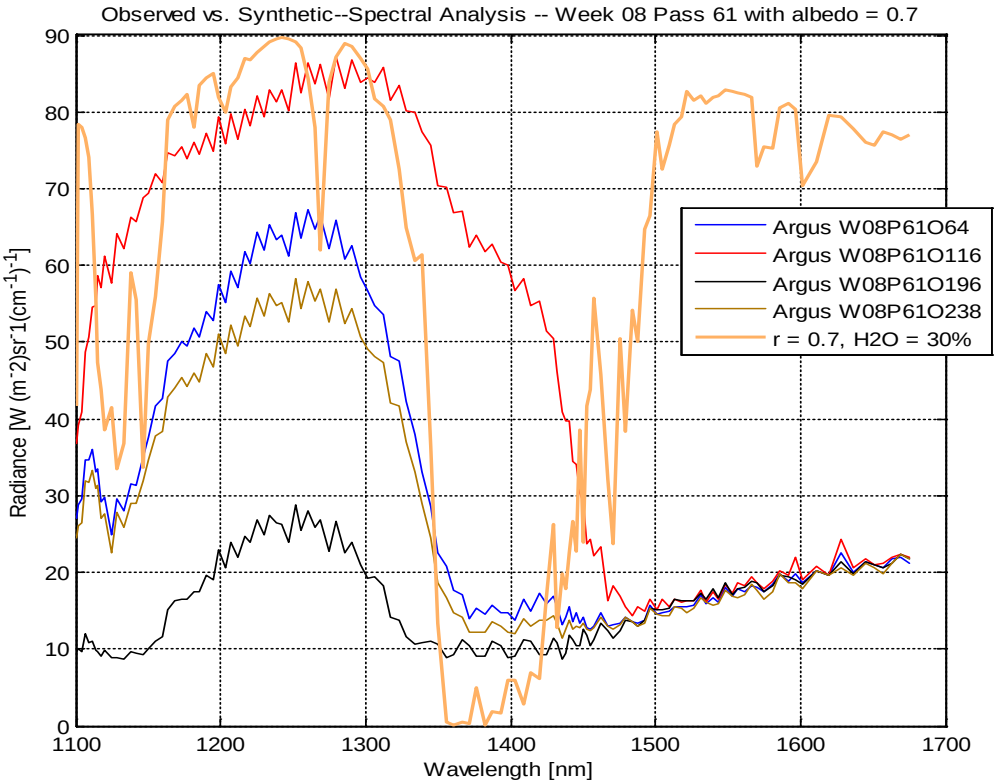

Fig. 4.22. RE model: Argus spectra (observed) of week 08 pass 61 with different observations number 64/116/196/238 vs. GENSPECT model spectra (synthetic) with (r=0.7, H_2O = 30%).

Table 4.12. RE & CRE of week 08 pass 61 with observations 64/116/196/238, albedo = 0.7

Week/Pass/Obs.	RE1	RE2	RE3	RE4	CRE1	CRE2	CRE3	Types of cloud
08/61/64	-0.325817	0.889781	-0.701545	-0.755222	-0.823079	-0.366177	-0.892803	middle/thin
08/61/116	-0.0504042	5.46447	-0.553336	-0.747347	-6.84985	-0.00922398	4.11339	thick
08/61/196	-0.750985	0.0961294	-0.724882	-0.753891	-0.063878	-7.81223	-2.13363	no/thick
08/61/238	-0.40588	0.605287	-0.711627	-0.760677	-0.518865	-0.670559	-1.2729	middle/low

Obs. (116) $_{red}$ = Thick clouds, Obs. (64) $_{blue}$ = middle/thin clouds, Obs. (238) $_{green}$ = middle/thick clouds and Obs. (196) $_{grey}$ = thick clouds or non-cloudy scenes.

4.4.6 Case No. 6: RE with albedo = 0.1 (W14P52O22/100/120/124)

Figure 4.23, shows a comparative plot of synthetic spectra (r = 0.1, H_2O = 30%, bold pink color) with each of the four-selected observed spectrum of week 14 pass 52 in the set. Only observation number 120 shows a good agreement with synthetic model when albedo is equal to 0.1, suggesting low cloud or non-cloudy scene. Observation number 22 also agrees between 1500 to 1675 nm (CO_2 and CH_4 wavelength bands). The calculated RE's and CRE's values for all the selected observation numbers are given in Table 4.13, show the high radiance ratios as compared with synthetic model. It is found that the observation number 124 has high radiance enhancement and is the best candidate for a scene with high or middle cloud layers. Observation numbers 22 and 100 also show high RE's and CRE's values in most of the selected wavelength bands, suggesting a middle cloud or low cloudy scene respectively.

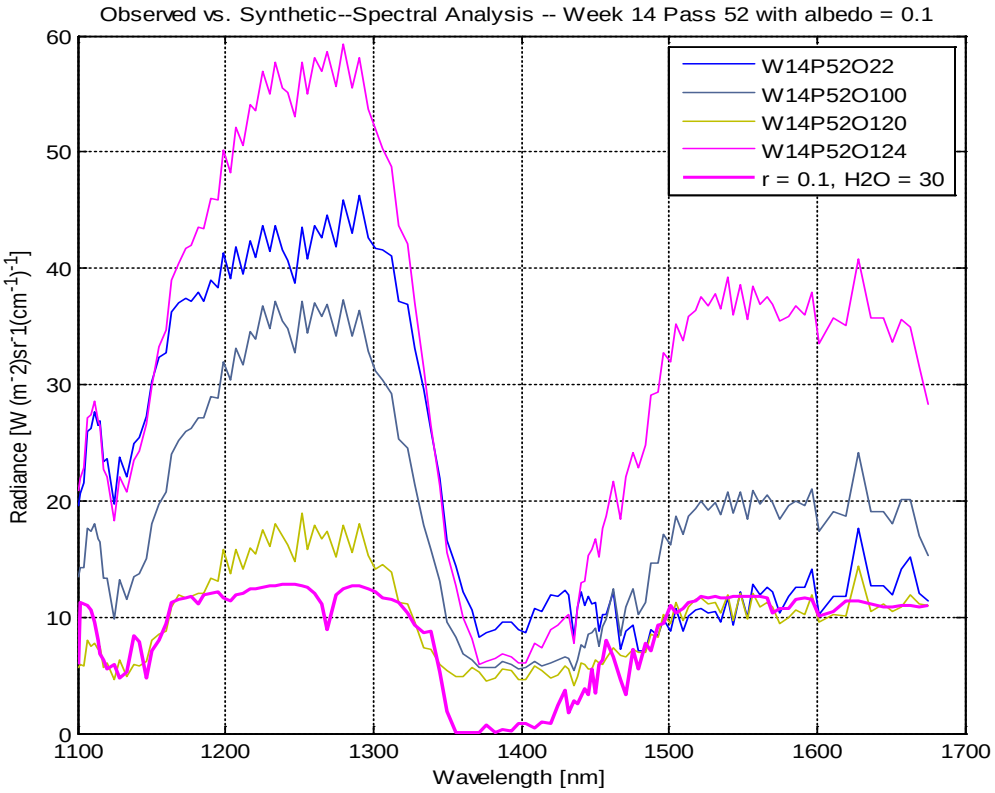

Fig. 4.23. RE model: Argus spectra (observed) of week 14 pass 52 with different observations number 22/100/120/124 vs. GENSPECT model spectra (synthetic) with (r=0.1, H_2O = 30%).

Table 4.13. RE & CRE of week 14 pass 52 with observations 22/100/120/124, albedo = 0.1

Week/Pass/Obs.	RE1	RE2	RE3	RE4	CRE1	CRE2	CRE3	Types of cloud
14/52/22	2.34289	7.76578	0.443422	0.0899136	3.19211	0.301694	10.6420	Thick/middle
14/52/100	1.54716	4.53176	0.804702	0.730737	1.98945	0.341404	7.61436	Thin/no/thick
14/52/120	0.175152	3.08311	0.12536	-0.0285374	21.0286	0.0568103	3.35508	No/thin
14/52/124	3.0557	6.47487	2.51549	2.20498	1.23081	0.471932	14.2510	Thick/middle

Obs. (124) $_{blue}$ = Thick/middle clouds, Obs. (22) $_{blue}$ = Thick/middle clouds, Obs. (100) $_{grey}$ = Thin/no/thick clouds and Obs. (120) $_{grey}$ = low clouds or non-cloudy scenes.

4.4.7 Case No. 7: RE with albedo = 0.3 (W14P52O22/100/120/124)

Figure 4.24 illustrates the effect of increasing the surface albedo to 0.3 and H_2O concentration to 30%. Observation 100 and 22 show good agreement with synthetic model within 1100 to 1480 nm and 1430 to 1675 nm wavelength bands. These two observations numbers also agree with the case 6 for middle or thick cloud scenes. The calculated RE's and CRE's values for all the selected observation numbers are shown in Table 4.14, suggesting thick or middle clouds specially for the observation number 124.

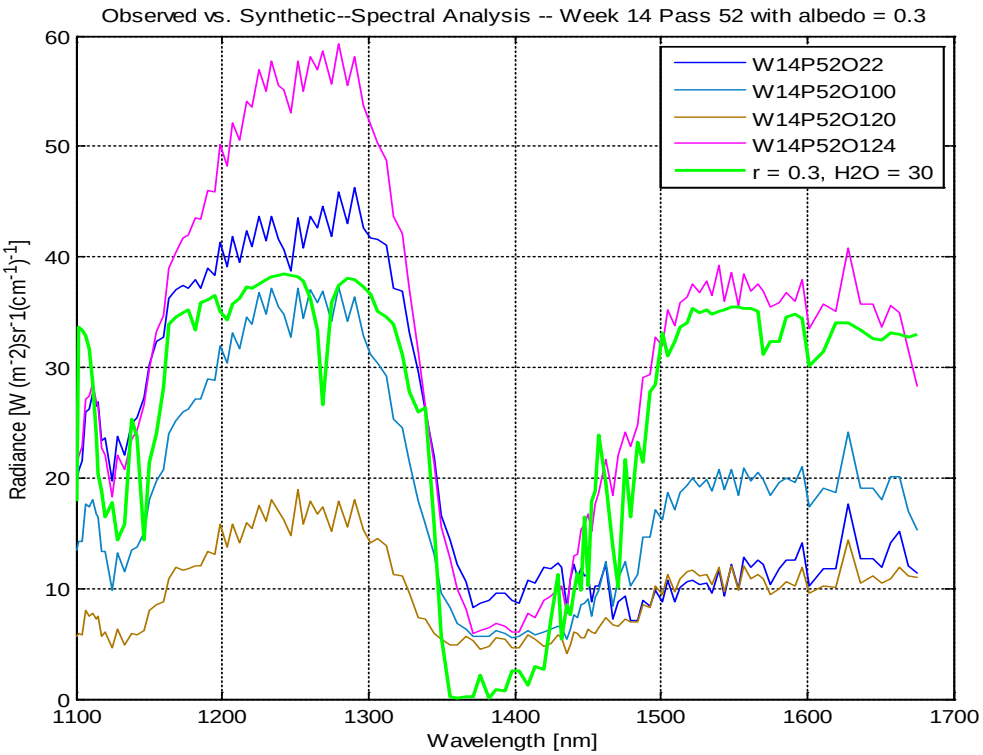

Fig. 4.24. RE model: Argus spectra (observed) of week 14 pass 52 with different observations number 22/100/120/124 vs. GENSPECT model spectra (synthetic) with (r=0.3, H_2O = 30%).

Table 4.14. RE & CRE of week 14 pass 52 with observations 22/100/120/124, albedo = 0.3

Week/Pass/Obs.	RE1	RE2	RE3	RE4	CRE1	CRE2	CRE3	Types of cloud
14/52/22	0.114297	1.92193	-0.518859	-0.636695	-3.67905	0.0594702	0.880671	Thick/middle
14/52/100	-0.150946	0.84392	-0.398433	-0.423088	-1.47016	-0.178863	-0.128546	Thin/No/thick
14/52/120	-0.608283	0.361035	-0.62488	-0.676179	-0.281079	-1.68483	-1.54831	No/thin
14/52/124	0.3519	1.49162	0.17183	0.0683261	3.54958	0.235917	2.08368	Thick/middle

Obs. (124) $_{blue}$ = Thick/middle clouds, Obs. (22) $_{blue}$ = Thick/middle clouds, Obs. (100) $_{grey}$ = Thin/no/thick clouds and Obs. (120) $_{grey}$ = low clouds or non-cloudy scenes.

4.4.8 Case No. 8: RE with albedo = 0.1, 0.25 (W75P43O19/30/43/65)

Figure 4.25 and Figure 4.26 show a comparative plot of synthetic spectra (r = 0.1 and 0.25, H_2O = 30%) with each of the four-selected observed spectrum of week 75 pass 43 in the set. In this case, the absolute radiance profile of the selected four observation numbers show less radiance as compared to previous selected observed spectra. Only observation number 65 shows a high absolute radiance as compared to the other three selected observation numbers and can be a candidate for middle or thin clouds. The calculated RE's and CRE's values as shown in Table 4.15 and Table 4.16, for observation numbers 19, 30 and 43, suggesting a candidate for non-cloudy scene.

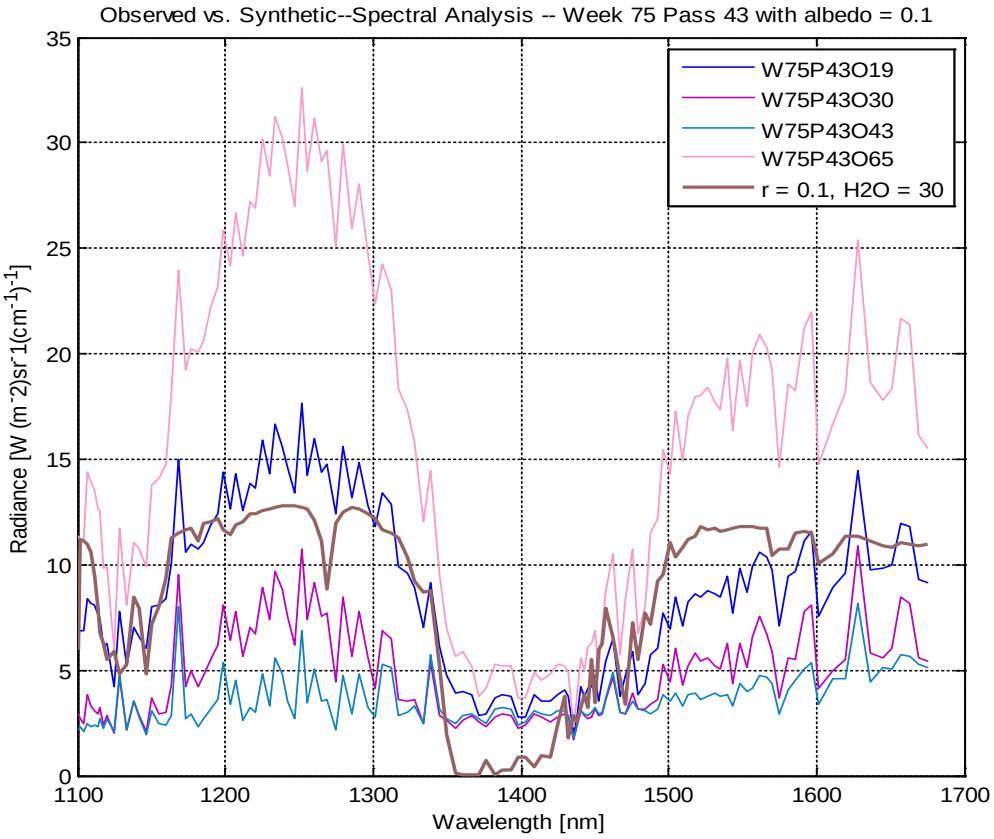

Fig. 4.25. RE model: Argus spectra (observed) of week 75 pass 43 with different observations number 19/30/43/65 vs. GENSPECT model spectra (synthetic) with (r=0.1, H_2O = 30%).

Table 4.15. RE & CRE of week 75 pass 43 with observations 19/30/43/65, albedo = 0.1

Week/Pass/Obs.	RE1	RE2	RE3	RE4	CRE1	CRE2	CRE3	Types of cloud
75/43/19	0.0900261	1.93735	-0.183703	-0.122302	-60.0253	0.0464686	1.72138	no
75/43/30	-0.455174	1.04854	-0.452621	-0.448411	-1.16042	-0.434102	-0.307664	no
75/43/43	-0.681497	1.12676	-0.506737	-0.585169	-0.88955	-0.604827	-0.64664	no
75/43/65	1.03648	3.27451	0.469704	0.676306	1.9118	0.31653	5.45700	middle/thick

Obs. (65) $_{orange}$ = middle/thick clouds and Obs. (19, 30, 43) $_{grey}$ = non-cloudy scenes.

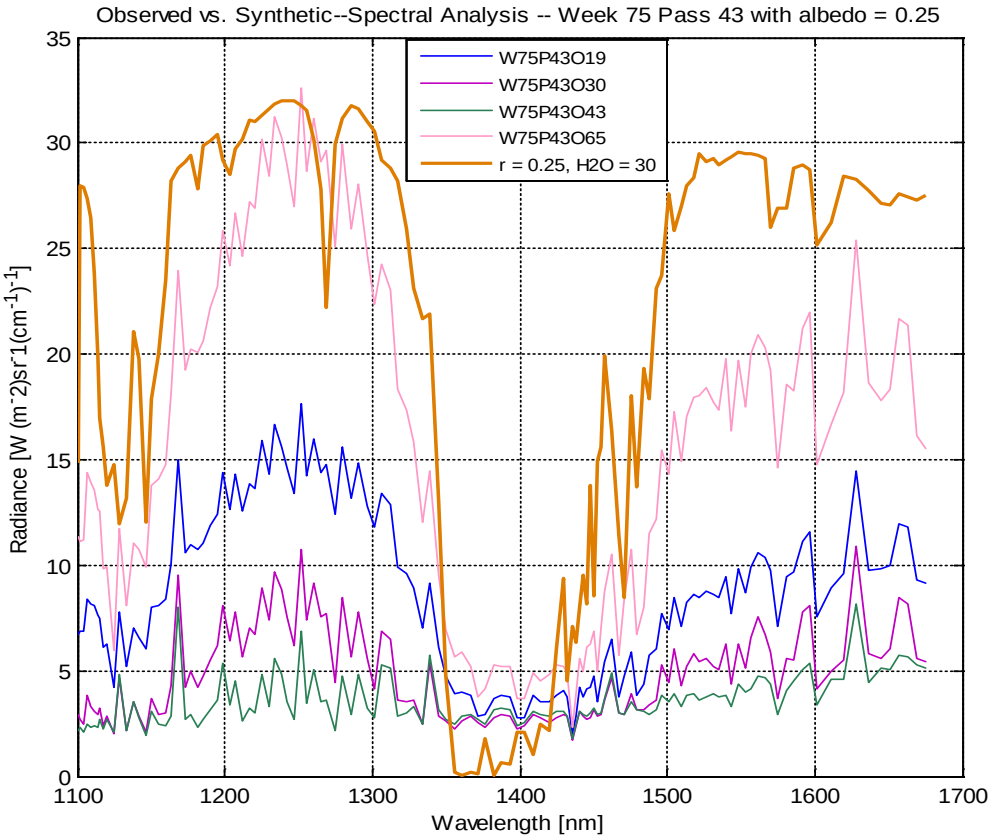

Fig. 4.26. RE model: Argus spectra (observed) of week 75 pass 43 with different observations number 19/30/43/65 vs. GENSPECT model spectra (synthetic) with (r = 0.25, H_2O = 30%).

Table 4.16. RE & CRE of week 75 pass 43 with observations 19/30/43/65, albedo = 0.25

Week/Pass/Obs.	RE1	RE2	RE3	RE4	CRE1	CRE2	CRE3	Types of cloud
75/43/19	-0.56399	0.174941	-0.673481	-0.648921	-0.144233	-3.22388	-1.71145	no
75/43/30	-0.782069	-0.180584	-0.781048	-0.779364	0.115653	4.33078	-2.52307	no
75/43/43	-0.872599	-0.149295	-0.802695	-0.834068	0.0874774	5.84481	-2.65866	no
75/43/65	-0.185408	0.709805	-0.412118	-0.329478	-1.37857	-0.261209	-0.217198	middle/thin

Obs. (65) $_{orange}$ = middle/thin clouds and Obs. (19, 30, 43) $_{grey}$ = non-cloudy scenes.

4.5 RE - Clouds Optimization Results

The comparison between Argus real and synthetic data is automated using lsqcal.m and lasqtest.m scripts as introduced in section 4.1.2. The code optimizes Argus data fitting comparing the generated values from the synthetic models to the calibrated Argus spectrum in order to determine a match over a set of wavelength bands. As mentioned earlier, we used the method of optimal retrievals by means of forward model to optimize the synthetic model by adjusting the parameters. Any optimization technique by means of retrieval method computationally difficult and will always yield no-zero error margin as no technique completely captures the complex behavior of the atmosphere [Rayner, P., et al., 2009]. Due to the very complex structure of clouds and its water absorption mechanism, most of the methods developed for the analysis of cloud scenes from satellite measurements are highly sensitive to the model parameters [Stephens, G.L., et al., 2007]. As discussed in section 4.3 and 4.4, we fixed some parameters specially O_2, CH_4, type of surface (Lambertian) and scattering type (Rayleigh). The parameters such as the gas mixing ratio profile specially H_2O and CO_2, solar zenith (Sun) angle, viewing (nadir) angle, surface to atmospheric height are adjusted until the closest match between the synthetic and observed radiance profiles is achieved. The solar zenith angle and nadir angle are different of each week per pass per observation number. We use the average of the solar zenith and sun angle, which corresponds to the specific date and time of the Argus observation number for the selected week per pass. The optimization process is computationally expensive if the number of variable parameters are too large. The selected model parameters are now optimized to achieve best fit retrieval results in order to categorize the different types of clouds. As discussed in section 4.2 and 4.3, we estimated

the radiance value in terms Wm^{-2} sr^{-1} $(1/cm)^{-1,}$ RE, and CRE for the detection of cloud scenes. Using solar radiation intensity and the radiance enhancement ratios flight data collected by Argus 1000 spectrometer is categorized into high, medium, low and no cloud scenes. For all the optimized results as shown in Figure 4.27 through 4.33, fitting over all wavelength bands of Argus spectral window, we find a good match between synthetic model observation. The Argus spectral candidates for high, medium, low, and no cloud scenes are describing in the following section:

Argus – Thin or thick cloud scenes (red color spectra): Figures 4.27 (a) and 4.28(a) show a comparison between synthetic (model) and observed radiance are the best candidates for high cloud scenes. The observed radiance profile was collected on October 30, 2009 at latitude 6° 30' 22.36" N, longitude 60° 57' 43.92" E and at latitude 4° 16' 5.16" S, longitude 58° 44' 51.36" E respectively. The CO_2 mixing ratio concentration was decreased by 7% and 9% of its value in the model which is 360 ppm for both the figures respectively. H_2O concentration was set as 30% (spectral saturation, as discussed in previous section) introduces 10% spectral fitting error within this band. O_2 and CH_4 remains the same as US atmospheric model 1976. Both the comparisons agree with the estimated results of case number 4 (section 4.4.4) with albedo is equal to 0.5 and 0.6. We found a good match between theory and observations in both cases, especially from 1120 to 1480 nm of wavelength bands. For the O_2 feature near around 1230 to 1260 nm, we only see the approximate match. The main reason is the O_2 is filled in by the ring effect due to the solar Fraunhofer lines in the spectra of scattered sun light compared to direct sun light observations [Wagner, T. et al., 2010]. There few other reasons for this error are (i) signal-to-noise ratio performance are not well calibrated for O_2 absorption peak (ii) line mixing in the dense

structure of O_2 band (collision tempted absorption) (iii) integration time setting of instruments may vary with case by case. In H_2O region, near 1350 to 1450 nm, it is very difficult to match in this wavelength band due to the complex structure of variation in water vapor contents, especially in all the region of vertical and horizontal of H_2O. Similarly, for CO_2 absorption bands from 1570 to 1620 nm, we cannot exactly fit our data, because the atmospheric absorption path is no longer enough in the presence of any reflective medium or in a case of thin or thick clouds at altitudes 10 km and 4 km as shown in Fig 4.27 (a) and Fig 4.28 (a) respectively. In both the cases photons will experience low absorption within CO_2 region. In view of all the above errors, the week 08 pass 61with observation numbers 64 and 238 may have introduced around ± 9 Wm^{-2} sr^{-1} $(1/cm)^{-1}$ and ± 10 Wm^{-2} sr^{-1} $(1/cm)^{-1}$ residual errors within the full spectral wavelength band of Argus 1000 as shown in Figure 4.27 (b) and Figure 4.28 (b) respectively.

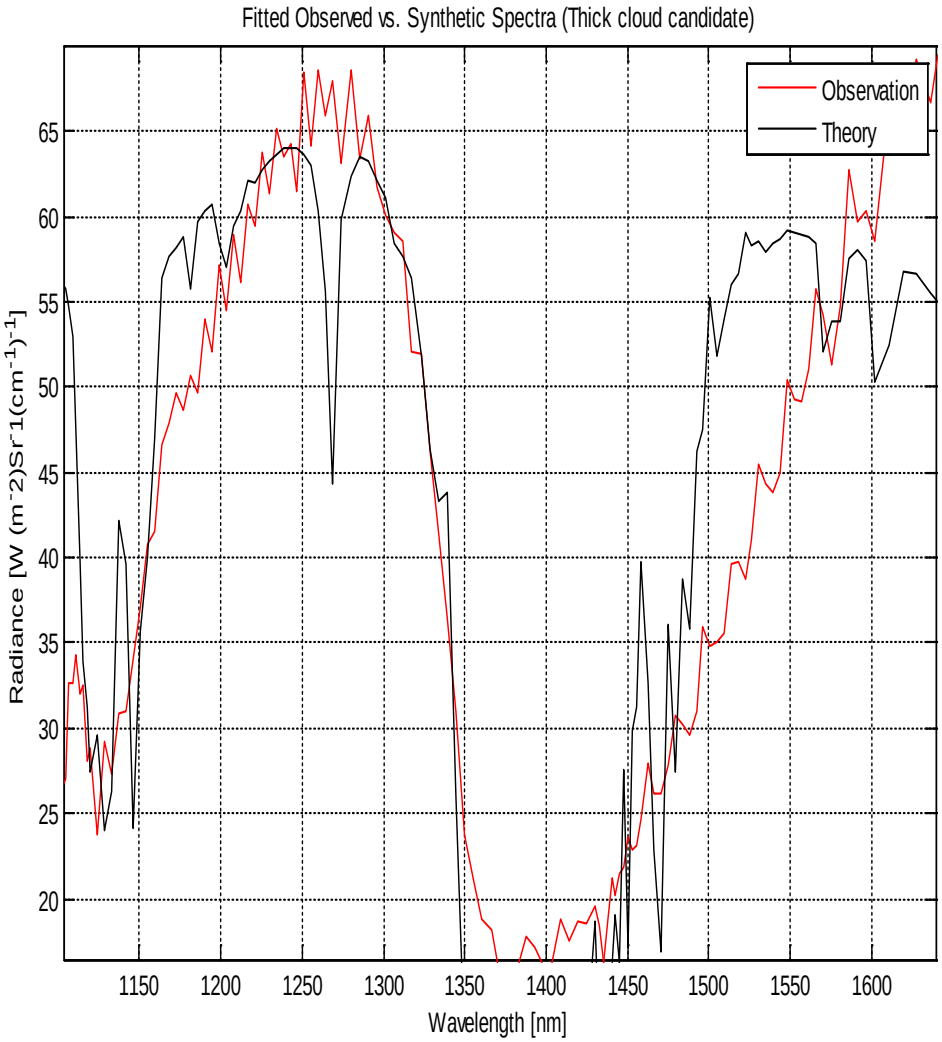

Fig. 4.27 (a). Argus spectral optimization with reference synthetic spectra for cloud classification (week 08 pass 61 observation number 64: albedo = 0.5, H_2O = 30%, altitude = 10km).

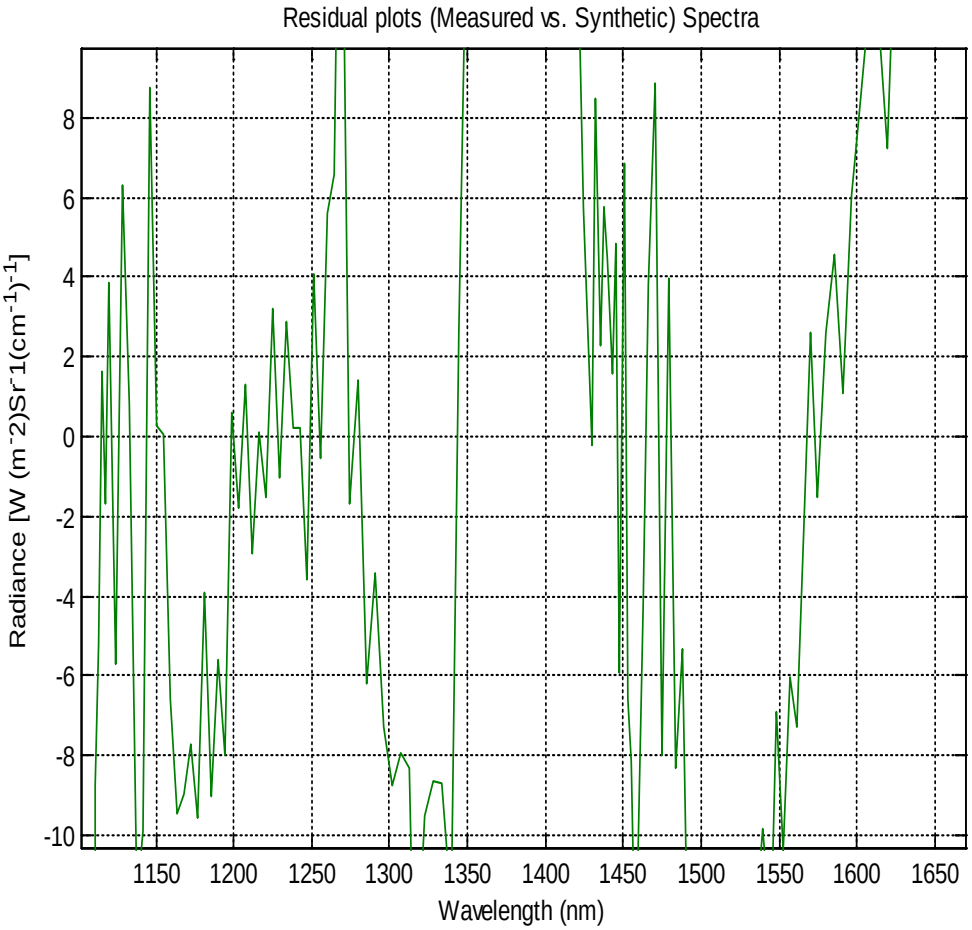

Fig. 4.27 (b). Argus spectral optimization ± 9 (Wm^{-2} sr^{-1} $(1/cm)^{-1}$) residual error within Argus 1000 wavelength band (week 08 pass 61 observation number 64).

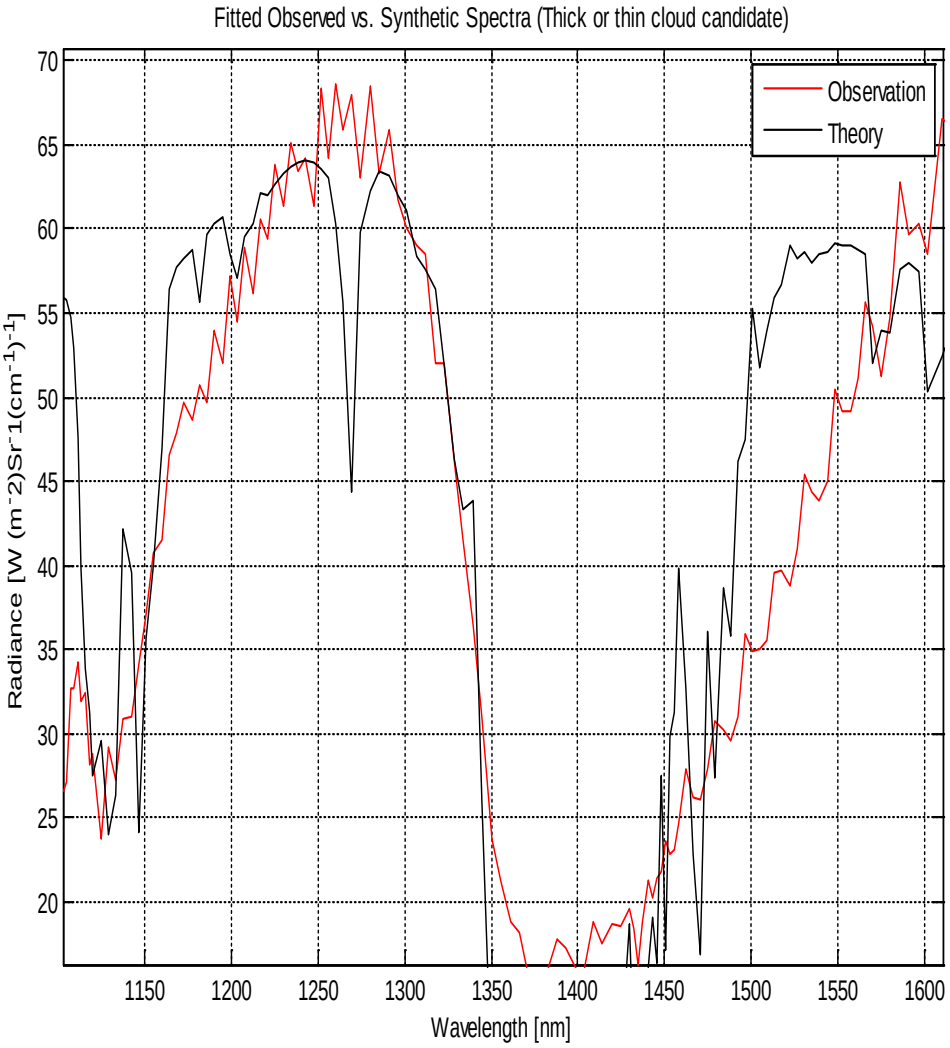

Fig. 4.28 (a). Argus spectral optimization with reference synthetic spectra for cloud classification (week 08 pass 61 observation number 238: albedo = 0.5, H_2O = 30%, altitude = 4km).

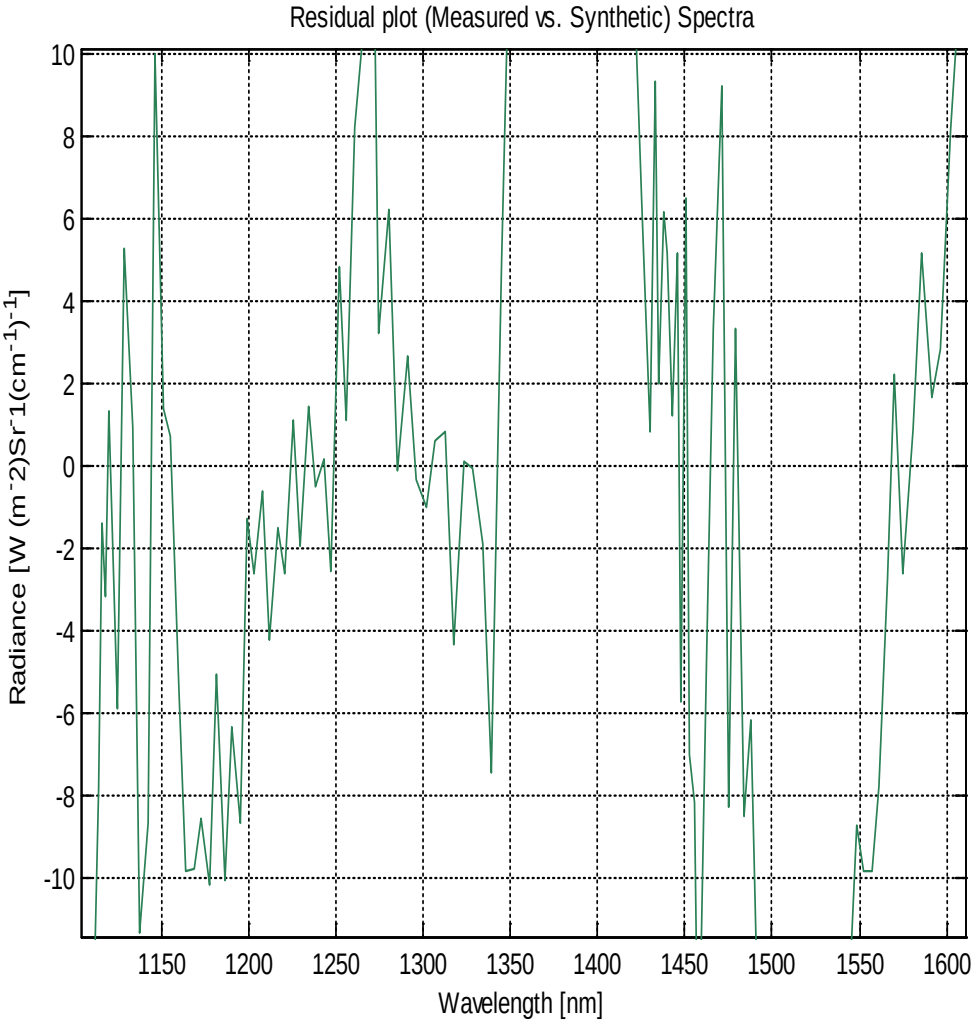

Fig. 4.28 (b). Argus spectral optimization ± 10 (Wm^{-2} sr^{-1} $(1/cm)^{-1}$) residual error within Argus 1000 wavelength band (week 08 pass 61 observation number 238).

Figure 4.29 (a) also shows the best candidates for thick or thin cloud scenes while comparing synthetic and observed radiance profile. The observed radiance profile was collected on March 04, 2010 at latitude 42° 17' 21.48" N and longitude 79° 56' 43.08" W. The observation number of this Argus flight gives an excellent match between theory and model within full spectral window. The retrieved CO_2 mixing ratio concentration was found to be approximately same by increasing 9% of its value in the model. This gives a CO_2 concentration of 392.4 ppm which is the same value recorded by the National Oceanic and Atmospheric Administration (NOAA) on March 04, 2010. The optimized albedo is the same as 0.5 with H_2O mixing ratio concentration is the same as discussed in the previous section. In this case, the week 14 pass 52 with observation number 124 may have introduced around ± 5 Wm^{-2} sr^{-1} $(1/cm)^{-1}$ residual errors within the full spectral wavelength band of Argus 1000 as shown in Figure 4.29 (b). This is one of the best-case scenario for detecting the thick cloud scenes. All the three results show maximum radiance profile approximately 68 Wm^{-2} sr^{-1} $(1/cm)^{-1}$ for high cloud scenes with adjusted albedo is 0.5.

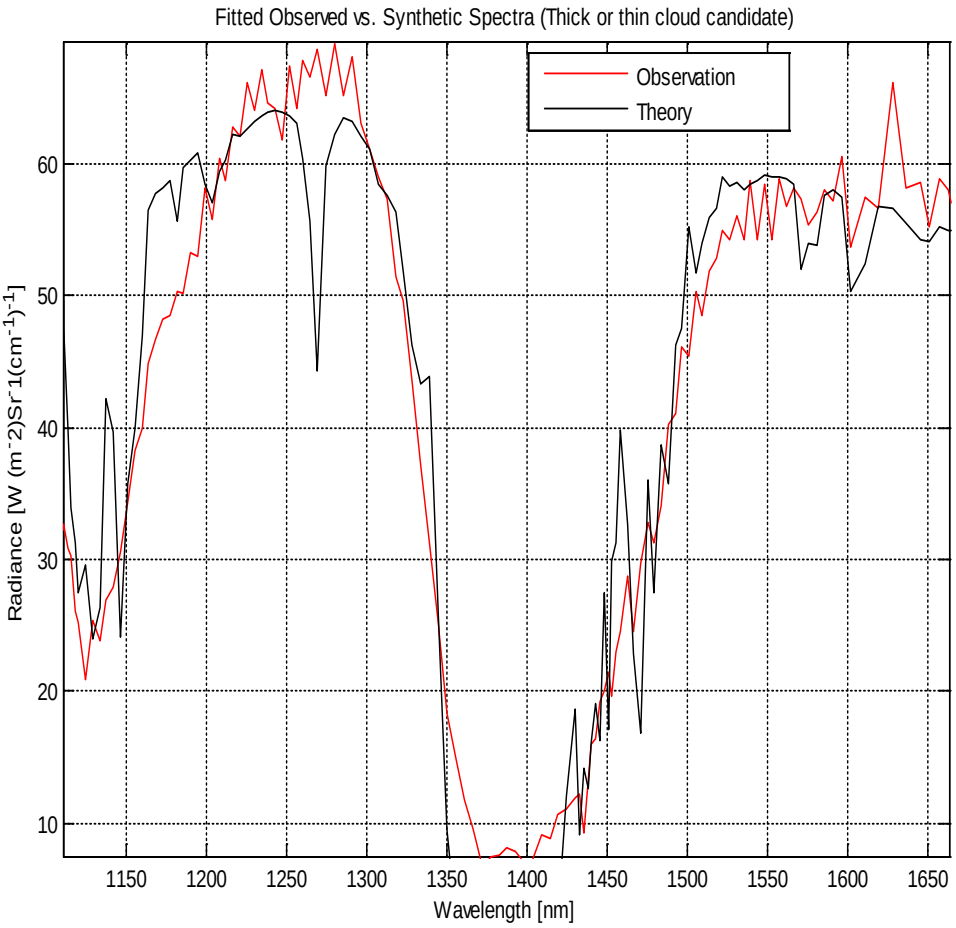

Fig. 4.29 (a). Argus spectral optimization with reference synthetic spectra for cloud classification (week 14 pass 52 observation number 124: albedo = 0.50, H_2O = 30%, altitude = 6km).

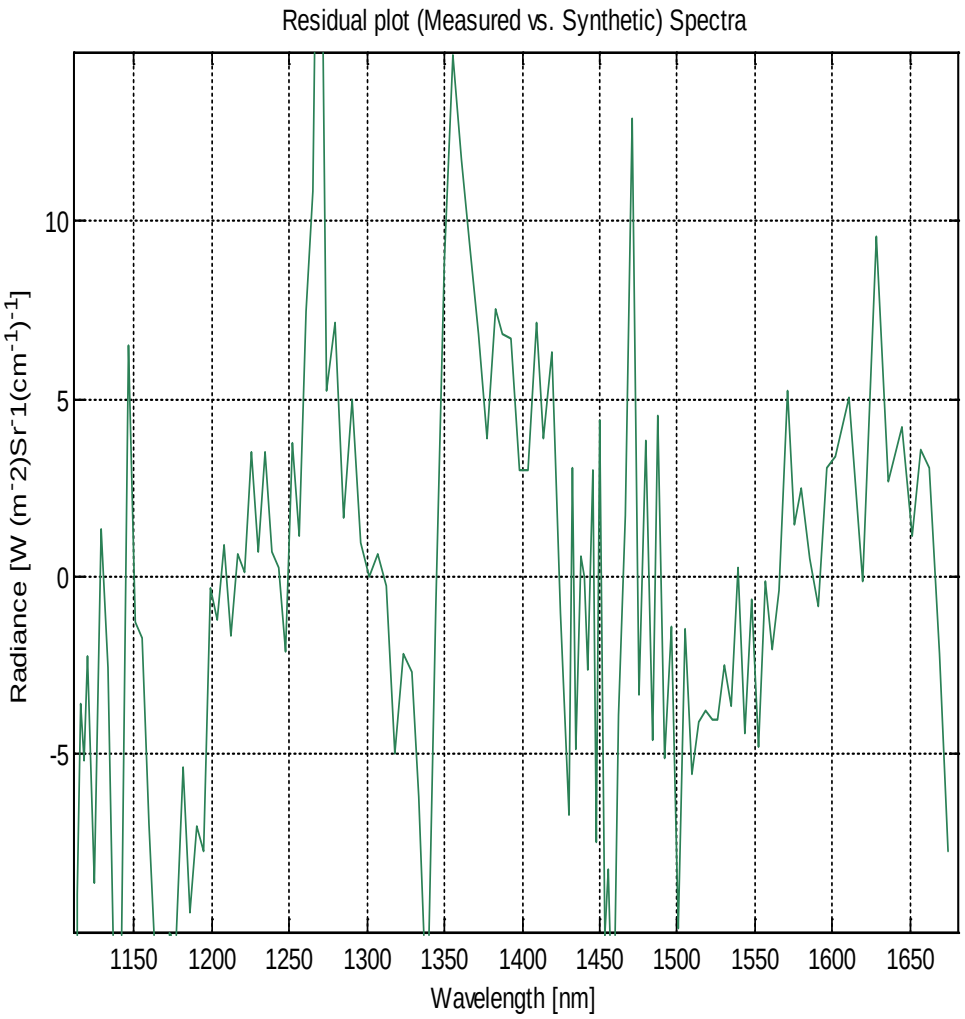

Fig. 4.29 (b). Argus spectral optimization ± 5 (Wm^{-2} sr^{-1} $(1/cm)^{-1}$) residual error within Argus 1000 wavelength band (week 14 pass 52 observation number 124).

Argus - medium/thick (low) clouds (orange color spectra): Figure 4.30 (a) and Figure 4.31 show a comparison between synthetic (theory) and the selected observed radiance are the best candidates (only from week 14 pass 52 and week 75 pass 43) for medium or thick cloud scenes. The observed radiance profile was collected on March 04, 2010 at latitude 42° 50' 28.68" N, longitude 79° 43' 8.04" W (observation number 100) and August 14, 2013 at latitude 19° 55' 28.56" N and longitude 145° 32' 53.16" E (observation number 65) respectively. The CO_2 mixing ratio concentration was increased by 10% for both the observation numbers of its value in the model which is 360 ppm. This yields a CO_2 concentration of approximately 396 ppm which is the same value recorded by the NOAA on August 2013. For CO_2 absorption bands from 1570 to 1620 nm, we almost fit our data specially for two prominent absorption peaks of CO_2 at 1560 nm and 1600 nm. In this case, increasing the CO_2 atmospheric concentration which reducing the H_2O radiance profile within the full spectral range. We found less albedo (0.2 to 0.25) consequently show perturbed photons count due to H_2O and CO_2 absorption features. In this case, only 3% fitting error may have introduced within full spectral region. In this case, the week 14 pass 52 with observation number 100 may have introduced around ± 4 Wm^{-2} sr^{-1} $(1/cm)^{-1}$ residual errors within the full spectral wavelength band (specially between 1100 to 1200 nm and 1550 to 1620 nm) of Argus 1000 as shown in Figure 4.29 (b). These two examples are good for detecting the middle or low-level cloud scenes. Both the spectra show maximum radiance profile approximately 35 Wm^{-2} sr^{-1} $(1/cm)^{-1}$ for middle/low cloud scenes with adjusted albedo is 0.25. The results are also agreed with the mean value of the estimated radiance of cloud height as discussed in section 4.2.4.

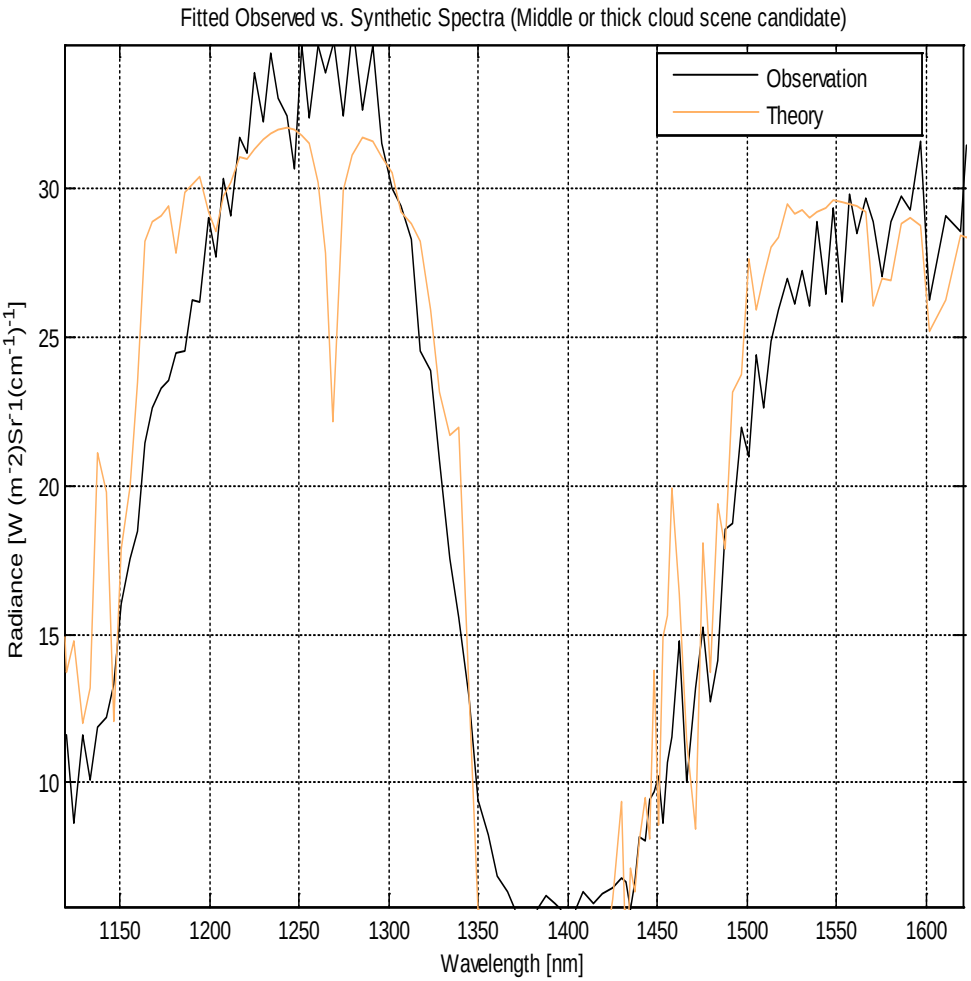

Fig. 4.30 (a). Argus spectral optimization with reference synthetic spectra for cloud classification (week 14 pass 52 observation number 100: albedo = 0.25, H_2O = 30%, altitude = 5km).

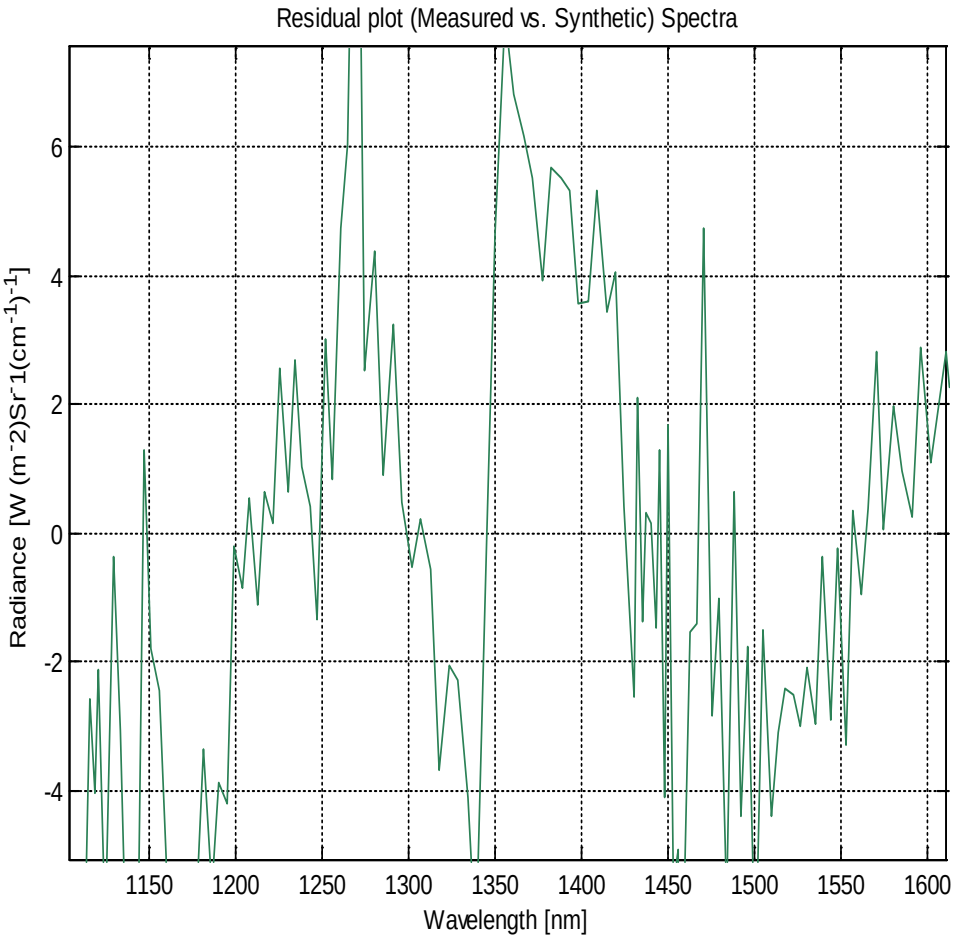

Fig. 4.30 (b). Argus spectral optimization ± 4 (Wm^{-2} sr^{-1} $(1/cm)^{-1}$) residual error within Argus 1000 wavelength band (week 14 pass 52 observation number 100).

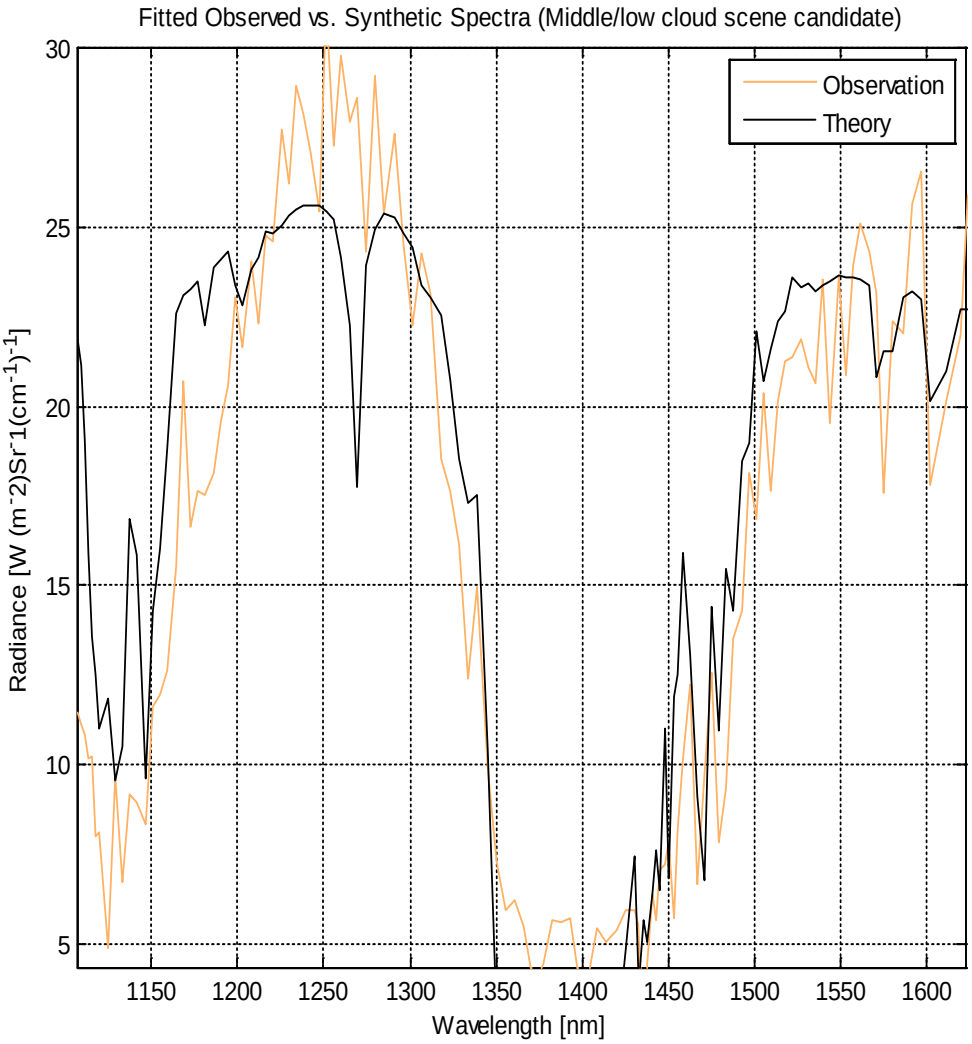

Fig. 4.31. Argus spectral optimization with reference synthetic spectra for cloud classification (week 75 pass 43 observation number 65: albedo = 0.20, H_2O = 30%, altitude = 5km).

Argus – no-cloud scene (bold grey spectra): Figure 4.32 (a) and Figure 4.33 show a comparison between synthetic (theory) and the selected observed radiance are the best candidates (only from week 14 pass 52 and week 75 pass 43) for clear sky or no-cloud scenes. The observed radiance profile was collected on March 04, 2010 at latitude 42° 50' 28.79" N, longitude 79° 43' 8.13" W (observation number 120) and August 14, 2013 at latitude 31° 45' 33.12" N and longitude 148° 12' 48.6" E (observation number 19)

respectively. The CO_2 mixing ratio concentration was increased by 15% and the concentration of water vapor was reduced by 40% (by US atmospheric model). In this case, our hypothesis is that there is no multiple scattering due to clouds and aerosols in the surrounding atmospheric layers. The albedo is from 0.05 to 0.1, giving high probability of no cloud scenes. In this case, 12% fitting error within CO_2 and H_2O region is introduced. These are the good candidates for clear sky or no-cloud scenes. In this case, the week 75 pass 43 with observation number 19 may have introduced around ± 2 Wm^{-2} sr^{-1} $(1/cm)^{-1}$ residual error within the full spectral wavelength band of Argus 1000 as shown in Figure 4.33 (b). Both the Argus spectra show a maximum radiance profile of approximately 14 Wm^{-2} sr^{-1} $(1/cm)^{-1}$ for no cloud scenes with adjusted albedo is 0.1.

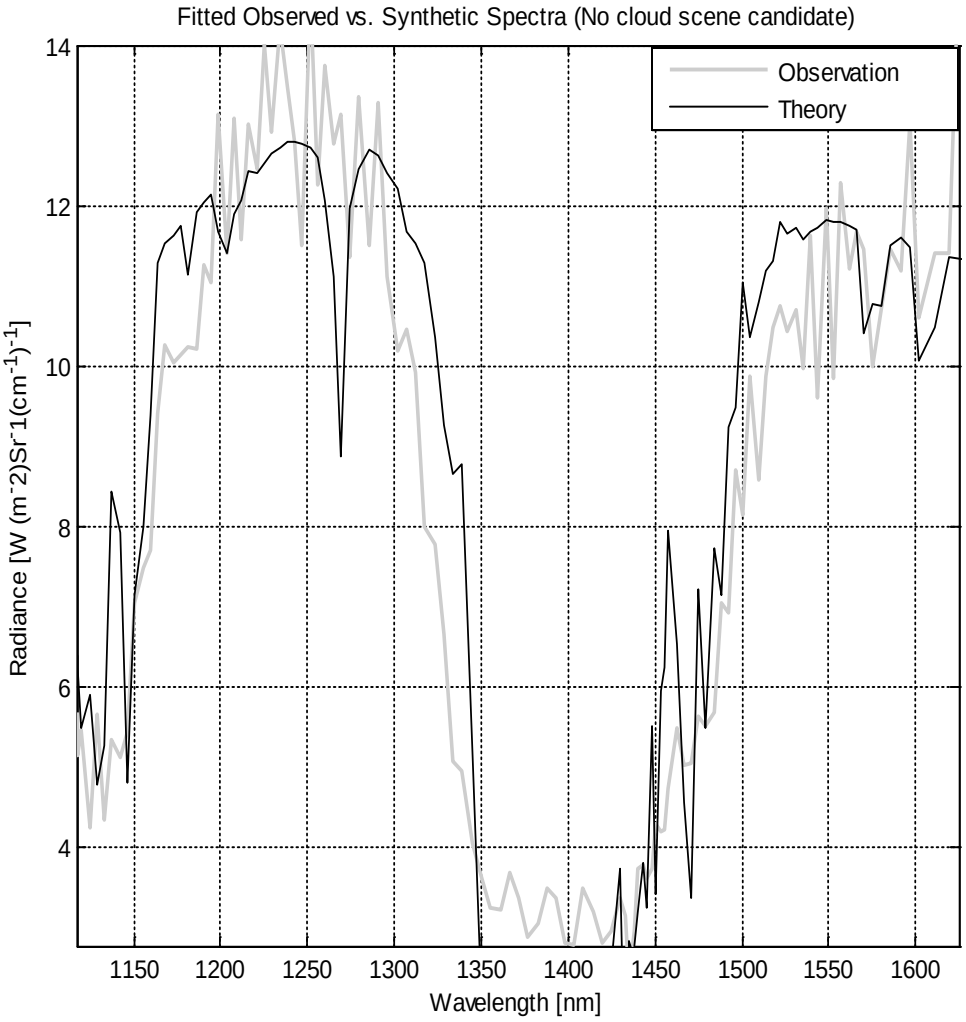

Fig. 4.32. Argus spectral optimization with reference synthetic spectra for cloud classification (week 14 pass 52 observation number 120: albedo = 0.1, H_2O = 40%, altitude = 5km).

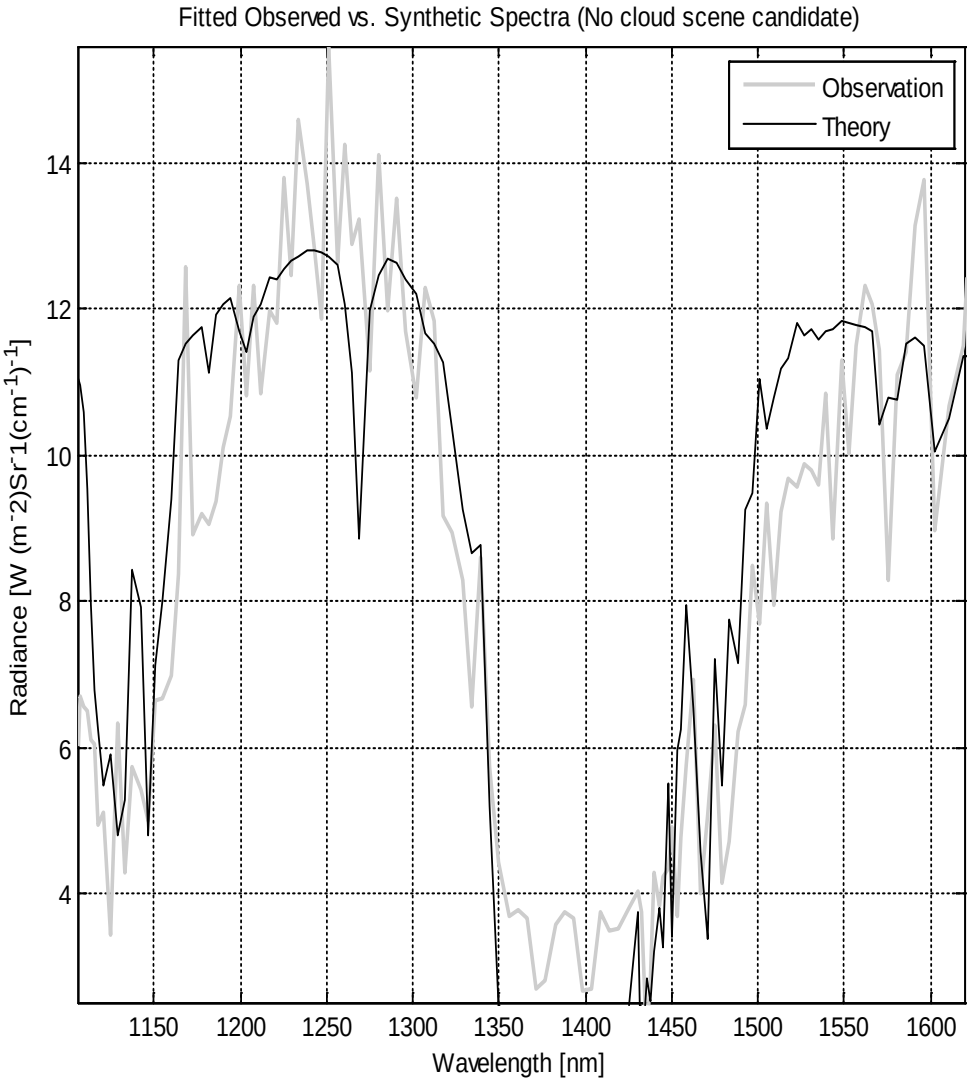

Fig. 4.33 (a). Argus spectral optimization with reference synthetic spectra for cloud classification (week 75 pass 43 observation number 19: albedo = 0.1, H_2O = 30%, altitude = 2km).

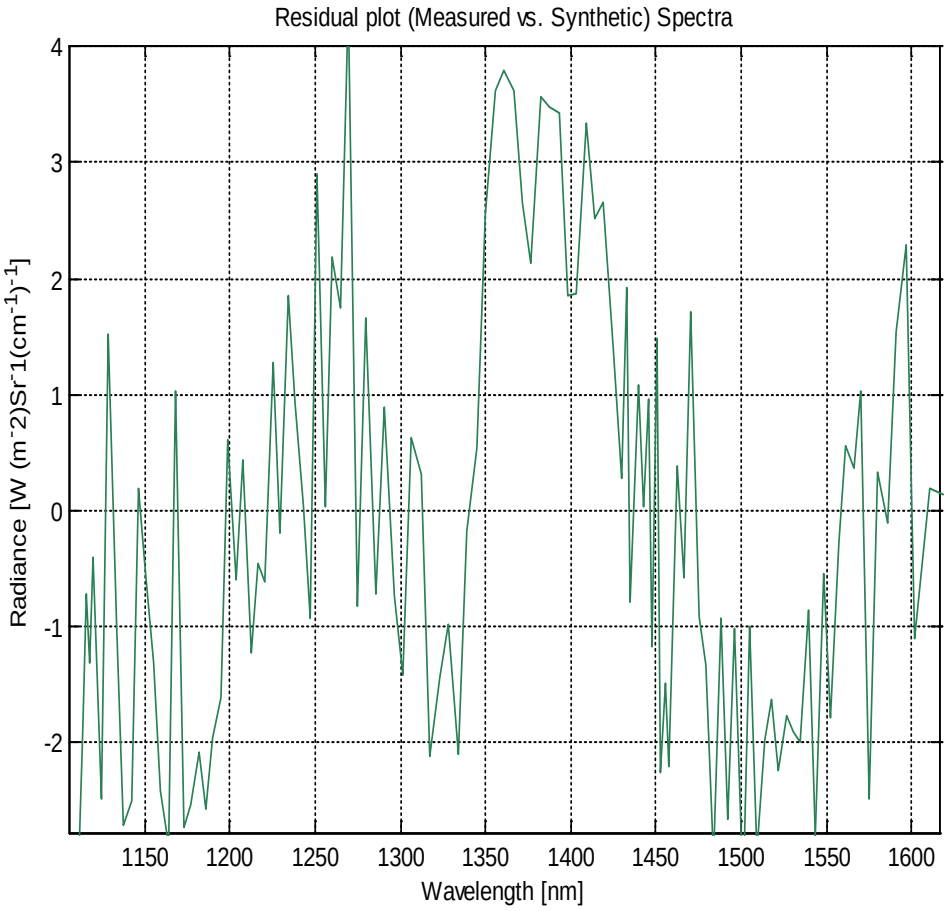

Fig. 4.33 (b). Argus spectral optimization ± 2 (Wm^{-2} sr^{-1} $(1/cm)^{-1}$) residual error within Argus 1000 wavelength band (week 75 pass 43 observation number 19).

Over all the RE results and optimization scenarios with their residuals, our results from the space-orbiting Argus 1000 (spectral wavelength range from 1100 to 1700 nm) show very good agreement with our cloud radiation model. We believe this is the first ever experimental techniques to demonstrate high quality of fitting of radiance scenes in the presence of clouds. While we have noted some model disagreements in our examples caused by input value assumptions, the GENSPECT-Synthetic model provides a good estimation to evaluate the cloud scene retrieval methods within this important window. While there are many other errors introduced in any of the retrieval methodology,

especially because of the complex atmospheric structure of water vapor regions, multiple scattering within atmospheric clouds and aerosols, instrument calibration error (in terms of joules per counts), limited instrument spectral resolution, modeling errors, optimizing errors, and some errors due to inhomogeneity of albedo and other estimated quantities of the model is apparently adaptable to describe a wide variety of real-world observation scenes in the presence of clouds. The cloud height is not validated with the other models, its only compared with the model estimated values by optimization technique.

4.6 Uncertainties

All remote sensing satellite observations are subject to a core set of uncertainties. In this section, we quantify the most significant sources of errors.

4.6.1 Geolocation uncertainties

There are two geolocation uncertainties, that have been estimated: the along-track error and the cross-track error [Jagpal R.K., 2011; Chesser H., et al., 2012]. These are estimated to be 33.4 km along-track and 12.8 km cross-track as shown in Table 4.17.

Table 4.17. Geolocation uncertainties for Argus micro-spectrometer data at a 3.8° nadir angle

Cause of Uncertainty	Earth Central Angle Uncertainty in Along-Track Direction (mrad)	Earth Central Angle Uncertainty in Cross-Track Direction (mrad)
Attitude Determination	1.7	1.7
NORAD TLE	0.3	0.3
Onboard Timing System	3.2	0
Total	5.2	2.0

Figure 4.34 illustrates the nadir angle of approximately 4.7° throughout the observation made on March 11, 2009 between 11:46 and 11:59 UTC [Siddiqui R. et al., 2015].

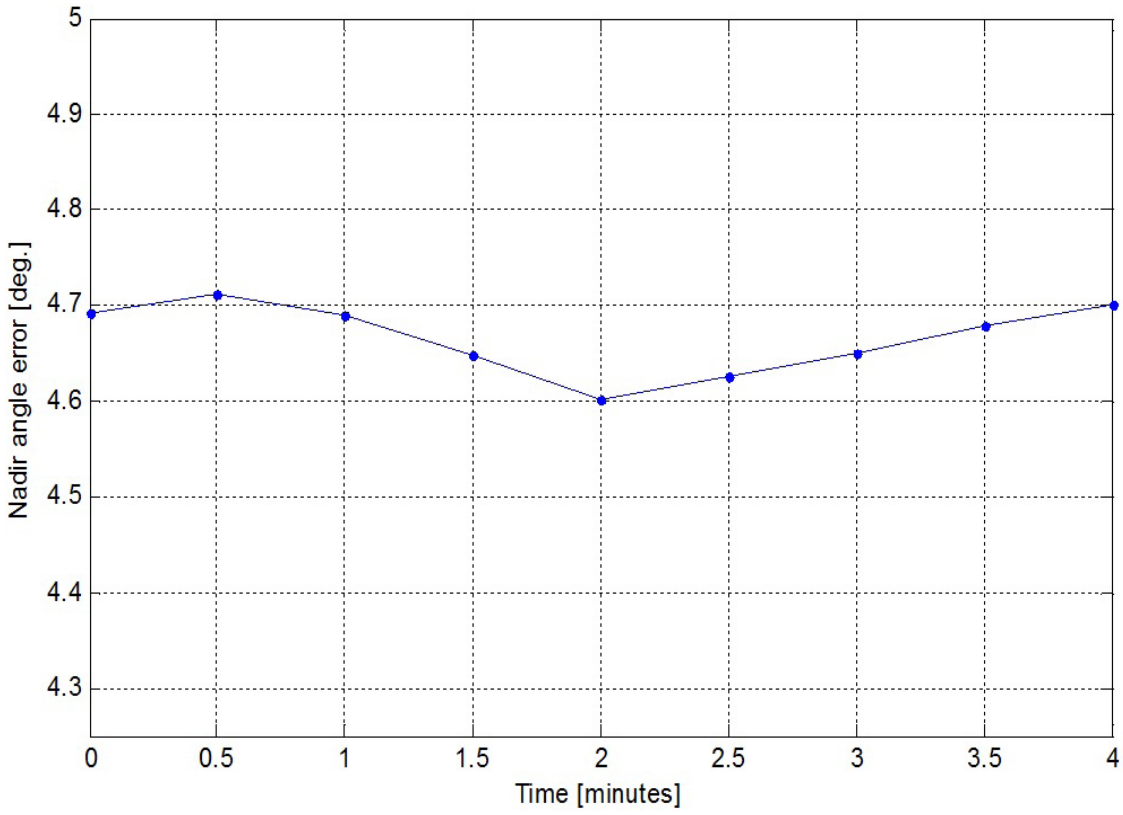

Fig. 4.34. Deviation from the nadir view of Argus obtained using spacecraft.

4.6.2 Cloud uncertainties within the NIR region

Cloud detection within the IR/NIR wavelength bands has some degree of uncertainty [Eliasson, S., 2013]. In each RE case study, the clouds are assumed to be uniform. But in general, real clouds are quite inhomogeneous [Zhang Z., et al., 2010]. Also, the uncertainty due to a large phase has a significant impact on retrievals [Eliasson, S., 2013]. Having diverse types of cloud phases in the atmosphere may give incorrect cloud types, as discussed in section 4.4. The effect of choosing a different atmospheric mixing ratio for the calculation of RE can lead to systematic uncertainties. Normally, the NIR radiances apply only to the top of clouds, since only the first four optical depths of a cloud contribute to its actual reflectance, because the smallest ice particles are in general only close to the top of the clouds [McFarquhar G. M. et al., 1998]. Overall, retrievals from any cloud technique range from a 10% to 20% degree of uncertainty, when clouds are optically thick, are partly mixed-phase, are made up of multi-layer clouds, or any combination of these factors [Waliser D. E., et al., 2009].

5.0 SHORTWAVE UPWELLING RADIATIVE FLUX (SWupRF) TECHNIQUE - CLOUD SCENES

5.1 SWupRF by Space-Orbiting Argus Dataset

The integrated absorption technique is applied to determine the magnitude of SWupRF within Argus wavelength bands of O_2, H_2O, CO_2 and CH_4 [Siddiqui, R., et al., 2017]. This approach is used to estimate the upwelling radiative flux variation within spectral range of 900 nm to 1700 nm of different weeks per passes of the Argus dataset.

5.1.1 Methodology

The Short Wave upwelling Radiative Flux (SWupRF) is calculated by using selected weeks of Argus spectra. The SWupRF model loads a set of observed spectra for different week per pass per observation number and integrates each spectrum over the different spectral range of bands of interest by applying Eq. (5.1) through Eq. (5.4):

$$(SWupRF)obs = \int_{\lambda 1}^{\lambda max} S(\lambda) d\lambda \quad (5.1)$$

where

$(SWupRF)obs$ = Short Wave upwelling Radiative Flux of Argus observed spectra

$S(\lambda)$ = Spectral radiance [$(Wm^{-2}\ sr^{-1}\ (1/cm)^{-1}$]

$\lambda 1$ to λmax = wavelength band

The equation 5.1 can also be written as

$$(SWupRF) \cong \sum_{i=1}^{N} S(\lambda i) d\lambda \quad (5.2)$$

To integrate over a solid, angle the following equations is applied:

$$(SWupRF)_{\Omega} = (SWupRF) \times 2\pi \int_0^{\frac{\pi}{2}} sin\theta cos\theta d\theta \ = \pi(SWupRF) \quad (5.3)$$

The total spectral SWupRF is calculated by the following relationship:

$$(SWupRF)_{total} = (SWupRF)_{\Omega} \text{ x } r_v \quad (5.4)$$

where r_v = resolution wavenumber.

5.1.2 SWupRF results (Argus observed dataset)

All the selected weeks per passes with four set of observations numbers have been used to calculate the $(\text{SWupRF})_{\text{obs}}$ by applying the 'Integrate observed spectra model'. Figure 5.1 illustrates the full set of Argus observed spectra of week 08 pass 61 (October 30th, 2009) over the Arabian Sea & Seychelles. The average range of$(\text{SWupRF} - \text{week08pass61})_{\text{obs}}$ is 1.65 [0.12 to 3.15] W/m^2. The observation number 116 show the probability of high level clouds with SWupRF of 3.2 W/m^2. Similarly, observation number 64 show probability of middle levels clouds with SWupRF of 2.7 and observation number 238 and 196 show low level clouds and no cloud scenes with SWupRF of 1.7 and 1.2 W/m^2 respectively.

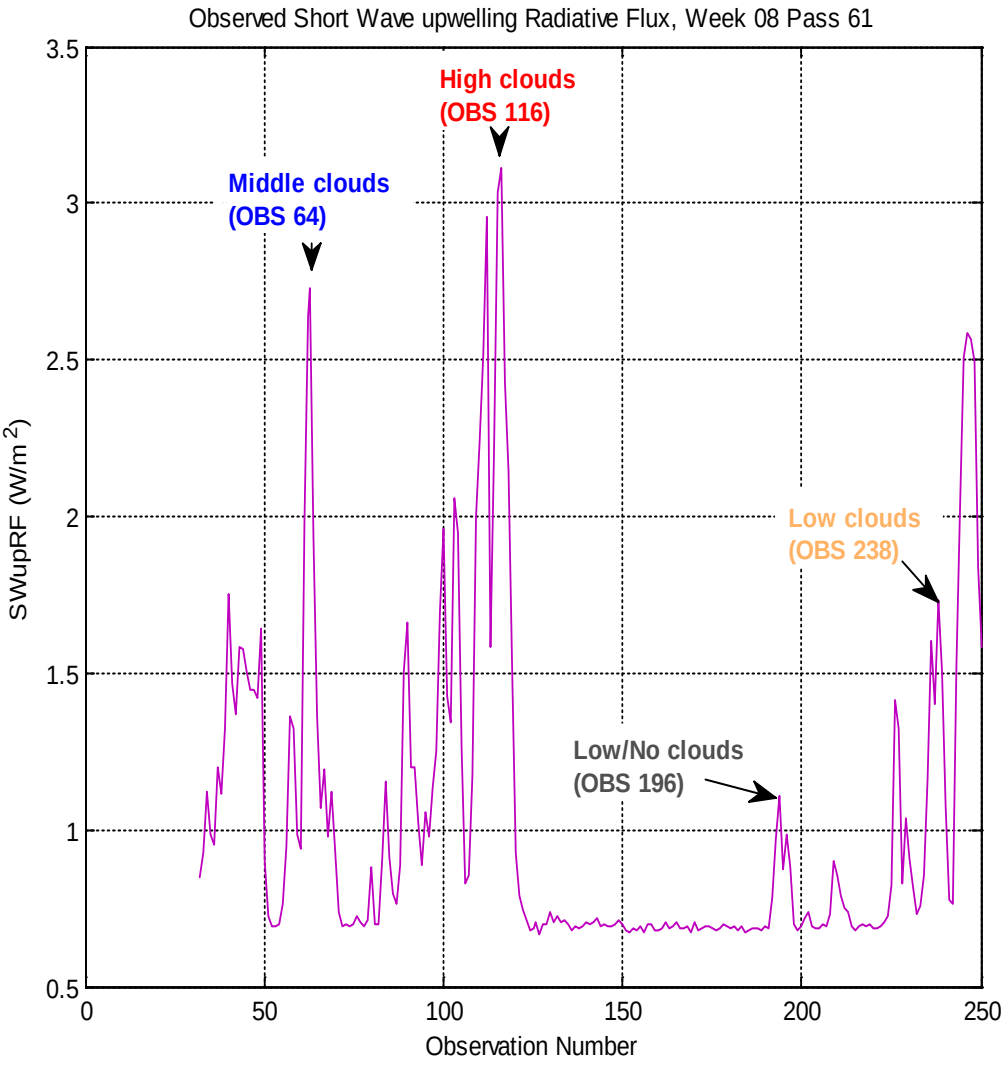

Fig. 5.1. Total radiative flux profile of Argus observed spectra of week 08 pass 61 (October 30th, 2009), show four different observation numbers with types of clouds.

Figure 5.2 illustrates the full set of Argus observed spectra of week 14 pass 52 (March 4th, 2010) over Toronto, Canada. The average range of $(\text{SWupRF} - \text{week14pass52})_{\text{obs}}$ is 1.0 [0.40 to 1.60] W/m^2. The observation numbers 22 and 124 show the probability of low level clouds with SWupRF of 1.0 and 1.4 W/m^2 respectively.

Similarly, observation numbers 100 and 120 show a probability of no clouds with SWupRF of 0.9 and 0.4 W/m^2 respectively.

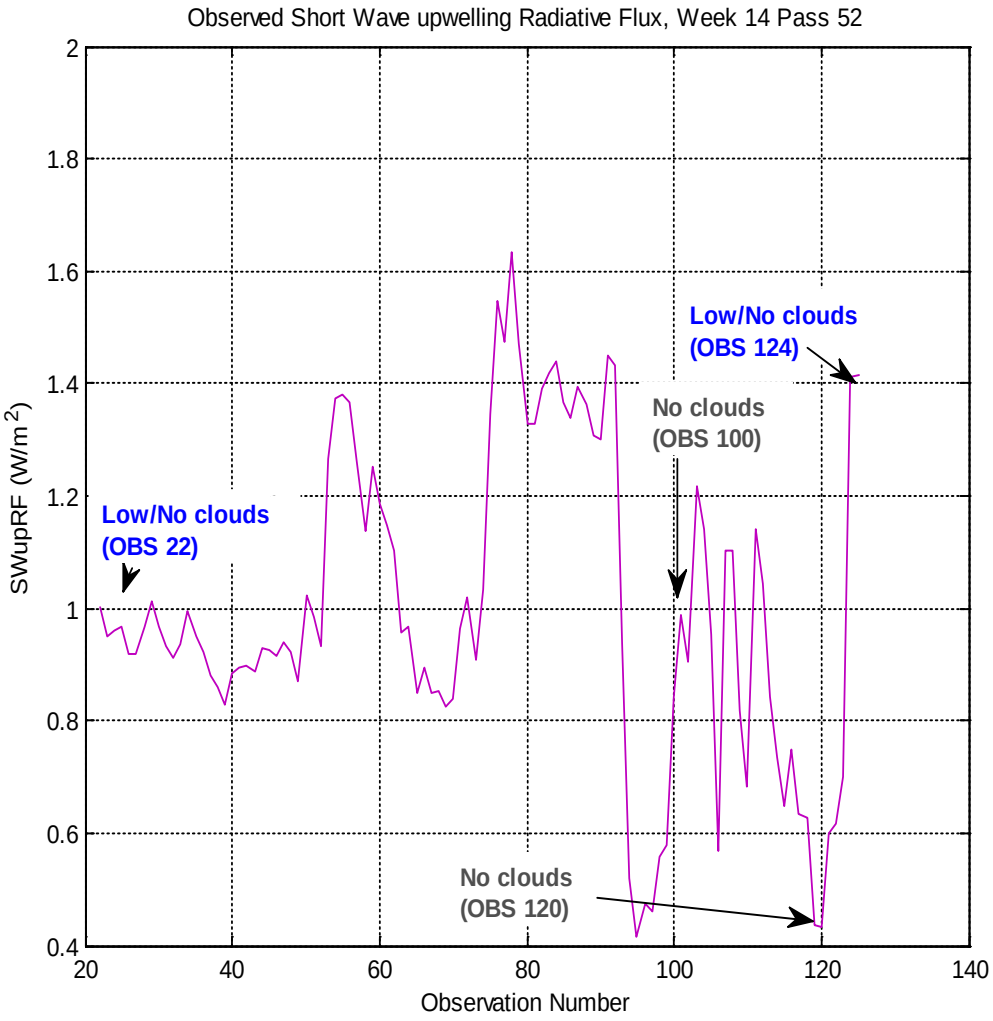

Fig. 5.2. Total radiative flux profile of Argus observed spectra of week 14 pass 52 (March 4th, 2010), show four different observation numbers with clouds and no clouds.

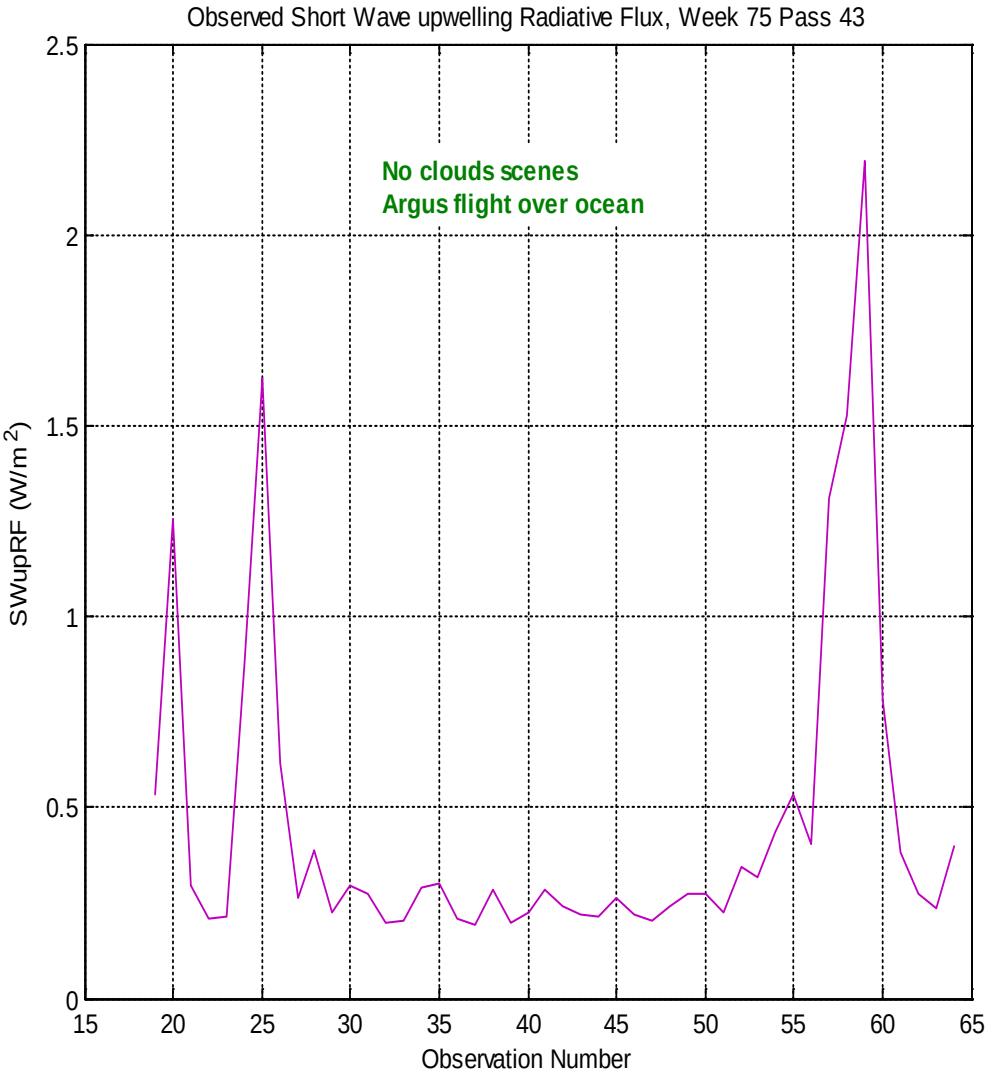

Fig. 5.3. Total radiative flux profile of Argus observed spectra of week 75 pass 43 (August 14th, 2013), show low flux profile with no clouds.

Figure 5.3 illustrates the full set of Argus observed spectra of week 75 pass 43 (August 14th, 2013) over the North Pacific Ocean. The average range of $(\mathrm{SWupRF} - \mathrm{week75pass43})_{obs}$ is 0.925 [0.25 to 1.60] W/m^2. The observation numbers 20, 25 and 58 show some degree high flux intensity. The rest of the observations for this Argus week show a flux profile of less than 0.30 W/m^2.

The higher the flux (W/m^2) the higher probabilty that the scene is contaminated with clouds. The lower flux profile indicates clear sky onditions or patchy/partial clouds or ice clouds.

5.2. Comparison with MODIS (Aqua/Terra) Satellite Data

The presentation of efficient detection of cloud scenes is usually based on by associations to the other satellites imagery [Jedlovec, G., 2010]. In this study, a validation is performed through with MODIS-Aqua/Terra satellite imagery. It is very important to compare numerous cloud scenes to validate cloud detection methodologies because of the large variation in the spectral characteristics present in real observation spectra. Each cloud detection method may use different satellite sensors, different wavelength selections bands, and different geographical regions, different date and time etc. [Jedlovec G., 2009]. In our analysis, all the three-selected data set of Argus space flight show a very good agreement in order to detect efficiently cloud scenes over different regions in comparisons with MODIS - Aqua/Terra satellite cloud masks. The results of all the selected data set of Argus 1000, as shown in Table 5.1, indicates that all the validations of cloud scenes ensured reasonably well in capturing the clouds and non-cloud scenes by the results of both RE and SWupRF techniques.

Table 5.1. Argus - RE and SWupRF comparison with MODIS images

W/P/O	Albedo (estimated)	Spectral Radiance (Max.) $W/m^2sr^{-1}(cm^{-1})^{-1}$	Spectral Radiance (Min.) $W/m^2sr^{-1}(cm^{-1})^{-1}$	RE	SWupRF (W/m^2)	Cloud Types (MODIS cloud images)
08/61/64	0.5	52	10	0.35	2.7	Middle/Thick
08/61/116	0.7	68	11	4.11	3.2	Thick/middle
08/61/196	0.3	22	10	0.35	1.2	No/low
08/61/238	0.3	45	09	2.36	1.7	Thick/thin
14/52/22	0.4	45	18	4.70	1.0	Middle/thick
14/52/100	0.2	38	25	0.89	0.9	No
14/52/120	0.1	18	15	3.3	0.5	No/low
14/52/124	0.4	60	40	2.08	1.4	Middle/thin
75/43/19	0.1	18	15	1.72	0.5	No
75/43/30	0.1	11	07	-0.30	0.25	No
75/43/43	0.1	07	05	-0.64	0.25	No
75/43/65	0.25	32	25	-0.26	1.1	-

Figures 5.4, 5.5 and 5.6 present the agreement of RE and SWupRF methods based results of Argus data set and the MODIS cloud images. The comparison is splits into three types of situations of cloud and clear sky, show the variability of different types of cloud surface strength.

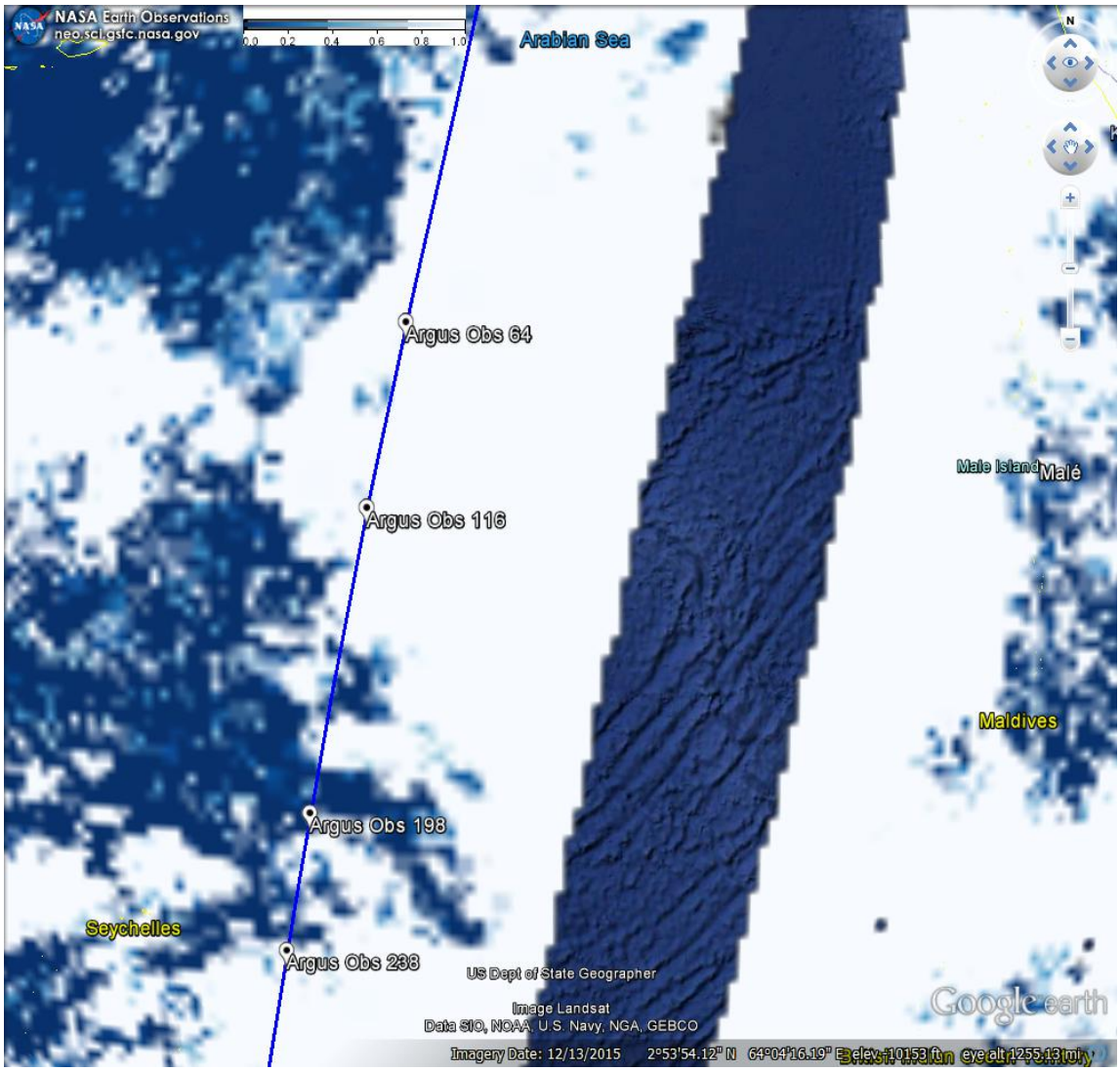

Fig. 5.4. Argus 1000 infrared space flight path with MODIS cloud masks of week 08 pass 61 for October 30, 2009 over the Arabian Sea.

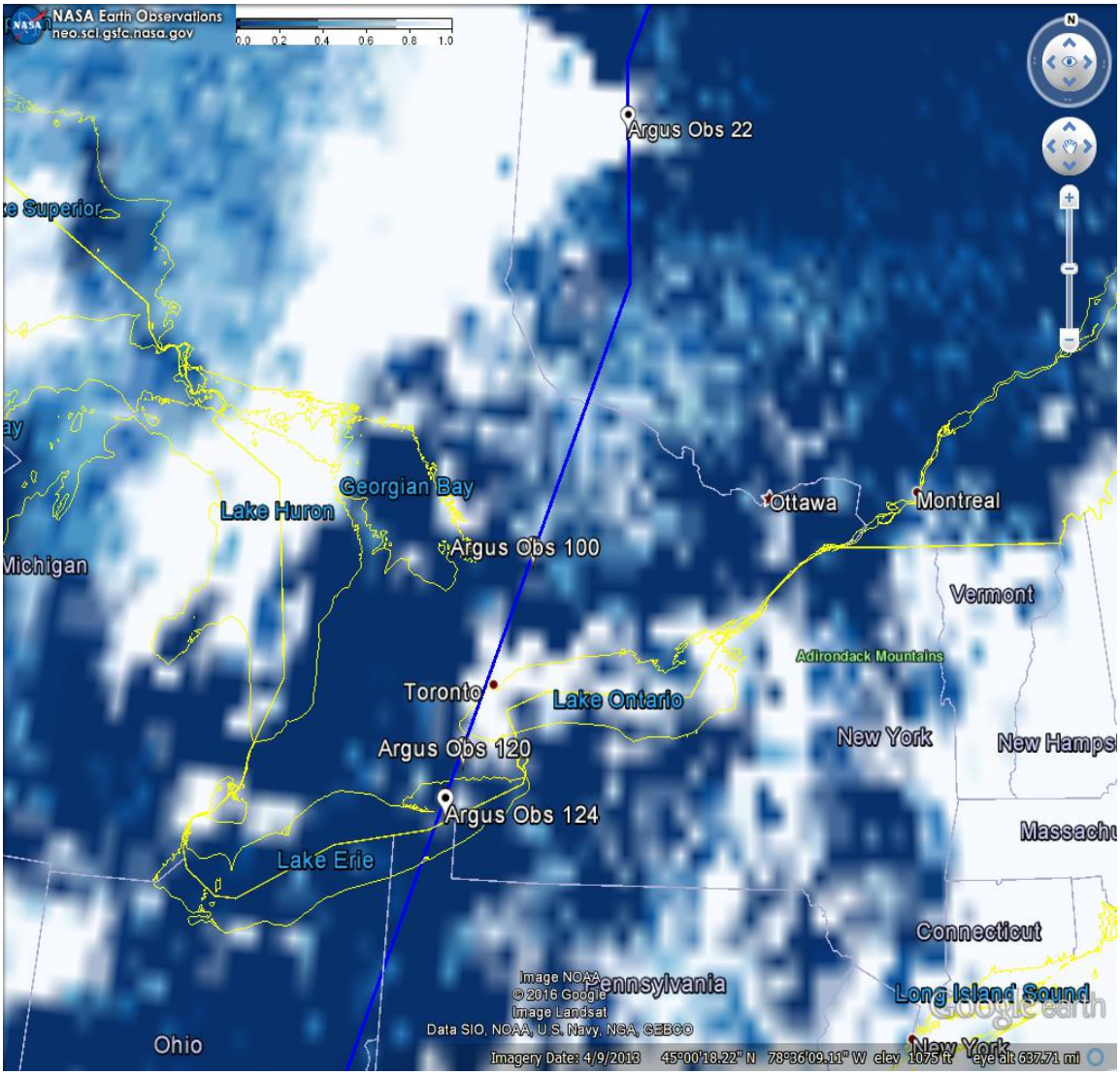

Fig. 5.5. Argus 1000 infrared space flight path with MODIS cloud masks of week 14 pass 52 for March 04, 2010 over Ontario, Canada.

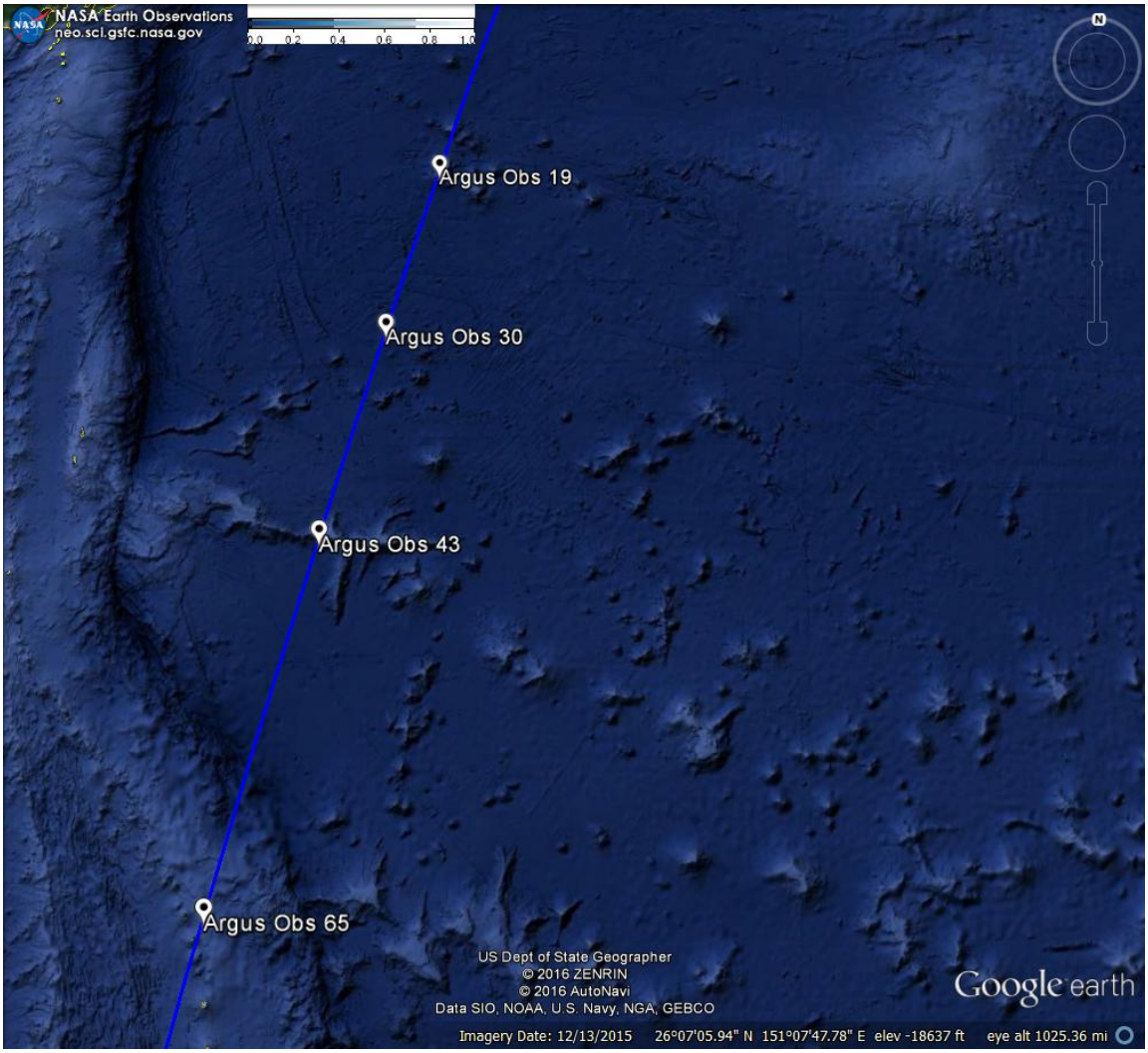

Fig. 5.6. Argus 1000 infrared space flight path with MODIS no-cloud masks of week 75 pass 43 for August 14, 2013 over North Pacific Ocean.

The RE and SWupRF results are shown in Figures 5.7, 5.8 and 5.9 for the potential candidates of cloud or no cloud scenes from different weeks per passes per observation of Argus dataset, in comparison with MODIS clouds coverage.

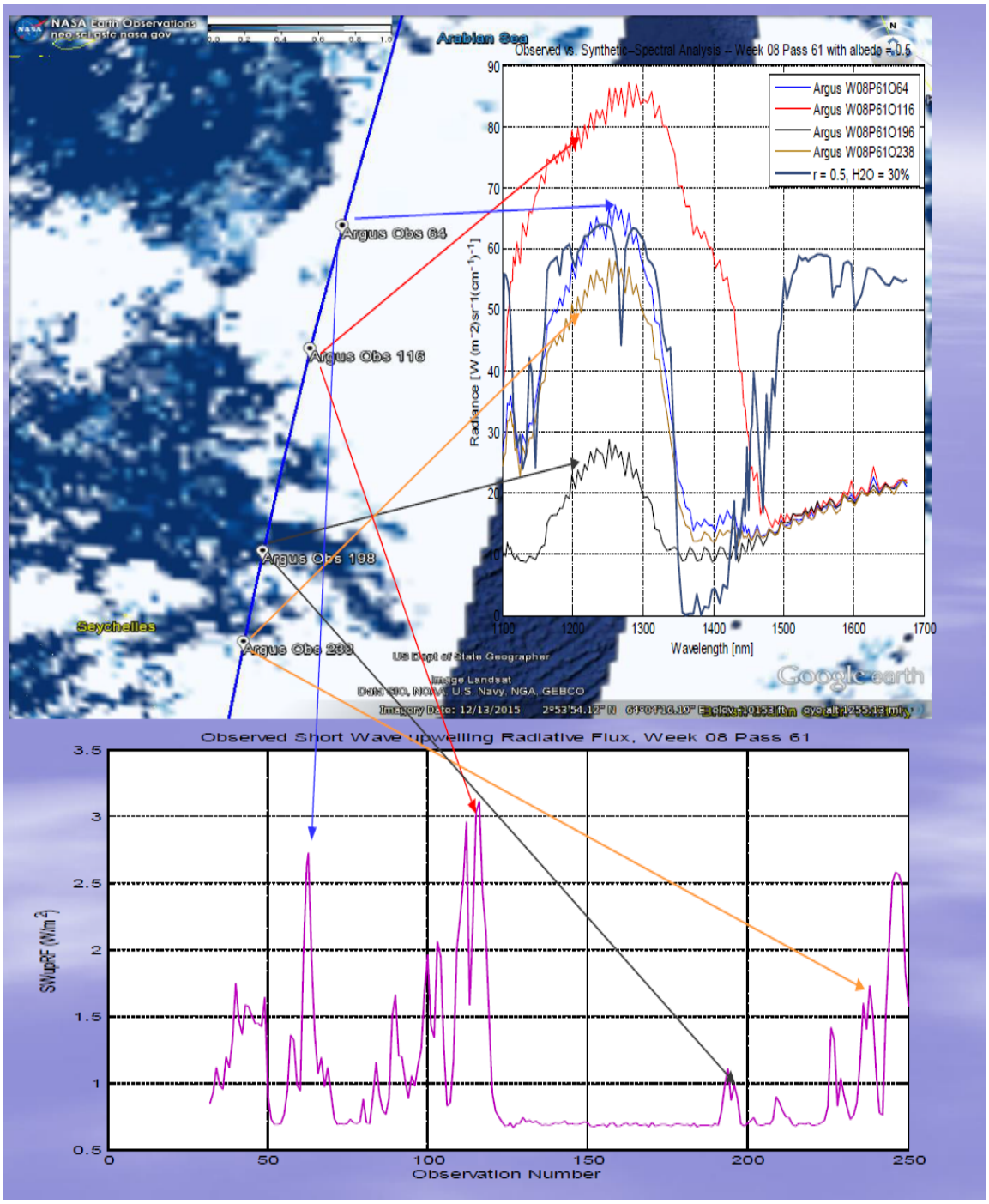

Fig. 5.7 (a). RE for Argus week 08 pass 61 with observations number 64/116/196/238 vs. GENSPECT-Synthetic model; (b) Argus flight vs. Terra/Aqua (MODIS cloud sat) with full and partial cloud scenes over the Arabian Sea; (c) SWupRF (0.12 to 3.15 W/m^2) shows the high and low radiative flux intensity within the same range of Argus observation number.

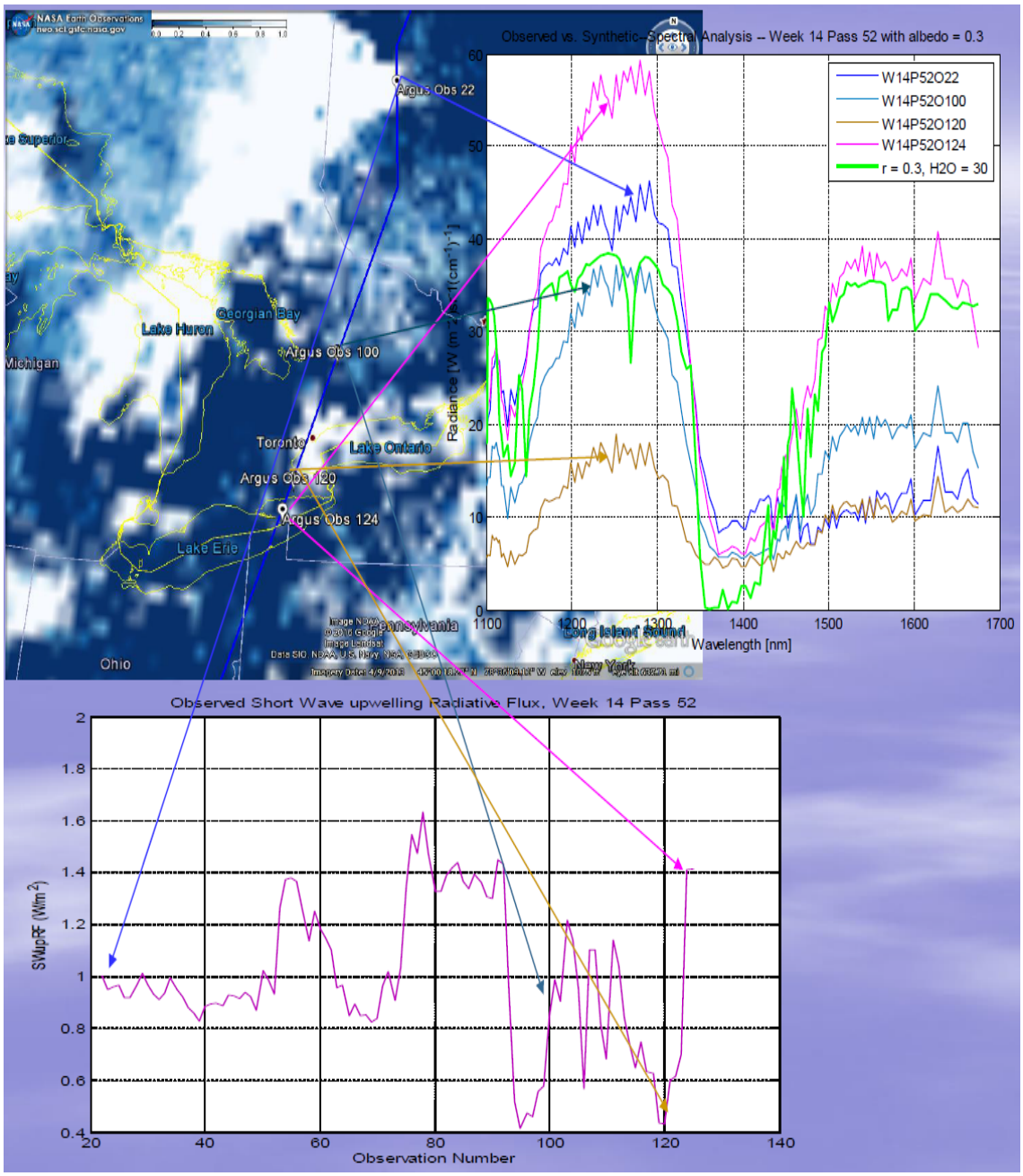

Fig. 5.8(a). RE for Argus week 14 pass 52 with observations number 22/100/120/124 vs. GENSPECT-Synthetic model. (b) Argus flight vs. Terra/Aqua (MODIS cloud sat) with full and partial cloud scenes over Ontario, Canada (c) SWupRF (0.40 to 1.60 W/m^2) shows the high and low radiative flux intensity within the same range of Argus observation number.

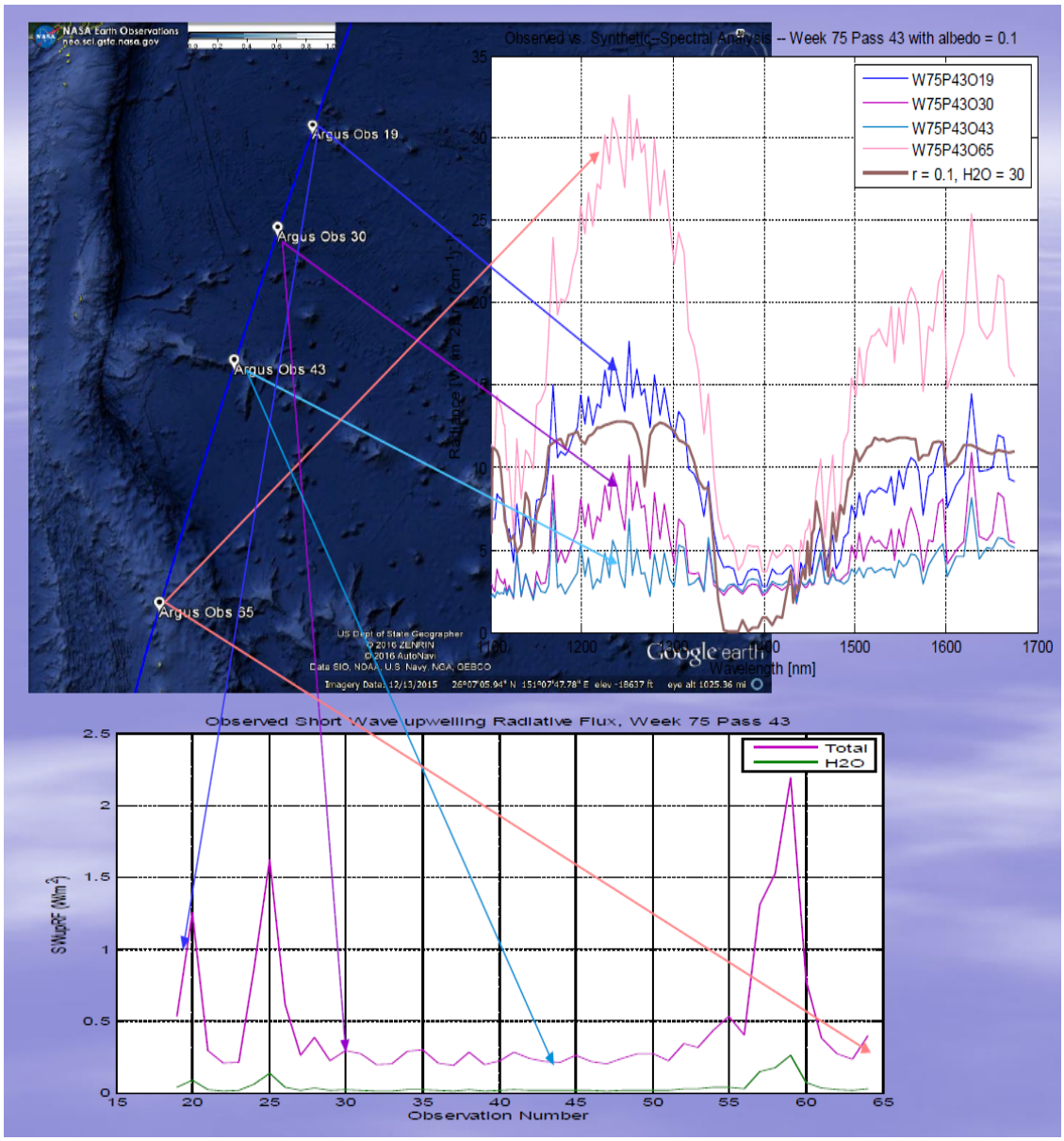

Fig. 5.9(a). RE for Argus week 75 pass 43 with observations number 19/30/43/65 vs. GENSPECT-Synthetic model. (b) Argus flight vs. Terra/Aqua (MODIS cloud sat) with full and partial cloud scenes over North Pacific Ocean (c) SWupRF (0.25 to 1.60 W/m^2) shows the high and low radiative flux intensity within the same range of Argus observation number.

5.3 Accuracy Analysis

To evaluate the RE and SWupRF algorithms more comprehensively, quantitative analysis is performed on a full set of Argus observations. Figures 5.10 and 5.11 are histograms show the maximum and minimum flux intensity and RE for the subsequent probability of cloud and non-cloud scenes, respectively. The results of both RE and SWupRF for week 08 pass 61 with observation number 37 and week 75 pass 43 with observation numbers 115 & 116 are agreed for the efficient detection of cloud scenes.

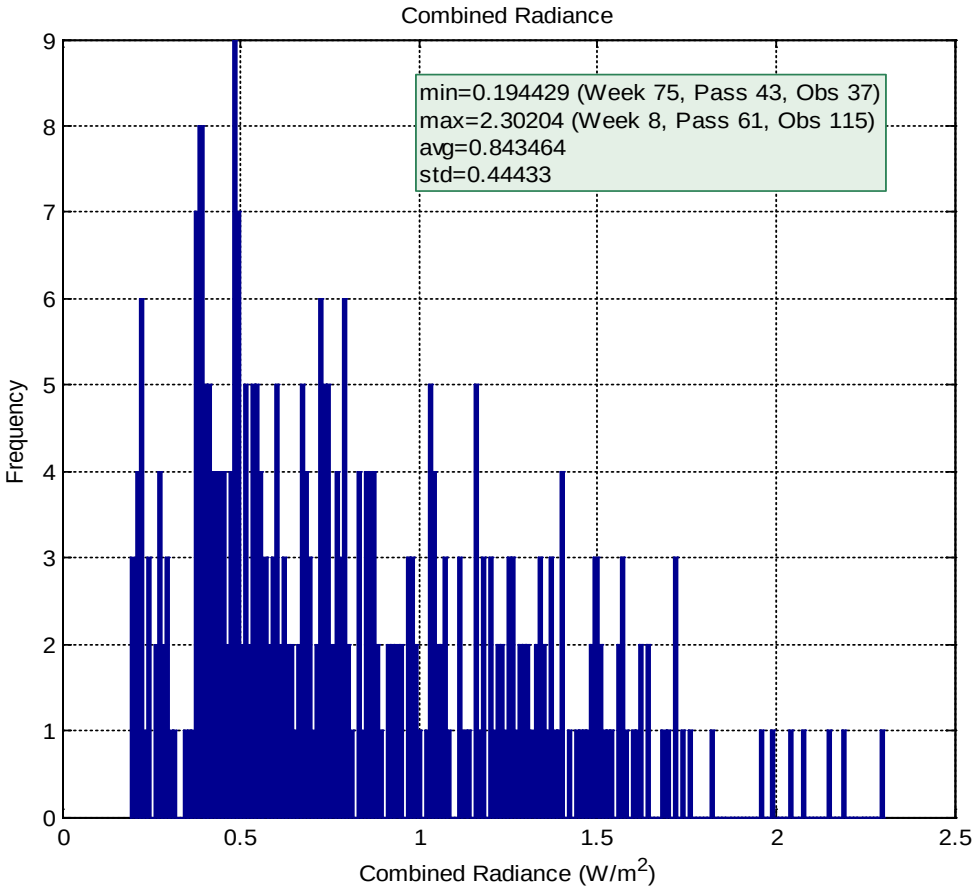

Fig. 5.10. Histogram of the Argus weeks/passes/observations with maximum flux intensity = 2.30 W/m^2, minimum flux intensity = 0.2 W/m^2, average of full spectral data set = 0.84 W/m^2.

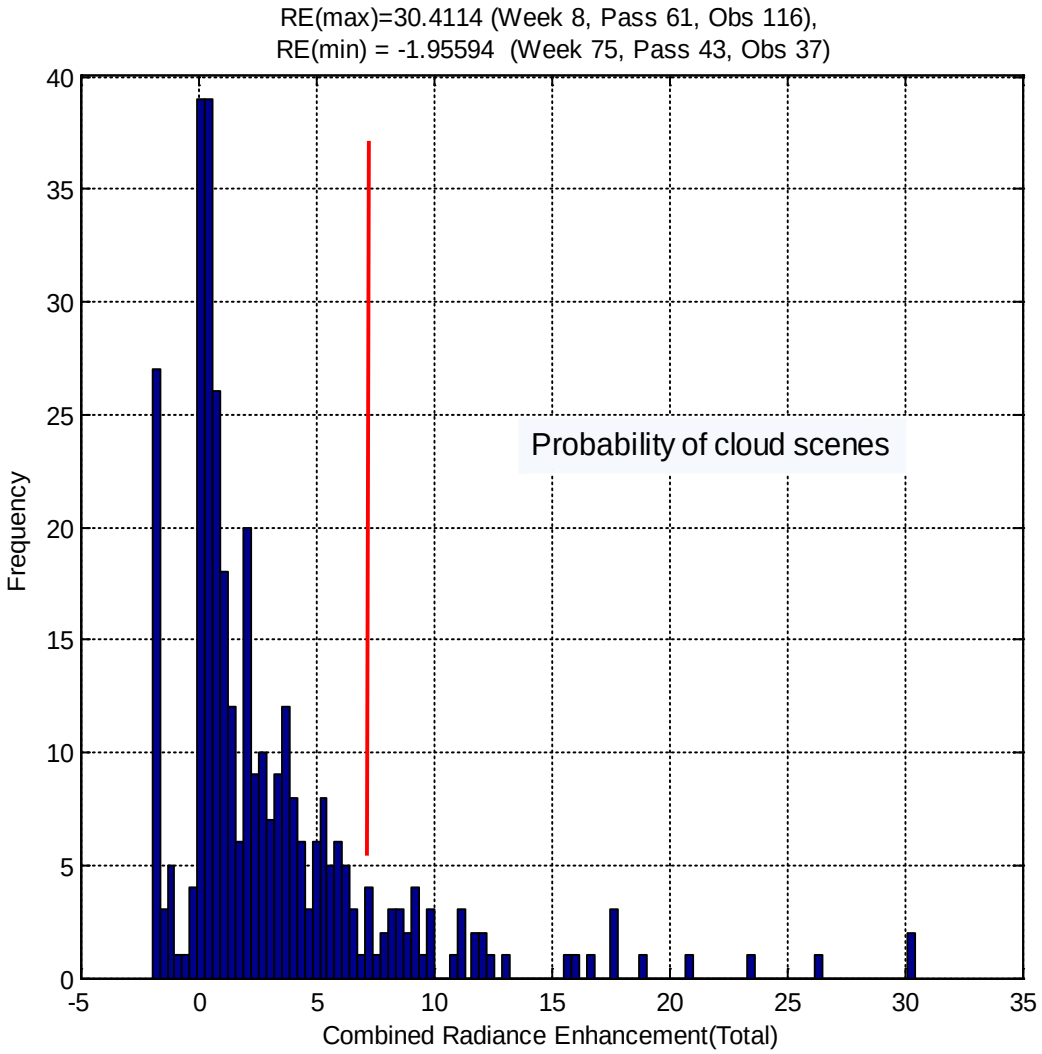

Fig. 5.11. Histogram of the subsequent probability of cloud and non-cloud scenes.

A high value of RE for the full wavelength bands, especially for H_2O and O_2 bands in comparison with SWupRF results, signifies a greater probability of cloud scenes by the Argus dataset.

The overall results of RE and SWupRF shown an excellent agreement for the efficient detection of cloud scenes [Siddiqui, R., et al., 2015; Siddiqui, R., et al., 2017].

It is found that there is some degree of uncertainty likely introduced by the following effects:

(i) the difference between the satellite path and the Argus boresight;

(ii) mixing of water vapor and carbon dioxide within atmospheric layers, which affects calculation of the radiance enhancement;

(iii) cloud height is not validated as compared to the individual thickness of the types of clouds.

(iv) selection of the average number of satellite Sun and nadir angles of the Argus data set.

6.0 CONCLUSIONS AND FUTURE WORK

6.1 Conclusions

This thesis presents a novel methodology that uses radiance enhancement (RE) and shortwave upwelling radiative flux (SWupRF) for the detection and classification of cloud scenes recorded by space borne Argus 1000 spectrometer operating in the NIR range 1100 nm to 1700 nm. The Argus spectrometer continuously monitors the sources and sinks of the trace gases. With nine years of orbital heritage on its first flight, the miniature spectrometer meets all requirements for stable and durable operation in Earth orbit. Applying GENSPECT LBL [Quine B. M. et al., 2002] as the tool to model radiative transfer, Argus retrieval products are generated. The two methods have been validated by real observations using collected MODIS imagery. The first method describes the RE technique for the efficient detection of clouds by using the remote sensing spectral dataset of Argus alongwith the GENSPECT model. This method enables us to calculate the enhancement of radiance by using different atmospheric concentrations of O_2, H_2O, CO_2 and CH_4, albedos and satellite sun and nadir angles [Siddiqui R., et al., 2015; Siddiqui R., et al., 2016].

The second method tested for the efficient detection of cloud scenes is based on the SWupRF results [Siddiqui R., et al., 2017]. The cloud detection technique is applied on high values of radiative intensity in terms of the calculated flux by using integrated spectral dataset of the selected range of Argus observations. Both RE and SWupRF results show a good agreement to detect different types clouds with MODIS satellite imagery. The

methodology presented can be used to reduce the quantification process of cloud detection. The methodology will therefore be helpful in describing the mechanism of climate change.

In summary, the major findings with Argus instruments are:

- The RE-based method [Siddiqui R., et al., 2015] by using Argus measurements alongwith GENSPECT LBL radiative transfer model, allows the efficient detection of cloud scenes. The results have been published in the International Journal of Space Science and Engineering.
- The RE technique can easily differentiate the high, medium and low cloud scenes by applying the full set of weeks per pass of the Argus 1000 flight.
- Clouds and water vapor appear to be far more radiatively dominant in this important spectral region 1100 nm to 1700 nm compared to CO_2.
- The Argus 1000 micro-spectrometer has been demonstrated as a capable nanosatellite payload able to perform significant scientific investigations, especially monitoring CO_2, CH_4, and H_2O.
- All the scenarios of optimization, show that our results are the first ever experimental data techniques within NIR spectral wavelength bands of 1100-1700 nm, giving an excellent contest between theoretical model and the real observations to detect clouds as discussed earlier on pages 97 and 113.
- Surface radiative flux of SW within NIR spectral range from 1100 nm to 1700 nm were determined using the satellite based measurement over different spatial locations during the period of 2009 to 2013 under different atmospheric concentrations.

- The Argus spectrometer is an excellent tool to calculate the shortwave upwelling radiative flux (SWupRF) [Siddiqui R., et al., 2017, In press] within the wavelength bands of O_2, H_2O, CO_2 and CH_4 as discussed earlier on pages 131 and 135. The manuscript has been accepted and will be publish in the Canadian Journal of Remote Sensing (peer review general).

The Argus 1000 micro-spectrometer has been tested the potential of nanosatellites to perform significant science missions, especially monitoring CO_2 [Jagpal R.K, 2011], cloud classification by RE technique [Siddiqui R. et al., 2015] and calculates radiative flux by using SWupRF methodology [Siddiqui R. et al., 2017]. In the last nine years that the Argus 1000 has been in operation, more than 300 observations sequences have been recorded [Siddiqui, R et al., 2015] over a series of land and ocean targets. Argus instruments orbiting the Earth are now providing a remote sensing dataset that can be accepted globally for improving our understanding of for the detection of cloud scene and the radiative flux profile within the SW range.

6.2 Future Work

This dissertation focuses mainly on the global signature of different types of cloud scenes detected by using an Argus spectrometer. The recommendations for future work include:

- This type of analysis can be extended to a larger and more representative Argus datasets by using different locations over the globe.
- Cloud RE for the same locations from the complete set of Argus retrieved data can be compared individually.

- Care must be taken to ensure that a fair comparison is made considering the difficulty in observing mixed-phase clouds from different surfaces, particularly in the presence of low-level liquid clouds, multiple layers of unknown surfaces or water clouds.
- To calculate RE within the O_2 absorption band at 1260 nm, a plateau assumption has been applied, which should be examined further for use as a substitution measurement for atmospheric path density. Observations of the Oxygen-A band may be needed as an additional data set.
- Clouds and snow have almost the same albedo and can become an issue to discriminate the types of clouds. There is therefore a need for proper interpretation of spectra to calculate RE and SWupRF.
- Detailed sub-classification of clouds by Argus data set is also required.
- There is also significant uncertainty in several RE results within the water absorption bands. More studies are required to compare the Argus dataset within this region.
- Data retrieved by the new Argus spectrometer with high spectral wavelength bands will be a better source for comparing the RE and SWupRF results.
- Future space missions may carry sets of Argus instruments each tuned to a particular spectrum range and species. Instruments may be developed to observe aerosols and investigate the RE by aerosols.

REFERENCES

Abrarov, S. M., Quine, B. M., and Jagpal, R. K., 2010a. Rapidly convergent series for high-accuracy calculation of the Voigt function, *J. Quant. Spectrosc. Radiat. Transfer*, 111, 372-375.

Atkinson, P.M. and Tatnall, A.R.L., 1997. Introduction neural networks in remote sensing. *International Journal of remote sensing*, *18*(4), pp.699-709.

Andrews, T., Forster, P. M., & Gregory, J. M., 2009. A surface energy perspective on climate change. *Journal of Climate*, 22(10), 2557-2570.

Ackerman, S.A., Strabala, K.I., Menzel, W.P., Frey, R.A., Moeller, C.C. and Gumley, L.E., 1998. Discriminating clear sky from clouds with MODIS. *Journal of geophysical research*, *103*(D24), pp.32-141.

Arnaud Czaja, 2016, Notes on Atmospheric Physics.

Arking, A., 1991. The radiative effects of clouds and their impact on climate. *Bulletin of the American Meteorological Society*, *72*(6), pp.795-813.

Aggarwal, S., 2004. Principles of remote sensing. *Satellite remote sensing and GIS applications in agricultural meteorology*, *23*.

Alsalem, N., Siddiqui, R., Tsouvaltsidis, C. and Quine, B., 2016. Clouds effect on the Atmospheric Total Column Carbon Dioxide Retrieval by Space Orbiting Argus 1000 Micro-spectrometer: Introductory Study. *arXiv preprint arXiv:1612.01172*.

Amy Elizabeth Chang, 2008. Controlling Cloud Albedo: Recent Advances in Understanding the Geo-Engineering Technique Proposed by John Latham

ACS climate science tool kit, water vapor and CO_2: https://www.acs.org/content/acs/en/climatescience/climatesciencenarratives/its-water-vapor-not-the-co2.html.

Czaja, A., 2017, Notes on Atmospheric Chemistry, Physics Department, Imperial College, London.

Argus 1000 IR Spectrometer, Owner's Manual, Thoth Technology Inc. *Document Number OG728001*, Release 1.03

Bernstein, L., Bosch, P., Canziani, O., Chen, Z., Christ, R. and Riahi, K., 2008. *IPCC, 2007: climate change 2007: synthesis report*. IPCC.

Bouter, L.M. and van Diedenhoven, B., 2007 Satellite remote sensing of cloud properties in support of tropospheric trace gas retrievals.

Bracher, A., Bovensmann, H., Bramstedt, K., Burrows, J. P., Clarmann, T. V., Eichmann, K. U., & Wuttke, M. W., 2005. Cross comparisons measured by the atmospheric ENVISAT instruments GOMOS, MIPAS, and SCIAMACHY. Advances in Space Research, 36(5), 855-867.

Barnes, R.A., E.E.Eplee, et al., 1999. Changes in the radiometric sensitivity of Sea WiFS determined from lunar and solar based measurements, Applied Optics, 38, 4649-4664.

Blumthaler, M., Ambach, W. and Ellinger, R., 1997. Increase in solar UV radiation with altitude. *Journal of photochemistry and Photobiology B: Biology*, *39*(2), pp.130-134.

Barnes, W., 2006. An Overview of MODIS Radiometric Calibration and Characterization. *Advances in Atmospheric Sciences*, *1*.

Boucher, O., Schwartz, S.O., Ackerman, T.P., Anderson, T.L., Bergstrom, B., Bonnel, B., Chýlek, P., Dahlback, A., Fouquart, Y., Fu, Q. and Halthore, R.N., 1998. Intercomparison of models representing direct shortwave radiative forcing by sulfate aerosols. *Journal of Geophysical Research: Atmospheres*, *103*(D14), pp.16979-16998.

Burrows, J.P., Weber, M., Buchwitz, M., Rozanov, V., Ladstätter-Weißenmayer, A., Richter, A., DeBeek, R., Hoogen, R., Bramstedt, K., Eichmann, K.U. and Eisinger, M., 1999. The global ozone monitoring experiment (GOME): Mission concept and first scientific results. *Journal of the Atmospheric Sciences*, *56*(2), pp.151-175.

Buchwitz, M., De Beek, R., Burrows, J. P., Bovensmann, H., Warneke, T., Notholt, J., Meirink, J. F., Goede, A. P. H., Bergamaschi, P., Körner, S., Heimann, M., and Schulz, A., 2005a. Atmospheric methane and carbon dioxide from SCIAMACHY satellite data: initial comparison with chemistry and transport models, *Atmos. Chem. Phys*., 5, 941–962.

Buchwitz, M., De Beek, R., Noel, S., Burrows, J. P., Bovensmann, H., Bremer, H., Bergamaschi, P., Körner, S., and Heimann, M., 2005b. Carbon monoxide, methane and carbon dioxide columns retrieved from SCIAMACHY by WFM-DOAS: year 2003 initial data set, *Atmos. Chem. Phys*., 5, 3313–3329.

Cheng, T., Gu, X., Chen, L., Yu, T. and Tian, G., 2007, July. Cloud detection based on the spectral, multi-angular, and polarized characteristics of cloud. In *2007 IEEE International Geoscience and Remote Sensing Symposium* (pp. 3321-3324). Ieee.

Chesser, H., Lee, R., Benari, G., Jagpal, R.K., Lam, K. and Quine, B., 2012. Geolocation of Argus flight data. *IEEE Transactions on Geoscience and Remote Sensing*, *50*(2), pp.357-361.

Camps-Valls, G., Tuia, D., Gómez-Chova, L., Jiménez, S. and Malo, J., 2011. Remote sensing image processing. *Synthesis Lectures on Image, Video, and Multimedia Processing*, *5*(1), pp.1-192.

Chylek, P. and Borel, C., 2004. Mixed phase cloud water/ice structure from high spatial resolution satellite data. *Geophysical research letters*, *31*(14).

Cutillo, L., Amato, U., Antoniadis, A., Cuomo, V. and Serio, C., 2004. Cloud detection from multispectral satellite images. In *Proceedings from IEEE Gold Conference, University Parthenope, Naples, Italy*.

Cooper, S.J., L'Ecuyer, T.S. and Stephens, G.L., 2003. The impact of explicit cloud boundary information on ice cloud microphysical property retrievals from infrared radiances. *Journal of Geophysical Research: Atmospheres*, *108*(D3).

Chen, J., Carlson, B.E. and Del Genio, A.D., 2002. Evidence for strengthening of the tropical general circulation in the 1990s. *Science*, *295*(5556), pp.838-841.

Christopher, S. A., and J. Zhang (2002a), Shortwave aerosol radiative forcing from MODIS and CERES observations over the oceans, *Geophys. Res. Lett.*, *29*(18), 1859, doi:10.1029/2002GL014803.

Chevallier, F., Bréon, F.M. and Rayner, P.J., 2007. Contribution of the Orbiting Carbon Observatory to the estimation of CO_2 sources and sinks: Theoretical study in a variational data assimilation framework. *Journal of Geophysical Research: Atmospheres*, *112*(D9).

Chylek, P., Robinson, S., Dubey, M.K., King, M.D., Fu, Q. and Clodius, W.B., 2006. Comparison of near-infrared and thermal infrared cloud phase detections. *Journal of Geophysical Research: Atmospheres*, *111*(D20).

Dufour, D. G.; Drummond, J. R.; McElroy, C. T.; Midwinter, C.;Bernath, P. F.; Walker, K. A.; Evans, W. F. J.; Puckrin, E.; Nowlan, C., 2005. Intercomparison of Simultaneously Obtained Infrared (4.8 ím) and Visible (515-715 nm) Ozone Spectra Using ACE-FTS and MAESTRO. *J. Phys. Chem*., 109, 8760-8764.

Dufour, D. G., Drummond, J. R., McElroy, C. Th., Midwinter, C., Bernath, P. F., Walker, K. A., and Nowlan, C., 2006. Simultaneous measurements of visible (400-700 nm) and infrared (3.4 μm) NO2 absorption, *J. Phys. Chem*. A, 110, 12414–12418.

Duggan, P., Sinclair, P. M., LeFlohic, M. P., Forsman, J. W., Berman, R., May, A. D., and Drummond, J. R., 1993. Testing the Validity of the Optical Diffusion Coefficient: Line-Shape Measurements of CO Perturbed by N2, *Phys. Rev*. A, 48, 2077-2083.

DeMott, P.J., Hill, T.C., McCluskey, C.S., Prather, K.A., Collins, D.B., Sullivan, R.C., Ruppel, M.J., Mason, R.H., Irish, V.E., Lee, T. and Hwang, C.Y., 2016. Sea spray aerosol as a unique source of ice nucleating particles. *Proceedings of the National Academy of Sciences*, *113*(21), pp.5797-5803.

Ebert, E.E., 1987. A pattern recognition technique for distinguishing surface and cloud types in the Polar Regions. *Journal of Climate and Applied Meteorology*, *26*(10), pp.1412-1427.

Ebert, E.E., 1989. Analysis of polar clouds from satellite imagery using pattern recognition and a statistical cloud analysis scheme. *Journal of Applied Meteorology*, *28*(5), pp.382-399.

Ebert, E.E., Janowiak, J.E. and Kidd, C., 2007. Comparison of near-real-time precipitation estimates from satellite observations and numerical models. *Bulletin of the American Meteorological Society*, *88*(1), p.47.

Ervens, B., 2015. Modeling the processing of aerosol and trace gases in clouds and fogs. *Chemical reviews*, *115*(10), pp.4157-4198.

Encyclopædia Britannica, 2007., https://www.britannica.com/science/Rossby-wave

Elhag, M. and Bahrawi, J.A., 2014. Potential Rainwater Harvesting Improvement Using Advanced Remote Sensing Applications. *The Scientific World Journal*, *2014*.

Escrig, H., Batlles, F.J., Alonso, J., Baena, F.M., Bosch, J.L., Salbidegoitia, I.B. and Burgaleta, J.I., 2013. Cloud detection, classification and motion estimation using geostationary satellite imagery for cloud cover forecast. *Energy*, *55*, pp.853-859.

Evans, K.F., Walter, S.J., Heymsfield, A.J. and McFarquhar, G.M., 2002. Submillimeter-wave cloud ice radiometer: Simulations of retrieval algorithm performance. *Journal of Geophysical Research: Atmospheres*, *107*(D3).

Erel, Y., Pehkonen, S.O. and Hoffmann, M.R., 1993. Redox chemistry of iron in fog and stratus clouds. *Journal of Geophysical Research: Atmospheres*, *98*(D10), pp.18423-18434.

Eliasson, S., 2013. *Ice clouds in satellite observations and climate models* (Doctoral dissertation, Luleå tekniska universitet).

Fisher, A., 2014. Cloud and cloud-shadow detection in SPOT5 HRG imagery with automated morphological feature extraction. *Remote Sensing*, *6*(1), pp.776-800.

Fournier, N., Stammes, P., Graaf, M.D., Piters, A., Grzegorski, M. and Kokhanovsky, A., 2006. Improving cloud information over deserts from SCIAMACHY Oxygen A-band measurements. *Atmospheric Chemistry and Physics*, *6*(1), pp.163-172.

Feather, O.R., 1971. Method of increasing the likelihood of precipitation by the artificial introduction of sea water vapor into the atmosphere windward of an air lift region. *U.S. Patent 3*,601,312.

Field, C. B., Barros, V. R., Dokken, D. J., Mach, K. J., Mastrandrea, M. D., Bilir, T. E., ... & Girma, B., 2014. IPCC, 2014: *Climate Change 2014*: Impacts, Adaptation, and Vulnerability. Part A: Global and Sectoral Aspects. Contribution of Working Group II to the Fifth Assessment Report of the Intergovernmental Panel on Climate Change.

Fu, Q., Yang, P. and Sun, W.B., 1998. An accurate parameterization of the infrared radiative properties of cirrus clouds for climate models. *Journal of climate*, *11*(9), pp.2223-2237.

Fu, Q., Marcia B., and Dennis L. H., 2002. Tropical Cirrus and Water Vapor: An Effective Earth Infrared Iris?" *Atmospheric Physics and Chemistry*, Vol. 2, pp 31-37.

Furlan, C., De Oliveira, A. P., Soares, J., Codato, G., & Escobedo, J. F., 2012. The role of clouds in improving the regression model for hourly values of diffuse solar radiation. *Applied Energy*, 92, 240-254.

Fritz, S., 1949. The albedo of the planet Earth and of clouds. *Journal of Meteorology*, *6*(4), pp.277-282.

Gao, B.C., Han, W., Tsay, S.C. and Larsen, N.F., 1998. Cloud detection over the Arctic region using airborne imaging spectrometer data during the daytime. *Journal of Applied Meteorology*, *37*(11), pp.1421-1429.

Greenhough, J., Remedios, J.J. and Sembhi, H., 2005, April. Cloud Detection and Distributions from MIPAS Infra-Red Limb Observations (51). In *Envisat & ERS Symposium* (Vol. 572).

Ghosh, R.R., Ali, M.S., Hena, A. and Rahman, H., 2012. A Simple Cloud Detection Algorithm Using NOAA-AVHRR Satellite Data. *International Journal of Scientific & Engineering Research*, *3*(6).

Guo, F., Shen, X., Zou, L., Ren, Y., Qin, Y., Wang, X. and Wu, J., 2015. Cloud Detection Method Based on Spectral Area Ratios in MODIS Data. *Canadian Journal of Remote Sensing*, *41*(6), pp.561-576.

Gilbrech, R.J., McManamen, J.P., Wilson, T.R., Robinson, F. and Schoren, W.R., 2005. Cloud-Aerosol LIDAR and Infrared Pathfinder Satellite Observation (CALIPSO) Spacecraft: *Independent Technical Assessment*.

Gottwald, M., Krieg, E., Noël, S., Wuttke, M. and Bovensmann, H., 2006, July. Sciamachy 4 Years in Orbit-Instrument Operations and In-Flight Performance Status. In *Atmospheric Science Conference* (Vol. 628).

Gómez-Chova, L., Camps-Valls, G., Calpe-Maravilla, J., Guanter, L. and Moreno, J., 2007. Cloud-screening algorithm for ENVISAT/MERIS multispectral images. *IEEE Transactions on Geoscience and Remote Sensing*, *45*(12), pp.4105-4118.

Hatzianastassiou, N., Matsoukas, C., Fotiadi, A., Pavlakis, K.G., Drakakis, E., Hatzidimitriou, D. and Vardavas, I., 2005. Global distribution of Earth's surface

shortwave radiation budget. *Atmospheric Chemistry and Physics*, *5*(10), pp.2847-2867.

Howard, L., 1804. On the Modification of Clouds and the Principles of their Production, Suspension and Destruction: Being the Substance of an Essay Read Before the Askesian Society in Session 1802–1803. *J. Taylor: London*.

Hobbs, P.V. and Mason, B.J., 1964. The sintering and adhesion of ice. *Philosophical Magazine*, *9*(98), pp.181-197.

Heymsfield, A.J. and Platt, C.M.R., 1984. A parameterization of the particle size spectrum of ice clouds in terms of the ambient temperature and the ice water content. *Journal of the atmospheric sciences*, *41*(5), pp.846-855.

Henderson, D. S., L'Ecuyer, T., Stephens, G., Partain, P., & Sekiguchi, M., 2013. A multisensor perspective on the radiative impacts of clouds and aerosols. *Journal of Applied Meteorology and Climatology*, 52(4), 853-871.

Hendrick, F., Van Roozendael, M., Kylling, A., Petritoli, A., Rozanov, A., Sanghavi, S., Schofield, R., Von, C., Wagner, T., Wittrock, F. and Fonteyn, D., 2005. SRef-ID: 1680-7324/acp/2006-6-93 European Geosciences Union Atmospheric Chemistry and Physics.

Hausmann, P., Zinner, T., Emde, C. and Mayer, B., 2012. Ground-based remote sensing of optically thin ice clouds. *Master's thesis, Meteorological Institute Munich, LMU*.

Inamdar, A.K. and Guillevic, P.C., 2015. Net Surface Shortwave Radiation from GOES Imagery Product Evaluation Using Ground-Based Measurements from SURFRAD. *Remote Sensing*, *7*(8), pp.10788-10814.

Illman, P.E., 1995. *The pilot's handbook of aeronautical knowledge*. Tab Books.

Islam, M. D., Kubo, I., Ohadi, M., & Alili, A. A., 2009. Measurement of solar energy radiation in Abu Dhabi, UAE. *Applied Energy*, 86(4), 511-515.

IPCC., 2007a. *Intergovernmental panel on climate change*. Geneva: IPCC Secretariat.

Jedlovec, G., 2009. Automated Detection of Clouds in Satellite Imagery, Advances in Geoscience and Remote Sensing, Gary Jedlovec (Ed.), InTech, DOI: 10.5772/8326.

Jagpal, R.K., Quine, B.M., Chesser, H., Abrarov, S.M. and Lee, R., 2010. Calibration and in-orbit performance of the Argus 1000 spectrometer-the Canadian pollution monitor. *Journal of Applied Remote Sensing*, *4*(1), pp.049501-049501.

Jagpal, R.K., 2011. Calibration and Validation of Argus 1000 Spectrometer–A Canadian Pollution Monitor (Doctoral dissertation, York University, Toronto).

Jagpal, R.K., Siddiqui, R., Brendan M. Quine, Sanjar M. Abrarov., 2014. Carbon dioxide retrieval of Argus 1000 space data by using GENSPECT line-by-line radiative transfer model**,** *IAF, Toronto,Canada, International level conference proceedings* : Poster session, http://www.iafastro.net/iac/paper/id/26425/summary/.

Jiang, J. H., Su, H., Zhai, C., Perun, V. S., Del Genio, A., Nazarenko, L. S., & Gettelman, A., 2012. Evaluation of cloud and water vapor simulations in CMIP5 climate models using NASA "A-Train" satellite observations. *Journal of Geophysical Research: Atmospheres*, 117(D14).

Jacob, D., 1999. *Introduction to atmospheric chemistry*. Princeton University Press.

Jounot, L. J., and Drummond, J. R.: Measurements of pollution in the troposphere-aircraft (MOPITT-A), *Geosci. Remote Sens. Symp.*, 2002. IGARSS '02. 2002 IEEE International, 6, 3180 - 3182, 2002.

Justice, C.O., Vermote, E., Townshend, J.R., Defries, R., Roy, D.P., Hall, D.K., Salomonson, V.V., Privette, J.L., Riggs, G., Strahler, A. and Lucht, W., 1998. The Moderate Resolution Imaging Spectroradiometer (MODIS): Land remote sensing for global change research. *IEEE Transactions on Geoscience and Remote Sensing*, *36*(4), pp.1228-1249.

Jedlovec, G., 2010. Automated detection of clouds in satellite imagery.

Jensen, E. and Pfister, L., 2004. Transport and freeze-drying in the tropical tropopause layer. *Journal of Geophysical Research: Atmospheres*, *109*(D2).

Jensen, E.J., Kinne, S. and Toon, O.B., 1994. Tropical cirrus cloud radiative forcing: Sensitivity studies. *Geophysical research letters*, *21*(18), pp.2023-2026.

Kiehl, J.T. and Briegleb, B.P., 1992. Comparison of the observed and calculated clear sky greenhouse effect: Implications for climate studies. *Journal of Geophysical Research: Atmospheres*, *97*(D9), pp.10037-10049.

Kyrölä, E., Tamminen, J., Leppelmeier, G. W., Sofieva, V., Hassinen, S., Bertaux, J. L., ... & Vanhellemont, F., 2004. GOMOS on Envisat: An overview. Advances in Space Research, 33(7), 1020-1028.

Koukouli, M., Balis, D., Loyola, D., Valks, P., Zimmer, W., Hao, N., Lambert, J.C., Van Roozendael, M., Lerot, C. and Spurr, R., 2012. Geophysical validation and long-term consistency between GOME-2/MetOp-A total ozone column and measurements from the sensors GOME/ERS-2, SCIAMACHY/ENVISAT and OMI/Aura. *Atmospheric Measurement Techniques*, *5*(5), pp.2169-2181.

Kristiansen, J., and Kristjansson, J.E., 1999. Shortwave cloud forcing of marine stratocumulus clouds. *Physics and Chemistry of the Earth, Part B: Hydrology, Oceans and Atmosphere*, *24*(3), pp.225-230.

Kahn, B.H., Eldering, A., Irion, F.W., Mills, F.P., Sen, B. and Gunson, M.R., 2002. Cloud identification in Atmospheric Trace Molecule Spectroscopy infrared occultation measurements. *Applied optics*, *41*(15), pp.2768-2780.

Kokhanovsky, A.A., Platnick, S. and King, M.D., 2011. Remote sensing of terrestrial clouds from space using backscattering and thermal emission techniques. In *The Remote Sensing of Tropospheric Composition from Space* (pp. 231-257). Springer Berlin Heidelberg.

Krezel, A. and Paszkuta, M., 2011. Automatic detection of cloud cover over the Baltic Sea. *Journal of Atmospheric and Oceanic Technology*, *28*(9), pp.1117-1128.

Korolev, A.V., Isaac, G.A., Cober, S.G., Strapp, J.W. and Hallett, J., 2003. Microphysical characterization of mixed-phase clouds. *Quarterly Journal of the Royal Meteorological Society*, *129*(587), pp.39-65.

Kjerstad, N., 2011. *Ice navigation*. Tapir Acad. Press.

Lohmann, U., Spichtinger, P., Jess, S., Peter, T. and Smit, H., 2008. Cirrus cloud formation and ice supersaturated regions in a global climate model. *Environmental research letters*, *3*(4), p.045022.

Loeb, N. G., and Kato S., 2002. Top-of-atmosphere direct radiative effect of aerosols from the Clouds and the Earth's Radiant Energy System Satellite instrument (CERES), *J. Clim.*, *15*, 1474 – 1484.

Li, W. and Li, D., 2008, October. Cloud detection in MODIS data based on spectrum analysis and snake model. In *Geoinformatics 2008 and Joint Conference on GIS and Built Environment: Classification of Remote Sensing Images* (pp. 714710-714710). International Society for Optics and Photonics.

Lin, B., Minnis, P., Fan, T.F., Hu, Y. and Sun, W., 2010. Radiation characteristics of low and high clouds in different oceanic regions observed by CERES and MODIS. *International Journal of Remote Sensing*, *31*(24), pp.6473-6492.

Levelt, P.F., van den Oord, G.H., Dobber, M.R., Malkki, A., Visser, H., de Vries, J., Stammes, P., Lundell, J.O. and Saari, H., 2006. The ozone monitoring instrument. *IEEE Transactions on geoscience and remote sensing*, *44*(5), pp.1093-1101.

Lorsignol, J., Hollier, P.A. and Deshayes, J.P., 1991, August. Polarization and directionality of the Earth's reflectances: the POLDER instrument. In *Orlando'91, Orlando, FL* (pp. 155-163). International Society for Optics and Photonics.

Mao, J. and Kawa, S.R., 2004, February. Measurement of atmospheric carbon dioxide column from space using reflected Sunlight. In *Remote Sensing* (pp. 336-346). International Society for Optics and Photonics.

McIntire, T.J. and Simpson, J.J., 2002. Arctic sea ice, cloud, water, and lead classification using neural networks and 1.6-/spl mu/m data. *IEEE Transactions on Geoscience and Remote Sensing*, *40*(9), pp.1956-1972.

Mateos, D., Antón, M., Valenzuela, A., Cazorla, A., Olmo, F.J. and Alados-Arboledas, L., 2014. Efficiency of clouds on shortwave radiation using experimental data. *Applied Energy*, *113*, pp.1216-1219.

McNally, A.P. and Watts, P.D., 2003. A cloud detection algorithm for high-spectral-resolution infrared sounders. *Quarterly Journal of the Royal Meteorological Society*, *129*(595), pp.3411-3423.

McCoy, D. T., Hartmann, D. L., & Grosvenor, D. P., 2014. Observed Southern Ocean Cloud Properties and Shortwave Reflection. Part II: Phase Changes and Low Cloud Feedback. *Journal of Climate*, 27(23), 8858-8868.

Murray, B.J., O'sullivan, D., Atkinson, J.D. and Webb, M.E., 2012. Ice nucleation by particles immersed in supercooled cloud droplets. *Chemical Society Reviews*, *41*(19), pp.6519-6554.

Mitchell, J., 2003. Nimbostratus clouds mean dreary days. *ChemMatters*, p.13.

Mishchenko, M.I., Travis, L.D. and Lacis, A.A., 2002. *Scattering, absorption, and emission of light by small particles*. Cambridge university press.

McKernan, E., Quine, B. M., and Drummond, J. R., MOPITT sensitivity studies, 2002. Computation of instrument parameter dependencies, 2002 IEEE *International Geoscience and Remote Sensing Symposium* (IGARSS) 2, 1102 – 1104.

Mills, G., 2008. Luke Howard and the climate of London. *Weather*, *63*(6), pp.153-157.

Minnis, P., Sun-Mack, S., Chen, Y., Yi, H., Huang, J., Nguyen, L. and Khaiyer, M.M., 2005, October. Detection and retrieval of multi-layered cloud properties using satellite data. In *Remote Sensing* (pp. 597909-597909). International Society for Optics and Photonics.

Mishchenko, M.I., Travis, L.D. and Lacis, A.A., 2002. *Scattering, absorption, and emission of light by small particles*. Cambridge university press.

Mishchenko, M.I., Rossow, W.B., Macke, A. and Lacis, A.A., 1996. Sensitivity of cirrus cloud albedo, bidirectional reflectance and optical thickness retrieval accuracy to ice particle shape. *Journal of Geophysical Research: Atmospheres*, *101*(D12), pp.16973-16985.

McFarquhar G. M. and Heymsfield A. J., 1998 The definition and significance of an effective radius for ice clouds. *J. Atmos. Sci.*, 55:2039–2052.

Mitchell, D. L. and Finnegan, W., 2009. Modification of cirrus clouds to reduce global warming. *Environmental Research Letters*, *4*(4), p.045102.

NOAA (National Centers for Environmental Information) - Greenhouse gases, water vapor (https://www.ncdc.noaa.gov/monitoring-references/faq/greenhouse-gases.php?section=watervapor).

Nett, H., Frerick, J., Paulsen, T., & Levrini, G., 2001. The atmospheric instruments and their applications: GOMOS, MIPAS and SCIAMACHY. ESA bulletin, 106, 77-87.

Nankervis, C.J., 2013. Co-located analysis of ice clouds detected from space and their impact on longwave energy transfer.

NASA *(*National Aeronautics and Space Administration*)* - Earth Data (https://Earthdata.nasa.gov/user-resources/remote-sensors).

O'Shea, S.J., Choularton, T.W., Lloyd, G., Crosier, J., Bower, K.N., Gallagher, M., Abel, S.J., Cotton, R.J., Brown, P.R.A., Fugal, J.P. and Schlenczek, O., 2016. Airborne observations of the microphysical structure of two contrasting cirrus clouds. *Journal of Geophysical Research: Atmospheres*, *121*(22).

Pepin, N. and Losleben, M., 2002. Climate change in the Colorado Rocky Mountains: free air versus surface temperature trends. *International journal of climatology*, *22*(3), pp.311-329.

Pacek, J.T., 1981. *Terminal Forecast Reference Notebook, Detachment 12, 15th Weather Squadron for Selfridge Air National Guard Base, Michigan* (No. 7WW-TFRN-81-001). WEATHER WING (7TH) SCOTT AFB IL.

Parkinson, C. L., Ward, A., King M. D., eds., 2006. Orbiting Carbon Observatory (PDF). Earth Science Reference Handbook. NASA. pp. 199–203. Retrieved 14 May 2015.

Price, J.C., 1984. Land surface temperature measurements from the split window channels of the NOAA 7 Advanced Very High Resolution Radiometer. *Journal of Geophysical Research: Atmospheres*, *89*(D5), pp.7231-7237.

Quine, B.M. and Drummond, J.R., 2002. GENSPECT: a line-by-line code with selectable interpolation error tolerance. *Journal of Quantitative Spectroscopy and Radiative Transfer*, *74*(2), pp.147-165.

Quine, B. M. and Abrarov, S. M., 2013, Application of the spectrally integrated Voigt function to line-by-line radiative transfer modelling, *Journal of Quantitative Spectroscopy and Radiative Transfer*, 127, pp. 37-48.

Rossow, W.B., 2011. International satellite cloud climatology project.

Rossow, W.B. and Garder, L.C., 1993. Cloud detection using satellite measurements of infrared and visible radiances for ISCCP. *Journal of climate*, *6*(12), pp.2341-2369.

Rankin, D., Kekez, D. D., Zee, R. E., Pranajaya, F. M., Foisy, D. G., & Beattie, A. M., 2005. The CanX-2 nanosatellite: expanding the science abilities of nanosatellites. Acta Astronautica, 57(2), 167-174.

Rayner, P., Jacob, D. J., Suntharalingam, P., Jones, D. B. A., Denning, A. S., Nicholls, M. E., Doney, S. C., Pawson, S., Boesch, H., Connor, B. J., Fung, I. Y., O'Brien, D., Salawitch, R. J., Reuter, M., Buchwitz, M., Schneising, O., Heymann, J., Bovensmann, H. and Burrows, J.P., 2009. A method for improved SCIAMACHY CO_2 retrieval in the presence of optically thin clouds. Atmospheric Measurement Techniques Discussions, 2, 2483-2538.

Russell, L.M., 2015. Atmospheric science: Sea-spray particles cause freezing in clouds. *Nature*, *525*(7568), pp.194-195.

Yau, M.K. and Rogers, R.R., 1976. *A short course in cloud physics*. Elsevier.

Ramanathan, V., 1987. The role of Earth radiation budget studies in climate and general circulation research. *Journal of Geophysical Research: Atmospheres*, *92*(D4), pp.4075-4095.

Schiffer, R.A. and Rossow, W.B., 1983. The International Satellite Cloud Climatology Project (ISCCP)- The first project of the World Climate Research Programme. *American Meteorological Society, Bulletin*, *64*, pp.779-784.

Stephens, G.L. and Kummerow, C.D., 2007. The remote sensing of clouds and precipitation from space: A review. *Journal of the Atmospheric Sciences*, *64*(11), pp.3742-3765.

Salter, S., Sortino, G. and Latham, J., 2008. Sea-going hardware for the cloud albedo method of reversing global warming. *Philosophical Transactions of the Royal Society of London A: Mathematical, Physical and Engineering Sciences*, *366*(1882), pp.3989-4006.

SRMSat Satellite mission: https://directory.eoportal.org/web/eoportal/satellite-missions/s/srmsat.

SB Sat mission: http://space.skyrocket.de/doc_sdat/sathyabamasat.htm.

Sarda, K., Eagleson, S., Caillibot, E., Grant, C., Kekez, D., Pranajaya, F., & Zee, R. E., 2006. Canadian advanced nanospace experiment 2: Scientific and technological innovation on a three-kilogram satellite. Acta Astronautica, 59(1), 236-245.

Simpson, J. J., 1999. Improved cloud detection and cross-calibration of ATSR, MODIS and MERIS data," in Proceedings of the ATSR International Workshop on the Applications of the ERS along Track Scanning Radiometer, ESA-SP-479, Ed.

Stevens, B., 2011. Twelve Lectures on Cloud Physics. *Max Planck Institute for Meteorology-University of Hamburg*.

Sussmann, R., and M. Buchwitz M., 2005. Initial validation of ENVISAT/SCIAMACHY column, CO by FTIR profile retrievals at the Ground-Truthing Station Zugspitze, *Atmos.Chem. Phys.*, *5*, 14971503.

Shonija, N.K., Popovicheva, O.B., Persiantseva, N.M., Savel'Ev, A.M. and Starik, A.M., 2007. Hydration of aircraft engine soot particles under plume conditions: Effect of sulfuric and nitric acid processing. *Journal of Geophysical Research: Atmospheres*, *112*(D2).

Stephens, G. L., Li, J., Wild, M., Clayson, C. A., Loeb, N., Kato, S., & Andrews, T., 2012. An update on Earth's energy balance in light of the latest global observations. *Nature Geoscience*, 5(10), 691-696.

Stephens, G.L., Vane, D.G., Boain, R.J., Mace, G.G., Sassen, K., Wang, Z., Illingworth, A.J., O'Connor, E.J., Rossow, W.B., Durden, S.L. and Miller, S.D., 2002. The

CloudSat mission and the A-Train: A new dimension of space-based observations of clouds and precipitation. *Bulletin of the American Meteorological Society*, *83*(12), pp.1771-1790.

Solomon, S. ed., 2007. *Climate change 2007-the physical science basis: Working group I contribution to the fourth assessment report of the IPCC* (Vol. 4). Cambridge University Press.

Siddiqui, R., Jagpal, R.K., Salem, N.A. and Quine, B.M., 2015. Classification of cloud scenes by Argus spectral data. *International Journal of Space Science and Engineering*, *3*(4), pp.295-311.

Siddiqui, R., Jagpal, R.K., Salem, N.A. and Quine, B.M., 2016. Short Wave upwelling Radiative Flux (SWupRF) within NIR range for the selected greenhouse wavelength bands of O_2, H_2O, CO_2 and CH_4 by Argus 1000 along with GENSPECT line by line radiative transfer model. *arXiv preprint arXiv:1608.05386*.

Siddiqui, R., Brendan M. Quine., 2016. Continuous and stochastic methods for modeling rain drop growth in clouds. *International Journal of Water Resources and Environmental Engineering*, 8(3), pp.32-38.

Siddiqui, R., Jagpal, R.K., and Quine., B. M. 2017. Short Wave upwelling Radiative Flux (SWupRF) within NIR range for the selected greenhouse wavelength bands of O_2, H_2O, CO_2 and CH_4 by Argus 1000 along with GENSPECT line by line radiative transfer model. *Canadian journal of Remote Sensing*, CJRS-16-0081, (In press).

Siddiqui, R., Brendan M. Quine., 2016. Efficient detection of cloud scenes by Radiance Enhancement and Shortwave upwelling Radiative Flux within the NIR wavelength

bands of space orbiting Argus 1000 spectrometer. *Remote Sensing of Environment*, RSE-D-16-01373 (submitted).

Siddiqui, R., Naif Al Salem, Rajinder K Jagpal, Brendan M Quine., 2016. The efficient detection of cloud scenes by Radiance Enhancement (RE) and with their impact on Earth global energy budget due to Short Wave upwelling Radiative Flux (SWupRF) within NIR spectral range of space-orbiting Argus1000 micro-spectrometer, *ExoClimes - The Diversity of Planetary Atmospheres, Squamish, B.C, Canada, NASA Astrobiology Institute* : Poster session, https://nai.nasa.gov/seminars/featured-seminar-channels/conferences-and workshops/2016/8/1/exoclimes-2016/.

Siddiqui, R., Brendan M Quine, Rajinder K Jagpal, Naif Al Salem, Sanjar Abrarov., 2015. The climate impact of short wave upwelling radiative flux on the global energy budget using GENSPECT synthetic model along with Argus 1000 spectrometer, *AGU Fall Meeting, Montreal, Quebec, Canada, International level conference proceedings*: Poster session, https://agu.confex.com/agu/fm15/preliminaryview.cgi/Paper33616.html.

Siddiqui, R., Brendan M. Quine, Caroline Roberts, Naif Al Salem, Catherine Tsouvaltsidis, Rajinder Jagpal., 2014. Efficient Detection of Cloud Scenes from Spectral Data of Space-Orbiting Argus1000 Micro-Spectrometer, *HPCS-2014, Halifax, Canada, national level conference proceedings*: Poster session, http://2014.hpcs.ca/program/#posters.

Someya, Y., Imasu, R., Saitoh, N., Ota, Y. and Shiomi, K., 2016. A development of cloud top height retrieval using thermal infrared spectra observed with GOSAT and

comparison with CALIPSO data. *Atmospheric Measurement Techniques*, *9*(5), pp.1981-1992.

Satheesh, S. K., and V. Ramanathan., 2000. Large differences in tropical aerosol forcing at the top of the atmosphere and Earth's surface, *Nature, 405*, 60 – 63.

Schuessler, O., Rodriguez, D.G.L., Doicu, A. and Spurr, R., 2014. Information Content in the Oxygen $ A $-Band for the Retrieval of Macrophysical Cloud Parameters. *IEEE Transactions on Geoscience and Remote Sensing*, *52*(6), pp.3246-3255.

Song, X., Liu, Z. and Zhao, Y., 2004, September. Cloud detection and analysis of MODIS image. In *Geoscience and Remote Sensing Symposium, 2004. IGARSS'04. Proceedings. 2004 IEEE International* (Vol. 4, pp. 2764-2767). IEEE.

Tang, B., Li, Z.L. and Zhang, R., 2006. A direct method for estimating net surface shortwave radiation from MODIS data. *Remote Sensing of Environment*, *103*(1), pp.115-126.

Tang, H., Yu, K., Hagolle, O., Jiang, K., Geng, X. and Zhao, Y., 2013. A cloud detection method based on a time series of MODIS surface reflectance images. *International Journal of Digital Earth*, *6*(sup1), pp.157-171.

Toohey, M., Quine, B.M., Strong, K., Bernath, P.F., Boone, C.D., Jonsson, A.I., McElroy, C.T., Walker, K.A. and Wunch, D., 2007. Balloon-borne radiometer measurement of Northern Hemisphere mid-latitude stratospheric HNO 3 profiles spanning 12 years. *Atmospheric Chemistry and Physics Discussions*, *7*(4), pp.11561-11586.

Toohey, M., 2009. *Comparing remote sounding measurements of a variable stratosphere* (Doctoral dissertation, University of Toronto).

U. Feister and K. Gericke, 1998. Cloud flagging of UV spectral irradiance measurements. *Atmospheric Research*, vol. 49, no. 2, pp. 115–138, View at Publisher

van Diedenhoven, B., 2007. *Satellite Remote Sensing of Cloud Properties in Support of Trace Gas Retrievals* (Doctoral dissertation, Ph. D. thesis, Free University, Amsterdam).

Vernier, J.P., Pommereau, J.P., Garnier, A., Pelon, J., Larsen, N., Nielsen, J., Christensen, T., Cairo, F., Thomason, L.W., Leblanc, T. and McDermid, I.S., 2009. Tropical stratospheric aerosol layer from CALIPSO lidar observations. *Journal of Geophysical Research: Atmospheres*, *114*(D4).

Wang, T., Yan, G., Shi, J., Mu, X., Chen, L., Ren, H., Jiao, Z. and Zhao, J., 2014, July. Topographic correction of retrieved surface shortwave radiative fluxes from space under clear-sky conditions. In 2014 *IEEE Geoscience and Remote Sensing Symposium* (pp. 1813-1816). IEEE.

Wang, X.C., Zhang, C., Ma, X. and Luo, L., 2015. *Water cycle management: a new paradigm of wastewater reuse and safety control*. Heidelberg: Springer.

Wang, J. and Rossow, W.B., 1995. Determination of cloud vertical structure from upper-air observations. *Journal of Applied Meteorology*, *34*(10), pp.2243-2258.

Waters, J.W. and Mergenthaler, J.L., 1999. Upper tropospheric humidity and thin cirrus. *Geophysical research letters*, *27*(17), pp.2645-2648.

Waliser D. E., Li J.-L. F., Woods C. P., Austin R. T., Bacmeister J., Chern J., A. D. Genio, J. H. Jiang, Z. Kuang, H. Meng, P. Minnis, S. Platnick, W. B. Rossow, G. L. Stephens, S. Sun-Mack, W.-K. Tao, A. M. Tompkins, D. G. Vane, C. Walker, and

D. Wu., 2009. Cloud ice: A climate model challenge with signs and expectations of progress. *J. Geophys. Res.*, 114:D00A21. doi: 10.1029/2008JD010015.

Winker, D.M., Vaughan, M.A., Omar, A., Hu, Y., Powell, K.A., Liu, Z., Hunt, W.H. and Young, S.A., 2009. Overview of the CALIPSO mission and CALIOP data processing algorithms. *Journal of Atmospheric and Oceanic Technology*, *26*(11), pp.2310-2323.

Winker, D.M., Pelon, J.R. and McCormick, M.P., 2003,. The CALIPSO mission: Spaceborne lidar for observation of aerosols and clouds. In Third International Asia-Pacific Environmental Remote Sensing *Remote Sensing of the Atmosphere, Ocean, Environment, and Space* (pp. 1-11). International Society for Optics and Photonics.

Williams, J., 2009. Thunderstorms and Tornadoes. In *The AMS Weather Book: The Ultimate Guide to America's Weather* (pp. 176-203). American Meteorological Society.

Wilson, T.W., Ladino, L.A., Alpert, P.A., Breckels, M.N., Brooks, I.M., Browse, J., Burrows, S.M., Carslaw, K.S., Huffman, J.A., Judd, C. and Kilthau, W.P., 2015. A marine biogenic source of atmospheric ice-nucleating particles. *Nature*, *525*(7568), pp.234-238.

Wielicki, B.A., Wong, T., Allan, R.P., Slingo, A., Kiehl, J.T., Soden, B.J., Gordon, C.T., Miller, A.J., Yang, S.K., Randall, D.A. and Robertson, F., 2002. Evidence for large decadal variability in the tropical mean radiative energy budget. *Science*, *295*(5556), pp.841-844.

Wielicki, B. A., Barkstrom, B. R., Baum, B. A., Charlock, T. P., Green, R. N., Kratz, D. P., ... & Young, D. F., 1998. Clouds and the Earth's Radiant Energy System (CERES): algorithm overview. *IEEE Transactions on Geoscience and Remote Sensing*, 36(4), 1127-1141.

Walshaw, C.D., and Rodgers, C.D., 1963. The effect of the Curtis-Godson approximation on the accuracy of radiative heating-rate calculations. *Quarterly Journal of the Royal Meteorological Society, 89*(379), pp.122-130.

Wagner, T., Beirle, S., Deutschmann, T. and de Vries, M.P., 2010. A sensitivity analysis of Ring effect to aerosol properties and comparison to satellite observations. *Atmospheric Measurement Techniques*, *3*(6), p.1723.

Yang, P., Wei, H., Huang, H.L., Baum, B.A., Hu, Y.X., Kattawar, G.W., Mishchenko, M.I. and Fu, Q., 2005. Scattering and absorption property database for nonspherical ice particles in the near-through far-infrared spectral region. *Applied optics*, *44*(26), pp.5512-5523.

Zeng, S., Cornet, C., Parol, F., Riedi, J. and Thieuleux, F., 2012. A better understanding of cloud optical thickness derived from the passive sensors MODIS/AQUA and POLDER/PARASOL in the A-Train constellation. *Atmospheric Chemistry and Physics, 12*(23), pp.11245-11259.

Zelinka, M.D. and Hartmann, D.L., 2010. Why is longwave cloud feedback positive?. *Journal of Geophysical Research: Atmospheres*, *115*(D16).

Zhang, Z., S. Platnick, P. Yang, A. K. Heidinger, and J. M. Comstock., 2010. Effects of ice particle size vertical inhomogeneity on the passive remote sensing of ice clouds. *J. Geophys. Res.*, 115: D17203, doi: 10.1029/2010JD013835.

Zhang, Z., Yang, P., Kattawar, G., Huang, H.L.A., Greenwald, T., Li, J., Baum, B.A., Zhou, D.K. and Hu, Y., 2007. A fast infrared radiative transfer model based on the adding–doubling method for hyperspectral remote-sensing applications. *Journal of Quantitative Spectroscopy and Radiative Transfer*, *105*(2), pp.243-263.